Absolute O_3 and OH densities measurement by two-beam UV-LED absorption spectroscopy in atmospheric pressure plasmas

Apiwat Wijaikhum

PhD

University of York

Physics

September 2016

I would like to dedicate this thesis to my beloved family.

Abstract

Low temperature atmospheric pressure plasmas (APPs) create rich environment of reactive particle species and chemical-physical interactions at close-to-room temperature and ambient pressure which calls for a wide range of fundamental and application studies. APPs for biomedical applications is one of the emerging interdisciplinary researches. Its fundamental mechanisms have been studied using different numerical models and various diagnostic techniques. With hundreds of particle species and complex reactions, each species requires unique measurement techniques. In a typical APP, ozone (O_3), one of the key species in living-cells inactivation, is produced from the complex reaction chain of short-lived oxygen atoms and excited molecules. Measurement and theoretical predictions of O_3 densities can have high uncertainties. The measurements of O_3 densities inside the small plasma volume are challenging due to the sensitivity to non-plasma parameters. In this work, two-beam UV-LED absorption spectroscopy has been developed by using a Mach-Zehnder configuration for O_3 density measurements on the core of a homogeneous, He-O_2 capacitively coupled, 13.56 MHz RF-driven APP. The improved technique allows for high-sensitivity measurement in the order of 10^{-3} absorption signal with 10^{-4} of uncertainty. The anti-correlation between O_3 density and gas temperature was observed and described based on the plasma chemistry models. For controlling-parameter effect, the duty-cycle in frequency modulations showed a significant influence on the spatial profile of O_3 density in the plasma channel. From an application perspective, the developed technique was able to provide 2D O_3 density distribution in the effluent region of a co-axial DBD kHz-driven APPJ when applied to biological samples. The correlation between radial O_3 density profiles and bacterial inactivation areas was investigated. In the relatively realistic condition with higher H_2O vapour admixture, hydroxyl (OH) density, which is one of important radical species, can be measured using the UV absorption technique. Thus, the setup has been adjusted in order to measure both species. Furthermore, O_3 density in the CO_2-CO conversion 40.68 MHz RF-driven APP, an important process in chemical research, was observed. The O_3 density as a function of plasma power and CO_2 concentration provided a significant contribution to the main production and destruction channels of the conversion processes.

Table of Contents

List of Tables

List of Figures

Acknowledgements

This work would not be possible if there was no invaluable support from the others. First of all, I would like to thanks my supervisor Timo Gans for one of biggest opportunities of my study in involving this research group. His years-long support and encourage lead me to this point. I would like to thank Deborah for all advices, opportunities and huge supports since the first day I was in YPI. All experiments could not be achieved without the strong support by Kari and Richard.

Many thanks for warm welcome and earlier settlement from Arthur, Andy Hurlbatt, Andy West, Andrew Gibson and Martin. Thanks for your enjoyment and every moment of your support including experiments, conferences and numerical works. Thanks to a nice collaboration with Daniel and suggestion from Volker, Ruhr-Universität Bochum. I would like thank Sandra and Angela for a very nice collaboration in the experiments and some discussions. Thanks for guideline on the joint plasma-Biology project from Marjan in Department of Biology.

Part of the work could not be done without the helps from James. One of special thanks goes to Prof Jun Yuan for PhD life suggestion during three years. I would like to thank Roddy for a huge support in the laboratory and many parts of data analysis. I also would like to thanks Erik for your valuable advices and help at YPI and conference. Thanks for the warm friendship from Jerome, Yury, Adam, Alex, Sudha, Dave, James Ellis, Frederik, Helen and Layla. Many thanks for nice time with YPI friends, Arka, Mohammed, Peshwaz ,Ozgur, Brendan, Sophia, Ellie, Phil, Jarrod and Rob. Thanks for YPI and Department of Physics staffs who also help so many occasions.

I would like to acknowledge financial support over ten years of my study from the Development and Promotion of Science and Technology Talents Project (DPST), Royal Government of Thailand Scholarship. I also wish to thank my family for their invaluable support and encouragement inspiring me doing this work until the end. Finally, Parinya who always with me along this journey. Thanks for your patience, understanding and love.

Declaration

I declare that this thesis is an original written work of my research, has been composed solely by myself and has not been submitted for any other degree at this, or any other, University. All sources are acknowledged as References. The experimental work is almost entirely my own work; any contributions from colleagues have been indicated clearly and acknowledged. The comparative plasma power density of the used plasma source was investigated by A. West in comparison with the COST reference microplasma jet. Part of plasma chemistry model simulation was performed by S. Schröter. For the biological results, the bacterial inactivations due to the plasma treatment were studied by A. P. Maldonado.

Chapter 1

Introduction

1.1 Motivation

Plasma, a collection of quasi-neutral ionized particles, naturally occurs in the universe due to effects of electromagnetic forces. The most common types are very hot and dense plasma, as found in the cores of stars, and cold plasma as found in interstellar clouds [1]. The physics of plasmas has been studied and developed to provide an understanding of these natural plasmas. What is now required is to find how to generate and control plasma. Artificially produced plasmas on Earth can be similarly classified into hot, dense plasmas and cold, less dense plasmas.

The former type can be described as an *equilibrium plasma* or *fully ionized plasma*. In these plasmas, the ion temperature equals the electron temperature ($T_i \approx T_e$). For example, fusion plasmas have been established and developed for power generation in two types: Magnetic Confinement Fusion (MCF) plasma [2, 3] and Inertial Confinement Fusion (ICF) plasma [4]. The colder plasma is *non-equilibrium plasma*, where $T_g \ll T_e$; it is also called *weakly ionized plasma* or *low temperature plasma*. This type has much wider application, such as industry-scale plasma processing for microelectronics [5, 6], material syntheses [7] and plasma propulsion [8, 9].

Non-equilibrium low-temperature plasma can further be divided into sub-classifications according to operational pressure, which relates to electron density [10]. At low pressure, plasma is generally operated in the glow discharge mode. The large quasi-neutral bulk is separated from the chamber wall by a narrow positive-space-charge region called a 'sheath'. This structure accelerates ions perpendicularly to the surface while confining electrons. The energy of accelerated ions can be controlled for application to any particular surface. This provides various potential applications in plasma-surface processing technol-

ogy, for example micro- and nano-electronics such as plasma etching [11–14] and plasma deposition [15–17].

In low-temperature high-pressure or atmospheric-pressure plasmas (APPs), more collision processes occur and the neutral species dominate charged species [18]. This plasma type has attracted substantial interest in the last few decades due to its nonlinear complexity and potential in a wide range of fundamental research areas and applications, for example plasma medicine [19, 20], material and surface processing technology [21, 22], plasma chemistry [23] and plasma nanoscience [24, 25]. Chemical species generated under this condition are found to be effectively interact and relate to species in living organisms [26]. These show great promise in biomedical applications.

The main important species for biomedical applications have been found to be reactive oxygen and nitrogen species (RONS) [27] such as atomic oxygen (O), ozone (O_3), singlet delta oxygen ($O_2(a^1\Delta_g)$), hydroxyl radical (OH), hydrogen peroxide (H_2O_2), nitric oxide (NO) and nitric acid (HNO_3). The physical and chemical mechanisms and species densities are the most important factors to be qualitatively and quantitatively examined. To understand these fundamental mechanisms, diagnostic techniques [28–30] and principles of plasma spectroscopy [31] have been established. Each individual species density requires specific tools for measurement. Based on the diagnostic and spectroscopy theory, many advanced techniques and technologies have been developed over the last decade to suit each reactive species' properties. For example, atomic oxygen densities have been measured using two-photon absorption laser-induced fluorescence (TALIF) [32, 33], VUV synchrotron absorption spectroscopy [34] and energy resolved actinometry (ERA) [35]. Singlet delta oxygen densities can be measured using infrared optical emission spectroscopy [36, 37]. OH density can be obtained by laser-induced fluorescence (LIF) [38–40] and UV absorption spectroscopy [41, 42]. Additionally, reactive nitrogen species have been investigated, for example N density by the TALIF [43] and $N_2(A\ ^3\Sigma_u^+)$ [44] and NO [45, 46] by the LIF technique.

Experimental measurements can be complemented with numerical simulations to provide a thorough understanding of the mechanisms related to various discharge gas and electromagnetic excitation characteristics [47–49]. The discharge models provide the chemical descriptions of the plasma in relation to species of interest. The full chemical kinetics models can include tens of species with several hundreds of reactions [50].

In systems of complex gas mixtures, there may be long reaction chains connecting many short lived species. O_3, which has a relatively long lifetime, can make significant direct and indirect contributions to the reactions and densities of other species. This results in par-

ticularly high uncertainties in the theoretical prediction of ozone densities [51]. For basic mechanisms of O_3 in medicine, ozone plays important role in an inactivation microorganisms (such as bacteria, viruses and fungi), in stimulation oxygen metabolism and in activation of the immune system [95]. Therefore, development a reproducible and accurate diagnostic for spatially resolved ozone density and its relation with other plasma parameters are highly desirable.

Ozone has a comparatively large photon absorption cross-section around 255 nm (Hartley band) in the ultra-violet (UV) absorption range [52]. UV absorption therefore provides a versatile measurement technique to investigate O_3 densities. Principally, APP sources are generated between electrode gaps on the order of micrometers to millimeters, leading to a small plasma volume [53]. Previous studies showed spatial O_3 density in the effluent of Micro RF discharge jet in He and O_2 admixture [54] and RF driven DBD APPJ in Ar + O_2 [55]. However, these did not present ozone density with relation of other parameters inside the plasma volume. Direct measurements of ozone densities inside the small active plasma volume provide plasma chemical kinetic information, and are one of the most challenging in this research. The O_3 density can be in spatial non-equilibrium and a short single-pass absorption length provides a relatively low absorption signal. Furthermore, with a mm gap, large electrode temperature variation of the studied plasma source can introduce significant fluctuation in the signal. Therefore, we developed UV-LED absorption spectroscopy using a two-beam setup with a reference beam in Mach-Zehnder configuration for improving signal-to-noise ratios. This allows high-sensitivity measurements in the investigated single-pass small-absorbance regime with the capability of space-resolved measurements. In addition, the developed technique is able to be modified and equipped with additional devices to investigate ozone density in many scenarios.

Atmospheric pressure plasma jet (APPJ) is known as an efficient source for the generation and controlled delivery of reactive species [18, 56]. Most of the main mechanisms in complex plasma models are strongly dependent on electron energy distribution function and gas temperature [51, 57–59]. Ozone density as function of plasma parameters – pulse-modulated driven frequency and gas temperature – were therefore investigated.

From the perspective of biomedical application, the emerging role of RONS in redox biology is of great interest in plasma production [60]. The important role of each main reactive species among the other RONS needed to be identified. Hence, the ozone density profile in the effluent region of a co-axial dielectric barrier discharged (DBD) kHz-driven APPJ when applied to the sample surface was investigated for correlation with the biological results. This makes an important contribution to the understanding of the role of ozone

density in this field. Furthermore, in a plasma with a water-vapour admixture, OH density significantly contributes to hydrogen-oxygen reactive species formation, as observed using UV-LED absorption spectroscopy.

Apart from biomedical application, the conversion of CO_2 into value-added chemicals and liquid fuels is a recent attractive topic [61]. There are various methods in CO_2 conversion but plasma processes are predicted to be the most efficient techniques [62]. For example, dissociation of CO_2 using RF discharge [63] 90% efficiently yielded CO which is one of the main chemical feedstock for further synthesis of fuels and chemicals [64]. In the chemical kinetics models of the process, ozone has an influence on the density of a number of oxygen species, which provide a significant contribution to the conversion processes. Since energy efficiency is one of important factors for conversion product, ozone density is measured as functions of coupled plasma power and CO_2 concentration. The results provide information to support further numerical simulation. The following section lays out all topics in detail in order to reveal the scope of the research.

1.2 Thesis outline

In Chapter 2, the fundamental equations of plasma physics are presented based on a general concept of plasma chemistry simulation models. The background of APPs is presented, in relation to the regime studied. An overview of atmospheric pressure plasma sources with different operating conditions is also discussed. Additionally, the principles of plasma spectroscopy and plasma diagnostics, as related to all experiments in this work, are introduced and the specific details described.

Chapter 3 describes all the details of a two-beam UV-LED absorption setup introduced for the improvement of the signal-to-noise ratio, as compared to the standard one-beam measurement. The effects of non-plasma parameters can be detected and suppressed by this setup. The basic experimental procedure that will later be used and adjusted is described for different conditions in several experimental situations. In addition, the requirements of optimized data acquisition are discussed, for example in relation to time-scales and synchronization of triggering signals.

In Chapter 4, ozone densities are investigated along with the parameters of plasma power and gas temperature. The gas temperatures are measured using N_2 spectroscopy based on an adjusted setup. The results for their physical and chemical mechanisms are discussed in relation to the plasma chemistry model.

Chapter 5 describes the driving frequency as one of the fundamental controlling factors

in the discharge, specifically of electrons. The kHz-frequency and duty cycle modulation signals are synchronized with the UV-LED setup signals for ozone density measurement. The spatially resolved density measurement and the effects of pulsed modulation on the ozone density profile in the plasma channel are also presented. These measurements show the ability to control the delivered ozone species

In Chapter 6, the setup is modified to measure ozone density in the effluent region of a co-axial DBD kHz-driven APPJ when applied downward to a biological sample. The setup, including plasma power supply unit, spatial measurement unit and data acquisition unit, is operated using an in-house computer program. The radial distributions of ozone density at 1 mm above the sample surface can be obtained and the correlation with the bacteria-inactivated area on agar plates observed. Based on this correlation, the role of ozone in bacteria inactivation is discussed.

In Chapter 7, the setup is shown to be able to be modified for measuring hydroxyl (OH) density, which is important in the chemical kinetics of oxygen-hydrogen based reactive species in APPs with H_2O vapour admixtures. Increasing OH density as a function of H_2O vapour admixture agrees with the results gained from a broadband UV absorption experiment. Additionally, the O_3 densities in He with water vapour and O_2 admixtures are investigated and the results discussed according to the chemical model description.

In Chapter 8, O_3 densities which significantly contribute to the main conversion reaction are investigated as a function of the plasma power. The results provide important information to support numerical simulation.

Finally, in Chapter 9, a conclusion on the two-beam UV-LED absorption spectroscopy technique and important results are provided.

Chapter 2

Background

From plasma chemistry model [51], ozone density is produced through the long-chain complex reactions in plasma chemistry model. In order to investigate ozone density in non-thermal atmospheric pressure plasma regime, all necessary background will be briefly provided in this chapter. A kinetic theory is discussed in the first section for their main criteria under atmospheric pressure plasma conditions. Then, elementary collisional mechanisms which are the dominant characteristic of this plasma regime are discussed relating to many important effects.

Then an overview of atmospheric pressure plasma sources for biomedical application will be given. This gives preferable reasons of the used capacitively-coupled RF plasma and coaxial-DBD kHz jet compared to the other types. Principles of the plasmas used will be discussed with further details. In the last section, related fundamentals of diagnostic techniques are provided that help to understand the improvement of the developed Two-beam UV-LED absorption technique.

Defined as a fourth state of matter, plasma is a collection of free charged particles moving in response to electromagnetic fields, which are, on average, electrically neutral. It is characterized by charged particle density, n(particles/m^3), $n \approx n_e \approx n_i$, and temperature, T(K), in equilibrium, T = T_e = T_i, where subscripts e and i represent electron and ion, respectively. Though, plasmas in stars are in thermal equilibrium, laboratory plasmas do not quite reach this equilibrium. The charged particles in laboratory plasmas are electrically driven, which means applied power mainly heats electrons. Meanwhile, the heavy ions efficiently exchange energy through elastic and inelastic collisions with the neutral background gas [65]. Therefore, the non-equilibrium plasma generally has $T_e \gg T_i$.

Plasmas can be classified by charged particle density n and electron temperature T_e. High temperature plasma (HTP), which is equilibrium plasma (e.g. fusion plasma [10]),

typically has $T_e \approx T_i \geq 10^7$ K and $n_e \geq 10^{20}$ m^{-3}. Low-temperature plasmas (LTP) can be divided into two subgroups: thermal LTP (quasi-equilibrium) and non-thermal LTP (non-equilibrium). Thermal plasmas, for example arc plasma and plasma torches, have $T_e \approx T_i \approx T_g \leq 2 \times 10^4$ K. For non-thermal LTP (e.g. glow discharge, corona plasma, APPJ, DBD and plasma needles), the electron temperature is much higher than the ion temperature: $T_i \ll T_e \leq 10^5$ K, $T_i \approx T_g \approx 300$ K.

In this work, the plasmas used are non-thermal atmospheric-pressure LTP, partly ionized and electrically driven. The charged particle collisions with neutral gas molecules are important. The dominant reactions are complex chemical mechanisms which include a large number of elementary processes. Inter-particle collisions occur with different spaces and time-scales, creating a nonlinear and complicated system. To understand the fundamentals of the complex plasma medium, the kinetic theory from the microscopic perspective and the fluid theory from the macroscopic perspective are considered in the first section. Then, the elementary processes in the gas phase are discussed for any possible main reactions involved in the chemical mechanisms of the investigated conditions. After the results description based on the 0D chemical kinetics model, an overview of models used in non-equilibrium LTP is also introduced.

More specific details on the plasma used, along with related diagnostic techniques, are discussed in the later parts of the chapter. One of the main applications of low-temperature APP is in biomedicine. Various plasma sources have been developed in order to suit the requirements of this application. In the later part of the chapter, the physics of typically used plasmas – radio-frequency (RF) capacitively coupled APPJ and co-axial kHz-frequency DBD APPJ – are discussed. For the investigation of the O_3 and OH density, the fundamentals of the UV absorption spectroscopy in relation to the measurement of their densities are introduced in the final part of the chapter, along with some details on the optical devices.

2.1 Kinetic theory and basic equation of nonthermal LTP

The main characteristics of LTP plasmas are as follows: (i) the typical charged particle densities are in the order of 10^{16} - 10^{18} m^{-3}; (ii) the motions of charged particles under electromagnetic force fields are associated with a local space charge and currents due to all the other charged particles; (iii) the short-time-scale variation of the velocities and energies depends on collisions, and it is impossible to trace all individual particle trajectories and interactions [66]. The way to simplify this complex dynamic system is through an analytical combination of kinetic theory and fluid theory.

The kinetic theory of gases, which relies on statistical physics, is usually taken as a starting point to study plasma from the microscopic point of view. The velocity distribution function $f(\mathbf{r}, \mathbf{v}, \mathrm{t})$ is introduced and solved by conservation laws. The transport and reaction coefficients are derived based on this function. These will be involved in calculation of the macroscopic quantities, density n and velocity, $\mathbf{u}$ by integration over the velocity distribution function in the Boltzmann equation. This process finally is expressed in fluid theory concept as discussed in the following sections.

2.1.1 Boltzmann equation and distribution function

For an element plasma volume, particles can be produced by an ionizing collision, destroyed by recombination or enter and leave the element. The equation governing the evolution of the distribution is expressed in the form of a continuity equation, namely the Boltzmann equation:

$$\frac{\partial f}{\partial t} + \mathbf{v}\cdot\nabla_{\mathbf{r}} f + \frac{\mathbf{F}}{m}\cdot\nabla_{\mathbf{v}} f = \left.\frac{\partial f}{\partial t}\right|_c \tag{2.1}$$

where f or $f(\mathbf{r},\mathbf{v},t)$ is a distribution function in the six-dimensional phase space created by particle positions and velocities ($\mathbf{r}$,$\mathbf{v}$) with $\nabla_{\mathbf{r}} = (\hat{x}\partial/\partial x + \hat{y}\partial/\partial y + \hat{z}\partial/\partial z)$ and $\nabla_{\mathbf{v}} = (\hat{x}\partial/\partial v_x + \hat{y}\partial/\partial v_y + \hat{z}\partial/\partial v_z)$. The Lorentz force acting on charged particles is $\mathbf{F} = q[\mathbf{E} + \mathbf{v}\times\mathbf{B}]$, in which the charged particle, q, with mass, m, responds to the local electric and magnetic fields ($\mathbf{E}$ and $\mathbf{B}$), respectively. The collision term is expressed on the right-hand side (RHS). The continuous evolution of the distribution function depends on the applied electromagnetic forces and various kinds of collision. In near-thermal equilibrium, the distribution function of an electron is assumed to have Maxwellian distribution as expressed in equation 2.2. It relates a characteristic electron temperature to the average electron energy and the mean speed of electrons used in the calculation of ionization and excitation coefficients.

$$f_e(v) = n_e \left(\frac{m}{2\pi k \mathrm{T}_e}\right)^{3/2} \exp\left(-\frac{mv^2}{2k\mathrm{T}_e}\right) \tag{2.2}$$

where k is a Boltzmann constant.

However, with sensitive dependence on a Maxwellian distribution of some rate constant and discharge parameters, only the high-energy tail significantly contributes. This yields a smaller rate constant by orders of magnitude than a Maxwellian distribution assumption. When a non-Maxwellian distribution is considered due to the influence of collisions with

excited neutrals [67, 68] as shown in figure 2.1, solving the Boltzmann equation is exceptionally difficult for discharges. Various approximations are used, for example a general simplification of two-term approximation is fundamentally explained in [5] and used in BOLSIG+ program [67].

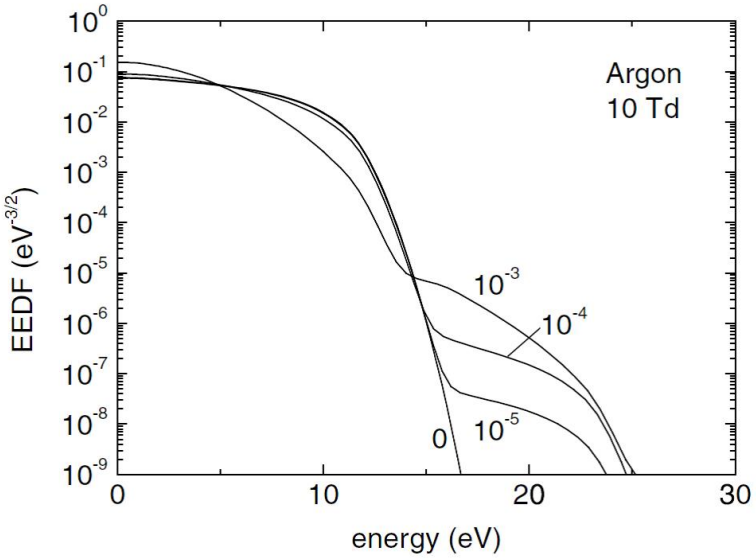

Fig. 2.1 Non-Maxwellian EEDF in argon at 10 Td where the collisions with excited neutrals were taking into account [67].

2.1.2 Governing equation

The charged particles' motion can be alternatively described by the set of fluid (or hydrodynamic or continuity) equations in the macroscopic perspective. The first fluid equation can be obtained by integration of the velocity coordinates into the Boltzmann equation 2.1, which is a particle or species conservation and depends only on the position and time as expressed in equation 2.3.

$$\frac{\partial n}{\partial t} + \nabla \cdot (n\mathbf{u}) = S - L \tag{2.3}$$

The first term on the left-hand side (LHS), which relates to the first term in equation 2.1, describes the changing of density. The second term accounts for the density flows over the local space, corresponding to the second term in the Boltzmann equation. It is a spatial differential operating independently of the velocity integral, where $\mathbf{u}$ or $\mathbf{u}(\mathbf{r},t)$ represents the drift velocity. The force term in equation 2.1 takes into account the distribution func-

tion values at $v = \pm\infty$, which yields zero. On the RHS, the contribution of collision, S, is usually due to elastic and excitation by electron-neutral collisions, $S = \nu_{iz} n_e$, where ν_{iz} is the ionization frequency. The volume loss rate, L, due to the recombination, is usually negligible.

Then, the momentum conservation is obtained by multiplying Boltzmann equation with the momentum of a particle, $m\mathbf{v}$, integrated over the velocity space, which gives

$$nm\left[\frac{\partial \mathbf{u}}{\partial t} + (\mathbf{u}\cdot\nabla)\mathbf{u}\right] = nq\mathbf{E} - \nabla p - m\mathbf{u}\left[n\nu_m + S - L\right] \tag{2.4}$$

where p is the particle pressure and $\mathbf{B} = 0$. The LHS of the equation includes the acceleration and the inertial terms. On the RHS, the electric driving force and the pressure gradient force are in the first and second terms, respectively. The third term, the friction force, expresses how particles are generated and lost when moving at the drift velocity; ν_m is the elastic momentum transfer collision frequency.

The fluid equations can be integrated over the space coordinates and yield a simplified description called the global model. The global particle balance of electrons in plasma, maintained by volume ionization between parallel walls separated by a distance l, is expressed in equation 2.5.

$$\frac{d\bar{n}_e}{dt} = \bar{n}_e n_g K_{iz} - \frac{2\Gamma_{wall}}{l} \tag{2.5}$$

where $\bar{n}_e$ is the average electron density over the separated distance, n_g is the gas density, K_{iz} is a rate coefficient for ionization and Γ_{wall} is electron flux at the wall. Furthermore, the energy balance for electrically driven plasma can be obtained by equation 2.6.

$$\frac{d}{dt}\left(\frac{3}{2}\bar{n}_e k T_e\right) = P_{abs} - P_{loss} \tag{2.6}$$

where P_{abs} is the power absorbed by the electron and P_{loss} is the rate of energy loss in the average lifecycle of electrons and any other loss processes. The absorbed power term depends on the electric field distribution, the current density and the system structure. For the energy loss term, the electron energy can be dissipated by two mechanisms: firstly, the collision with gas such that the energy transfers inelastically into ionization and excitation, and elastically into the thermal energy of gas; secondly, the transfer of kinetic energy to the boundaries.

The details of the fluid equations can be considered from different perspectives in terms of conditions such as pressure, excitation frequency domain and collision frequency. This

leads to different dominant and negligible terms in each plasma type. In the studied non-thermal APP in the RF and kHz frequency domain, it is classified into a high-pressure and low-frequency domain in which the excitation electric-field frequency (ω) is lower than the electron plasma frequency (ω_{pe}). The collision processes play an important role in this plasma regime. The important element collision processes are discussed in the following section.

2.2 Elementary processes in gas phase

In low-temperature non-equilibrium atmospheric pressure plasmas, the collisions of electrons and gas-phase molecules are one of the most important characteristics. The transfer of energy is mostly in elastic processes. The quantum Hamiltonian is always used to describe the elementary processes such as isolated molecules, electron kinetic energy and electron-molecule interactions. A detailed description of the main elementary processes and particles related to this work will be given in the following subsections.

2.2.1 Electron-atom collisions

In an inelastic collision between a much lighter electron and a heavy neutral gas molecule, what should firstly be considered is the energy level of the atom. The energy transition between two different levels, $\Delta\varepsilon$, is defined in equation 2.7, which indicates the threshold energy for the excited state, ε_{ex}. The cross-section for electron-induced excitation equals zero when the energy is below this level.

$$\Delta\varepsilon = \varepsilon_{k+1} - \varepsilon_k = \varepsilon_{ex} \tag{2.7}$$

In this plasma regime, low-temperature atmospheric pressure plasma for biomedical application, He is a preferred background gas as its high thermal conductivity and relatively high electron mobility. Fundamentally, the excited state He significantly contributes as the main pathway of many reactions. In figure 2.2, the bound electrons are allowed for radiative transition at some levels through absorption or emission. The lifetimes of these upper excited states are on the order of 10^{-9} s such as transition from 2^1P and 2^3P to ground state. The excited states can also decay to the levels that do not allow radiative transition to ground state. These are called *metastable states* which has lifetime in range of 10^2 s or longer. For example, the two metastable states of He, 2^1S and 2^3S, have lifetimes of 7.9×10^3 s and 1.95×10^{-2} s, respectively [6].

Stepwise excitation or Penning ionization can occur due to the collisions between the electrons and metastable atoms, which is more efficient than excitation from ground state atoms. However, this depends on the density of the metastable or excited state atoms. Obviously, the metastable state of He (He^*) plays an important role in low-temperature APP, as it acts as an energy reservoir for subsequent Penning ionization of fractional admixture species such as O_2 and N_2 [58]. Moreover, the metastable states of oxygen atoms, $O(^1D)$ and $O(^1S)$, are partly included in the heavy-particle reactions of the reactive oxygen formation [59, 69].

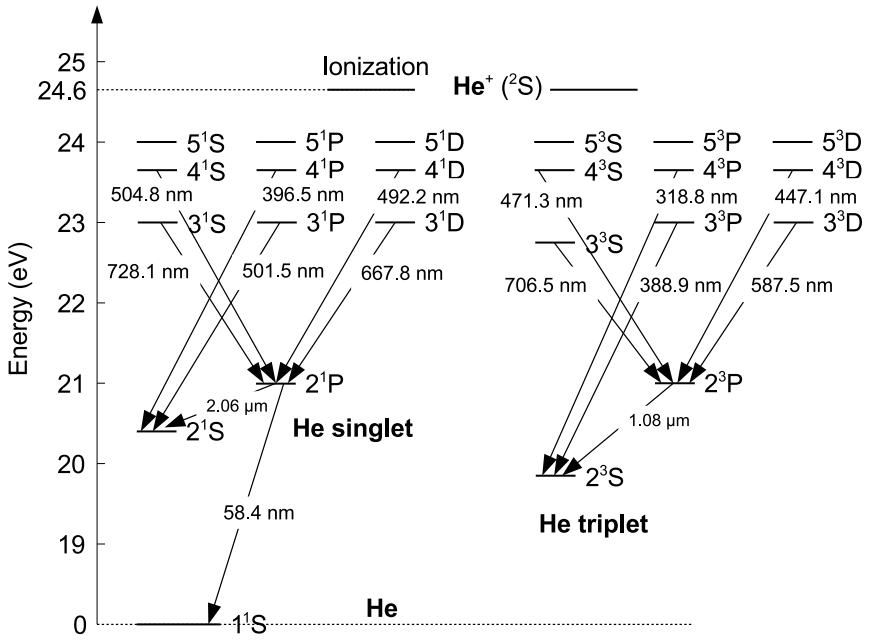

Fig. 2.2 Radiative transition of helium energy levels. Helium is commonly used as a plasma background gas in biological application [6].

2.2.2 Electron-molecule collisions

Due to the internal degrees of freedom of molecules, inelastic energy losses occur at much lower energy than in the case of electron-atom inelastic collision through the excitation to rotational and vibration energy levels. The rotational energy, ε_r, has the general form shown in equation 2.8.

$$\varepsilon_r = \frac{\hbar^2 l(l+1)}{2I} = \left[B_e + \alpha\left(v+\frac{1}{2}\right)\right] l(l+1), \qquad l = 0,1,2,... \tag{2.8}$$

where $B_e = \hbar^2/2I$ is the rotational constant, which is mostly in the range of 10^{-4} - 10^{-3}

eV, $\hbar = 1.05 \times 10^{-34}$ Js, where I is the moment of inertia, l is the quantum number, v is the vibrational quantum number and α is a vibration-rotation interaction constant.

Since the rotational excitations occur at small energies, rotational inelastic losses are of very small significance. In most APP models, the contributions of the rotational excitation are not included. However, these contributions are very useful and are commonly used in gas-temperature determination. The optical emission line profile for the rotational level of excited states of diatomic molecules (rotational temperature), especially nitrogen ($N_2(C)$) and hydroxyl (OH(A)), are used to calculate the gas temperature [70]. Further details will be discussed in the diagnostic technique section 2.5.2.

Vibrational excitation

The vibrational energy level (ε_v) can be established from the eigenvalue equation. The final form is expressed as

$$\varepsilon_v = \left(v + \frac{1}{2}\right)\hbar\nu + V(r_0), \qquad v = 0, 1, 2, ... \tag{2.9}$$

where v is the vibrational quantum number and $V(r_0)$ is the minimum potential. The transition energy is

$$\Delta\varepsilon_v = \varepsilon_v - \varepsilon_{v-1} = \hbar\nu \tag{2.10}$$

In most cases the transition $v = 0 - 1$ is the most important, but this still requires the data from the higher transitional levels derived from theory or beam experiments. The vibrational excitation of molecules can lead to Penning ionization, dissociation and electronic excitation. For example, in He with O_2 admixture, the electron impact with vibration excitation state of $O_2(v)$ mainly transfers into excitation (e + $O_2(v) \rightarrow O_2(^1\Delta)$ + e), dissociation (e + $O_2(v) \rightarrow$ O + O + e) and ionization (e + $O_2(v) \rightarrow O_2^+$ + e + e). About ten of these reactions are included in 184 [58] and 267 [69] reactions of one-dimensional semi-kinetic numerical models of He/O_2 plasma. The rate coefficients of these vibrational excitations depend on the electron energy probability function (EEPF, f(ε)). Furthermore, some interactions with vibrationally excited N_2 can be observed in the chemical kinetic model in atmospheric pressure He/O_2 with humid air impurity (a total of 1048 reactions) [59].

Electronic excitation

The electronic states are defined based on the different electron energies that bound both atoms forming the molecule. The angular momentum of molecular states are denoted by $\Sigma, \Pi, \Delta, ...$ for values of $\Lambda = 0, 1, 2, ...$ The electronic transitions take place over a very short period of time, in the order of 10^{-16} s, such that the intermolecular distance cannot change during this transition. In figure 2.3, the molecule can be excited from grounded state $v = 0$ to excited state $v' = 0 - 5$. For $v' = 0 - 2$, the electron is still bound but can be dissociated at $v' = 3 - 5$. The highest transition probability around r_0 is at $v' = 2$. The potential curve can be higher than the dissociation energy limit (V_D) and excessive energy is converted to the kinetic energy of the molecule, with the maximum energy E_c. These energies typically range between a few eV and 20 eV. For example, the dissociation energies of N_2 and O_2 are 9.76 and 5.11 eV, respectively.

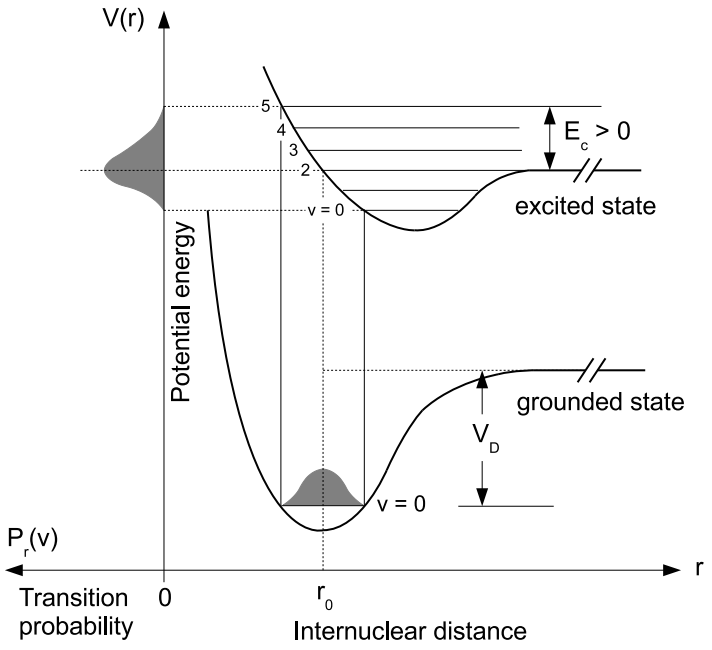

Fig. 2.3 Dissociative electronic excitation of a molecule [6].

Electronic excitation molecules due to electron impact comprise some of the main reactive species, e.g. singlet delta oxygen $O_2(a^1\Delta_g)$ [36] and singlet sigma oxygen $O_2(b^1\Sigma_u^+)$ [51]. They mainly contribute to the formation of the reactive oxygen species that are found in most of the recent studies on this plasma regime. Apart from the excitation level of molecules, the electron impact can induce more reaction reactions such as dissociation, recombination and attachment, which create positive and negative ion species. Table 2.1 [5, 6] shows various

electron-molecule collision processes. These are the primary reactions to create the excited species and ion species and lead further to heavy-particle collisions which are the dominant reactions in the non-thermal atmospheric pressure plasmas.

Table 2.1 Table of electron-molecule collisions where A, B and M are molecules [5, 6].

Process	**Reaction**	**Energy loss**	Δ_ε
Elastic	$e + M \xrightarrow{\varepsilon} e + M$	$\sim 2(m/M)\varepsilon$	~ 0
Electronic excitation	$e + M \xrightarrow{\varepsilon>\varepsilon_{ex}} e + M^j$	ε_{ex}	10 eV
Rotational excitation	$e + M(r) \xrightarrow{\varepsilon>\varepsilon_r} e + M(r')$	ε_r	kT
Vibrational excitation	$e + M(r) \xrightarrow{\varepsilon>\varepsilon_v} e + M(v')$	ε_v	0.1 eV
Electron impact dissociation	$e + AB \xrightarrow{\varepsilon>\varepsilon_d} A + B + e$	ε_d	10 eV
Ionization	$e + AB \xrightarrow{\varepsilon>\varepsilon_i} AB^+ + 2e$	ε_i	15 eV
Dissociative ionization	$e + AB \xrightarrow{\varepsilon>\varepsilon_i} A + B^+ + 2e$	ε_{dis}	15 eV
Dissociative recombination	$e + AB^+ \xrightarrow{\varepsilon>\varepsilon_{d'}} A + B^*$	$\varepsilon_{d'}$	15 eV
Dissociative attachment	$e + AB \xrightarrow{\varepsilon>\varepsilon_a} A + B^-$	ε_a	$\sim$eV
Polar dissociation	$e + AB \xrightarrow{\varepsilon>\varepsilon_{ip}} A^+ + B^- + e$	ε_{ip}	~ 20 eV
Electron impact attachment	$e + AB^- \xrightarrow{\varepsilon>\varepsilon_a} AB + 2e$	ε_a	$\sim$kT
Superelastic collision	$e + M^j \xrightarrow{\varepsilon} e + M$	0.01 $\sim$ -20 eV	

2.2.3 Heavy-particle collisions

Particles in this collision involve ions, neutral, and excited species. Most ions and neutrals range from room temperature ($\sim$ 0.026 eV) in the bulk plasma to about a hundred of eV for ions in RF sheaths [71]. The main categories are listed in table 2.2, while the detailed descriptions can be found in [5, 6]. About tens of these selected species interact with each other in different energy levels and consequently produce several hundreds of reactions.

In atmospheric pressure plasma, the ion-neutral mean free path is smaller than the critical radius which increases the ion-neutral collisions. Therefore, three-body reaction is one of the dominant reactions in this pressure regime [10]. Specifically, the atmospheric pressure plasma for biomedical application focuses on the production and destruction mechanisms of reactive oxygen, nitrogen and hydrogen species [72]. The three-body interactions in the models are reported as the dominant reactions. For example, in a RF driven micro-atmospheric pressure plasma jet [57], interaction of heavy particles, O, O^*, O_2, O_3 and He, are the main processes of O formation.

The formation of the main density of reactive nitrogen species, NO, in He/O_2 with air

Table 2.2 Table of heavy-particle collisions where A, B, X and M are molecules [5, 6].

Process	**Reaction**
Ion-molecule	
Resonant charge transfer	$AB^+ + AB \rightarrow AB + AB^+$
Nonresonant charge transfer	$X^+ + AB \rightarrow AB^+ + X$
Dissociative charge transfer	$X^+ + AB \rightarrow A^+ + B + X$
Ion recombination	$X^- + AB^+ \rightarrow X + AB^*$
Associative detachment	$X^- + AB \rightarrow XAB + e$
Detachment	$X^- + AB \rightarrow X + AB + e$
Three-body ion recombination	$X^+ + AB^- + M \rightarrow XAB + M$
Excited species	
Penning ionization	$X^* + AB \rightarrow X + AB^+ e$
Associative ionization	$X^* + AB \rightarrow XAB^+ + e$
Dissociative ionization	$X^* + AB \rightarrow X + A + B^+ + e$
Excimer formation	$X^* + X + M \rightarrow X_2^* + M$
Transfer of excitation	$X^* + AB \rightarrow X + AB^*$
Ground state molecule	
Transfer of excitation	$X + AB \rightarrow X^+ + AB + e$
	$X + AB \rightarrow X^* + AB$
Three-body association	$X + AB + M \rightarrow XAB + M$

impurity atmospheric pressure plasma [59] reports the interactions between O, NO_2, H, OH, N and NO_3 as the main mechanisms. Furthermore, the study of low-temperature atmospheric pressure He+H_2O plasma for the main species for reactive hydrogen-based species such as OH and H_2O_2 found that the chemical reactions play a key role in production and destruction processes [50]. Since the numerical simulation includes numbers of species, interactions and rate coefficients, there are several models for dealing with this complicated system. Hence, the overview of the simulation models should be given in the following section including details of the 0D semi-kinetic model that is used as a description for all of discussion parts of this work.

2.3 Modeling of non equilibrium low-temperature plasma

In non equilibrium low-temperature plasma, an excitation RF has the period in the order of nanoseconds shorter than the time scale of the complex gas-phase interaction processes. During these processes, the kinetics of active neutral species occur with the gas flowing

through the system in milliseconds or seconds time scales. Due to the vast difference in time scale, the simulations need to treat as many as 10 orders of magnitude in time development [6]. Several techniques of modeling low-temperature plasma have been developed to study the characteristic of an individual plasma condition. The main classification of the modeling can be shown in figure 2.4. The main models are continuum model, particle model, hybrid model and circuit model.

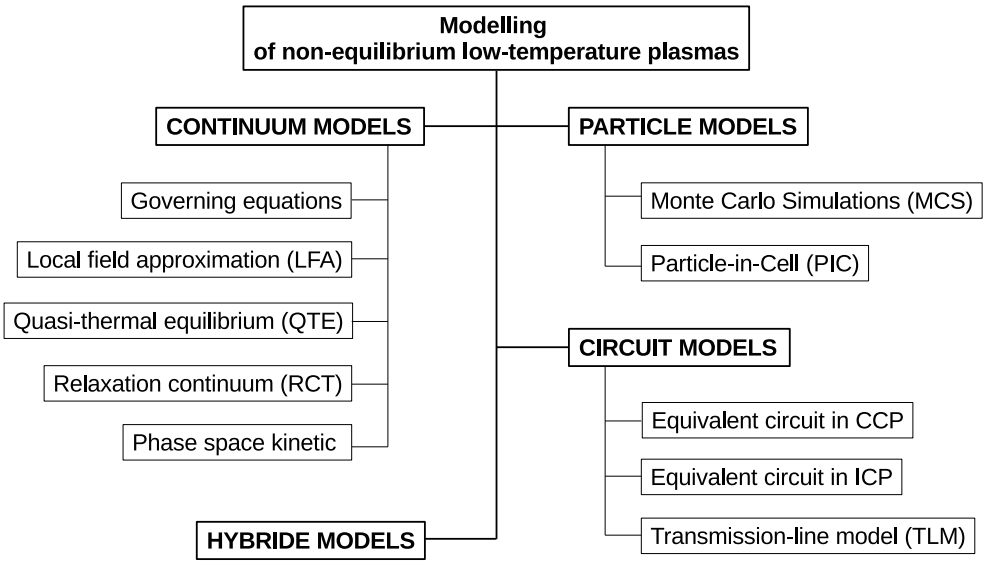

Fig. 2.4 Modelling diagram in non-equilibrium low-temperature plasmas

2.3.1 Continuum models

Continuum model treats particles as fluids and is based on the moments of the Boltzmann equation. These quantities can be obtained by integration of Boltzmann equations over of a different order of velocity space. The corresponding conservation laws are

$$\int (Boltzmann\ Eq.)\ dv \quad \Rightarrow \quad particle\ number\ density \tag{2.11}$$

$$\int (Boltzmann\ Eq.)\ vdv \quad \Rightarrow \quad momentum\ number \tag{2.12}$$

$$\int (Boltzmann\ Eq.)\ v^2 dv \quad \Rightarrow \quad energy\ balance \tag{2.13}$$

The model which treats particles as fluids provides a relatively short computational time compared to the other models. All particles and a set of Maxwell's equation are involved and completed in these continuity or governing equations as described in the kinetic theory section. The set of these governing equations are required to characterize the non-equilibrium plasma in time and configuration space of all particle species. The used simple chemistry model is deduced from 0D semi-kinetic fluid model, which is also based on the continuum concept.

The typical non-equilibrium RF plasma constructs a plasma bulk and ion sheaths in different regimes. Several sub models or equations are required to deal with this complex system. For example, the local field approximation (LFA) assumes a quasi-equilibrium of charged particles at all points in space and for all time. It provides the transport coefficients as a function of reduced field strength (E/N), given by the local electric field (E) and number density of the feed gas (N). The Quasi-Thermal Equilibrium (QTE) model assumes electrons are in thermal equilibrium in plasmas and their energies are Maxwellian distribution. This model suits the high degree of ionization condition. The Relaxation Continuum (RCT) model considers the electrons gaining and losing their momentum and energy in the plasma sheath structure. The effective modified electric field is taken into account in the momentum and energy conservation equation as a relaxation term. Phase Space Kinetic model use two-term approximation in solving the Boltzmann equation for the determination of the transport and rate coefficients of electrons. Details of the other models can be found in [6].

2.4 Atmospheric pressure plasmas

When plasmas operate at atmospheric pressure, the chemical mechanisms are dominated by reactive neutral species, while ion species are insignificant in comparison [18]. In microscopic prospective, the three-body collision and the effect of high-density excited species are taken into account as one of the main elementary processes.

2.4.1 Fundamentals

As plasmas operate at atmospheric pressure, the first characteristic of plasma to be considered is the ignition. The breakdown voltage, V_b, depends on the electrode spacing d and the pressure p as follows

$$V_b = \frac{B(p \cdot d)}{\ln[A(p \cdot d)] - \ln[\ln(1 + 1/\gamma_{se})]} \tag{2.14}$$

where A and B are constants found experimentally, and γ_{se} is the secondary electron emission coefficient of the cathode. The breakdown voltages are optimized through the relation between pressure and electrode space as seen in figure 2.5 [18]. For example, when the plasmas needed to be operated at low voltage, the gap should be narrower. Therefore, electrode spacing in atmospheric pressure plasma is relatively narrow.

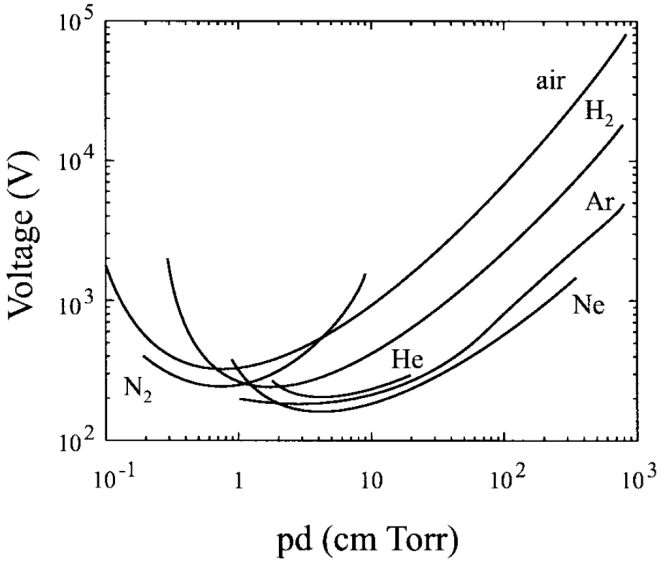

Fig. 2.5 Breakdown potential in various gases as a function of the gap distance and pressure $p \times d$ for plane-parallel electrodes [18].

After the plasma is ignited, it is mainly sustained by electron production from electron-neutral collisions. The discharge can be divided into three regions: (i) the *Townsend mode*, (ii) the *glow discharge mode* which has two sub-modes: α and γ mode, (iii) the *arc mode* [73, 74]. In the Townsend mode, there are low numbers of charge particles after ignition that lead to relatively few excitations of gas.

When more energy is transferred to the charge particles, the excitation and ionisation increase. At this point, the plasma starts its formation. The electrons are accelerated away from the cathode. The ions are left behind and create an electric field with the cathode known as the sheath. Since the accelerated electrons are also induced photon emissions in the sheath region, the sheath becomes a brighter layer. After electrons lose their energy to the ionisation in the sheath region, they are then in the region between the sheath and the anode and are weak effective for inducing further ionisation. As a result, this region has relatively less ionisation and relatively more number of electrons known as the plasma bulk. With these above properties and structures, the plasma gets into the glow discharge mode.

In the glow plasma mode, electrons are still generated by the electron-gas collision. These types of ionizations take place throughout the plasma volume. This is called α *glow discharge mode*. When additional energy is applied to the plasma, the discharge current rises. As a result, the secondary electrons increase and become the dominant number in the discharge process. This leads to the γ *glow discharge mode* and the sheath thickness is also reduced. In γ mode, more number of ionizations happen and make the plasma more conductive. Therefore, the voltage of the plasma volume drops and then results in an increase of discharge glow current.

Although there is an increase of discharge current in the γ mode, there is no reaction to limit this current. This leads to an exponential increase of plasma conductivity. The stable glow mode starts instability and changes to the arc mode. In this mode, a new form of plasma such as narrow channels is generated. Therefore some applied energies are changed to the heat, shock waves, and mechanical movements, which show the instability of the plasma mode. The most stable α glow mode is to be operated for the used atmospheric pressure plasma sources in this work.

2.4.2 Atmospheric pressure plasma sources for biomedical applications

Commonly, plasma generations are excited by an AC excitation in a sinusoidal waveform at the frequency ranging from a few hertz to a few tens of gigahertz [75] as shown in figure 2.6. Breakdown voltage, which ignites plasma inside the gap, is inversely proportional to the excitation frequency [76]. At below the frequency of 1 kHz, the plasma is ignited by the high breakdown voltage with some energetic electrons. These electrons are still accelerated over a half-period of these low frequencies. With long excitation period compared to higher frequency, relatively large amount of energy is transferred to the plasma through the coupling of electrons and excitation frequency. As a result, gas temperature is too high for plasma biomedical applications in this frequency range.

For higher frequencies over 30 MHz, when most of electrons are kept inside plasma bulk and more energy is transferred through electron with many cycles of excitation frequency, the gas temperature also rises to a higher level. In order to operate atmospheric pressure plasmas with gas temperature below 150 °C, the common frequencies are between 1 kHz and 30 MHz. After a few decades of research and development of non-thermal atmospheric pressure plasma sources, these sources are mainly categorized by the excitation frequencies with differences in discharge configuration as shown in figure 2.7. The cross and linear field configurations [77] are compared in figure 2.7 (a) and the configuration of two-frequency

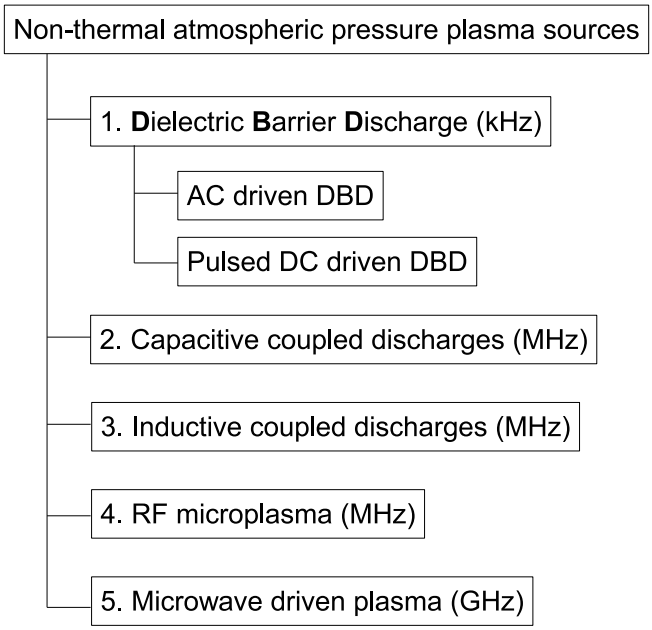

Fig. 2.6 Non-thermal plasma categorized by frequencies.

driven DBD jet is shown in figure 2.7 (b) [78]. In figure 2.7 (c), the separated ground electrode configuration has been studied for the operational modes [79]. Additionally, the capacitively coupling discharged reference μAPPJ has been established [54, 80] as shown in figure 2.7 (d).

Since the sources are very different in terms of structure, power supply, plasma temperature and working condition, they have various applications. Most of them are still under development in laboratories. The applications of different atmospheric pressure plasma sources include gas cleaning, chemical-conversion production, surface treatments, surface coating, and biomedicine, for which an overview can be found in [65]. In this work, we focus on the biomedical applications and CO_2-CO conversion. The main aim is to study the reactive species densities as a function of plasma parameters related to the responsive biological effects and chemical products. Various APPJs have been invented and studied for their plasma and operational characteristics. In table 2.3, examples of each type APPJs, which have long-term development and use different diagnostic approaches for biomedical parameters characterisations are presented.

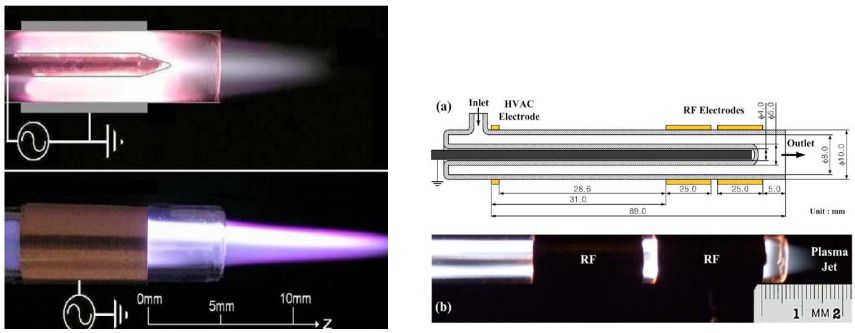

Fig. 2.7 Different aspects of APPJs (a) cross-field and linear field [77], (b) kHz-RF DBD APPJ [78], (c) APPJ with separated ground electrode [79], and (d) capacitively-coupled RF-driven μAPPJ [54, 80].

Table 2.3 Details of some low-temperature atmospheric pressure plasma sources for biomedical applications.

Excitation	Source	Plasma characteristics	Observations
Pulsed DC	DBD APPJ [81]	15 kV 600 ns pulse width	OH, N_2 by optical emission spectrum
	inner rod and outer ring	25 kHz repetition rate	O_3 by sensor device
	cross-field	T_e = 1 eV, $T_g \approx$ 373 K	
		Ar with air admixture	
	Plasma Pencil [82]	10 kV, pulse width 200 ns to DC	Plasma bullet by ICCD camera
	two ring electrodes	He and Ar	I-V characteristic
	linear-field		For sterilization, dental-bacteria
			inactivation [83]
AC-kHz DBD	APGD plume [84]	30 kVpp, 8 - 30 kHz,	an insignificant role of UV in
		Ar, N_2, O_2 and air, $T_g \leq$ 320 K.	organic contaminant degradation
	Corona DBD [85]	0-2 kV, 30 - 70 kHz	Electrical characteristic and
	pin to plane electrode	He gas, $T_g \leq$ 490 K	rotational gas temperature
13.56 MHz RF	COST Reference	$T_e \approx$ 1 - 2 eV	O, He^*, SDO densities have been studied
	Microplasma Jet [80]	He/O_2, He/H_2O	[36, 58, 86]
	Plasma needle [87]	He, Ar , N with air admixture,	NO densities by mass spectrometry [88]
		$T_g \approx$ 300 - 500 K	To manipulate eukaryotic cells
		at plasma power 2 - 8 W	and kill bacteria
	APGD torch [89]	He, duty-cycle modulated	active species in the downstream zone
		$T_g \approx$ 323 K	surface treatments

The used atmospheric-pressure plasma sources in this work are the Radio-frequency driven capacitively-coupled APPJ and the DBD kHz-driven APPJ. The physics of their plasmas are discussed in the following parts and their specific configurations will be explained in the later chapters.

2.4.3 Radio-frequency driven capacitively-coupled APPJ

Concept of capacitively-coupled atmospheric-pressure RF plasma in this section was deduced from fundamental of low-pressure RF plasma [66]. This will give a simplified picture of its principle. Additionally, the different characteristics in atmospheric-pressure regime will then be addressed.

In low pressure, the plasma description can be expressed by equivalent-circuit models, which focus on the impedances of the plasma and sheath structures. These impedances, which directly relate to the voltages and current, can be derived from the integration of local RF electromagnetic field. Therefore, the analysis descriptions are expressed in terms of the RF voltage and current instead of RF electromagnetic fields and also conveniently compared with the measurements.

Consider two parallel plates with each surface area A, an RF voltage $V_{rf}(t) = V_0 \sin \omega t$ with RF current, $I_{RF} = -I_0 \sin \omega t$, is connected to the powered electrode as presented in figure 2.8 [66]. Another electrode is grounded. Here, ω is frequency, V_0 and I_0 are the voltage and current amplitudes of the RF power supply, respectively. A plasma is formed between the electrodes constituted of the plasma bulk and space charge sheaths such that the thickness varies at the radio frequency.

In figure 2.8, a quasi-neutral plasma expands over distance d and is separated by the time-varying sheath thickness $s_a(t)$ and $s_b(t)$. The electric field in quasi-neutral plasma is approximated to be zero or much smaller than in the sheaths. However, at atmospheric pressure plasma, the electric fields in both regions are comparable [73]. In sheath a ($0 \leq x \leq s_a(t)$), electric field, $E_a(x,t)$, and potential, $\phi(x,t)$, can be expressed by equation 2.15 and 2.16.

$$E_a(x,t) = \frac{n_0 e}{\varepsilon_0}[x - s_a(t)] \tag{2.15}$$

$$\phi(x,t) = -\frac{n_0 e}{\varepsilon_0}\left[\frac{x^2}{2} - s_a(t)x\right] + V_{ab}(t) \tag{2.16}$$

where $\phi(0,t) = V_{ab}(t)$, n_0 is the plasma density at the discharge center and ε_0 is the

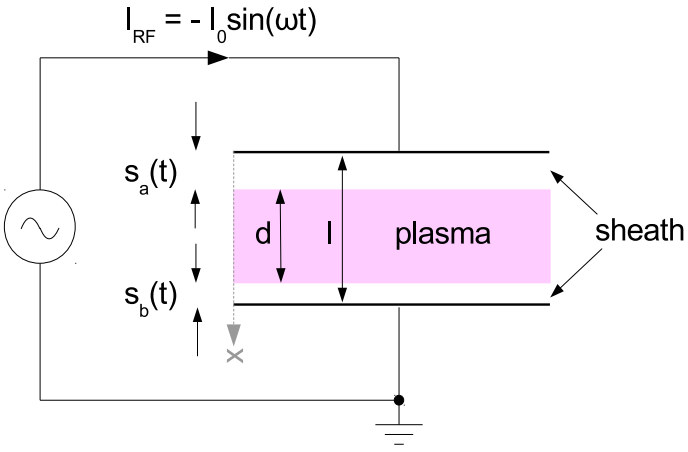

Fig. 2.8 RF capacitive discharge model with the sheath and plasma bulk dynamics between two parallel electrodes [66].

vacuum permittivity. Then, in the plasma region, the electric field is zero corresponding to the low-pressure regime assumption. The potential at the plasma/sheath boundary, $s_a(t) < x < s_b(t)$, can be expressed as

$$\phi_p(x,t) = +\frac{n_0 e}{\varepsilon_0} s_a(t)^2 + V_{ab}(t) \tag{2.17}$$

In sheath b, $s_b(t) \leq x \leq l$, the electric field and potential can be obtained by equation

$$E_b(x,t) = \frac{n_0 e}{\varepsilon_0}[x - s_b(t)] \tag{2.18}$$

$$\phi(x,t) = -\frac{n_0 e}{\varepsilon_0}\left[\frac{x^2}{2} - s_b(t)x + \frac{s_b(t)^2}{2}\right] + \phi_p(t) \tag{2.19}$$

Finally the potential between the electrodes, $V_{ab}(t)$ can be expressed as

$$V_{ab}(t) = V_0 \cos \omega t \tag{2.20}$$

where $V_0 = 2n_0 e s_0^2/\varepsilon_0$ and s_0 is the amplitude of the sheath motion.

According to the structure of the plasmas, it is convenient to construct the equivalent electrical circuit. The common electrical components are matched to the properties of the plasmas. Two plasma sheaths can be modeled by a single capacitance and resistances which represent the power dissipation. The capacitance, C_s, can be determined by differentiation

of voltage in equation 2.20 and is defined by equation 2.22.

$$\frac{dV_{ab}}{dt} = -\omega V_0 \sin \omega t = -\frac{2s_0}{\varepsilon_0 A} I_0 \sin \omega t \tag{2.21}$$

$$C_s = \frac{\varepsilon_0 A}{2s_0} = \frac{n_0 e \omega \varepsilon_0 A^2}{2I_0} \tag{2.22}$$

The power dissipation due to the resistance includes the electron heating collisional process (ohmic), $2R_{ohm,sh}$, electron heating collisionless (stochastic), $2R_{stoc}$, and ion acceleration across the sheath, $2R_e$. These components can be expressed in the complex impedance, Z_s, form in equation 2.23.

$$Z_s = \frac{1}{i\omega C_s} + 2(R_i + R_{stoc} + R_{ohm,sh}) \tag{2.23}$$

In the plasma bulk, since $\omega \ll \omega_{pe}$ (the electron plasma frequency), the capacitance which implies the displacement current crossing plasma, is negligible. The electrical components, therefore, compose of a power-resistance in series with an electron inertia inductance, L_p. The voltage of the plasma is formed as $V_p = R_p I_{RF} + L_p \frac{dI_{RF}}{dt}$.

Finally, the total equivalent circuit of the plasma sheaths and bulk is shown in figure 2.9. For the power dissipation, most RF power is absorbed by electrons that responded to the RF fields. On the other hand, ions energy gaining from the fields are negligible in the plasma bulk, but are a significant fraction of sheath region.

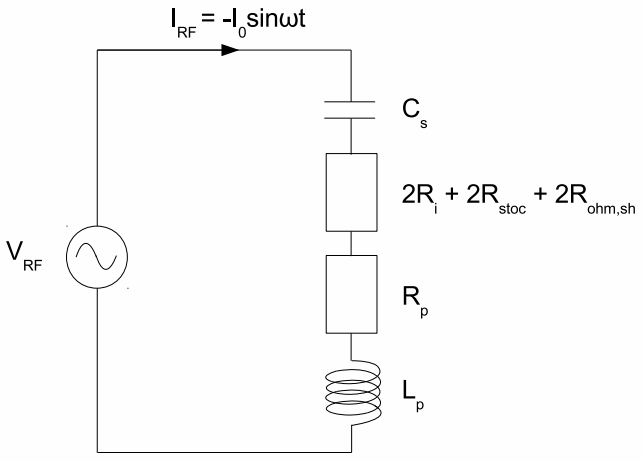

Fig. 2.9 Equivalent circuit of RF capacitive plasma [66].

To complete the equivalent circuit of CCP, the load of plasma source needed to be

matched to a standard generator with 50 Ω output impedance. This must be included in the matching network. The complete circuit of CCP is presented in figure 2.10 when a typical matching circuit composes of two variable capacitances, C_1 and C_2 and inductor, L_m. Moreover, in reality, the power losses in connection components that represented by the resistance R_{loss}, stray series inductance L_{stray} and stray capacitance C_{stray}. The resistance of transmission cable, R_T, is also included.

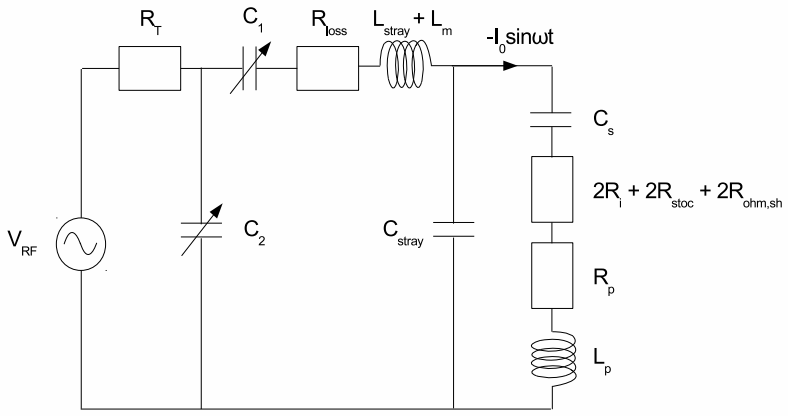

Fig. 2.10 Equivalent circuit of RF capacitive plasma with matching box network [66].

2.4.4 Dielectric barrier discharged (DBD) kHz-frequency driven APPJ

In this section, the principles of DBD kHz-driven atmospheric pressure plasma are summarised from these full description literatures [65, 90]. This discharge has a dielectric layer that covers at least one of the electrodes with the gap between electrodes in millimeters scale. The dielectric acts as an insulator that cannot pass a dc current in the initial stage. With the derivative of the applied voltage and the dielectric constant, these determine the displacement current that can be passed through the dielectric. It requires a high enough electric field to generate gas breakdown and pass current into the discharge gap. The gas breakdown structure comprises of large numbers of micro-discharges at a typical gas pressure of the order of 10^5 Pa. The electric field can be driven by either sinusoidal continuous or pulsed modes. However, the dielectric becomes less effective in current limitation at very high frequency. For these reasons, the DBD is effectively operated in kHz frequency domain with voltage ranging between hundreds volt and several kV.

When an applied electric field is high enough local breakdown in the gap is initiated. It is symbolized by closing a switch and drives the current through the plasma microdischarge

channel with rapid time-variation of its resistance $R(t)$ as shown in figure 2.11. In the local breakdown, growing electron avalanches immediately create high space charge and consequently form the self-propagating streamers. The streamers propagate very fast and are reflected at the anode back to the cathode within 1 ns. At this moment, the current passes through this conductive channel connecting both electrodes. Then, when the charges accumulate at the dielectric surface, the local electric field is reduced. This stops the ionization within a few nanoseconds and constricts the microdischarge. While the applied voltage keep rising, the next microdischarge will likely ignite at other locations outside this area. Hence, the dielectric not only limits the amount of energy and charge coupled into each microdischarge but also at the same time spreads the microdischarge over the electrode surface. This implies that there is no arcing in the electrode gap. The individual microdischarge is limited charges transfer of order of 100 pC and energies at μJ level [91]. Therefore, in the minute of energy dissipation, the local heating effect due to the short current pulse is low and approximately 10 °C in air. The low gas heating effect of microdicharge structure in the DBD discharge makes it one of the preferred option for thermal-sensitive treatment applications.

Furthermore, in order to have homogeneous DBD, the condition with helium gas is also required [92]. He with ten times lower breakdown voltage than dry air easily allows to produce the set of microdischarge. In addition, He which has high-energy metastable states ($\approx$20 eV) and likely to ionise, supports extendedness of microdischarges on dielectric surface. One of the used plasmas is homogeneous DBD kHz-driven type with He as an operational gas.

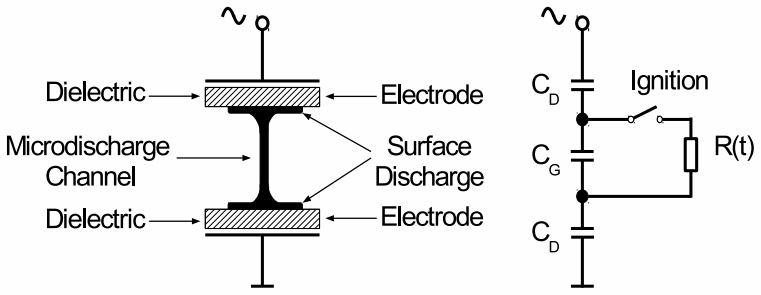

Fig. 2.11 Equivalent circuit of micro-discharge channel in dielectric barrier discharge, where C_D and C_G are the dielectric and gas discharged capacitances, respectively [90].

2.5 Diagnostic techniques

In the previous studies [55, 93, 94], O_3 and OH density have been measured using UV-LED absorption spectroscopy with various parameters in the effluent of the jet. However, there are lacks of O_3 and OH densities as function of fundamental parameters inside the plasma volume. For example, the spatial measurement that shows the development of O_3 equilibrium range in the plasma channel and the density with gas temperature that important for biomedical application. In this section, principles of various employed techniques will briefly discussed.

In the last decades, principles of plasma diagnostic have been established to study the fundamental mechanisms of such complex plasmas [30, 31]. Since then, laboratory plasmas have been widely spread in many different research aspects along with the development of the diagnostic techniques, optical devices, and detection technology. Specific requirements in different plasma regimes and applications motivated the development of technique on established diagnostic principles. In low temperature atmospheric pressure plasmas for biomedical applications, number density of reactive atomic and molecular species are one of the most important parameters.

In fundamental mechanisms of RONS in medicine, nonthermal atmospheric pressure plasmas are found to support wound healing by various effects, for example antiseptic effects, stimulation of proliferation and migration of wound skin cells and inhibition of integrin receptors on the cell surface [95]. For the main species related to this research, ozone plays important role in an inactivation microorganisms (such as bacteria, viruses and fungi), in stimulation oxygen metabolism and in activation of the immune system. For hydroxyl radical (OH), it was reported to be a primarily responsible for dielectric barrier discharge plasma-induced angiogenesis [96]. In this work, we study relation of O_3 and OH densities with fundamental plasma parameters as these species have relatively strong effect on living organisms and significantly contribute to other species' creation and destruction reactions.

O_3 and OH densities can be measured by UV absorption spectroscopy due to their relatively large absorption cross section. Hence, the fundamentals of the absorption for both species are given, while the specific details of the developed technique are explained in later chapters. Furthermore, the main plasma parameter, T_g, which is the dependent factor of many main reaction rates to be measured and correlated to the density. Therefore, the rotational gas temperature determination is discussed as well. Additionally, fundamentals of the main diagnostic devices are included in the final part of this section.

2.5.1 Density from absorption spectroscopy

The absolute density can be determined from the Beer-Lambert law, which is defined as the transmission T(λ) proportional to the exponential decay of the absorbance A(λ).

$$T(\lambda) = \exp(-A(\lambda)) \tag{2.24}$$

For the broadband absorption spectrum of O_3, equation 2.24 can be expressed as

$$\frac{I_T(\lambda)}{I_0(\lambda)} = \exp(-\sigma(\lambda,T)\cdot L\cdot n_{O_3}) \tag{2.25}$$

For the resonant absorption spectrum for OH density, the Einstein absorption coefficient and the normalize line profile for each spectral line are required. So, the absorbance can be expressed as

$$\frac{I_T(\lambda)}{I_0(\lambda)} = \exp(-h\lambda B(\lambda)\phi(\lambda)\cdot L\cdot n_{OH}) \tag{2.26}$$

In equation 2.25, $T(\lambda)$ can be defined as the ratio of the transmitted, $I_T(\lambda)$, and incident, $I_0(\lambda)$, intensities of the UV light as shown in figure 2.12. The absorbance is defined in terms of the absorption cross section with the function of wavelength and temperature, $\sigma(\lambda,T)$, the absorption length, L, and the ozone density, n_{O_3}. This case is appropriate for the broadband absorption spectrum. However, with the resonant absorption spectrum of OH density, each spectral line requires more details of the line profile as shown in equation 2.26, where h is the Planck constant, λ is the center wavelength, $B(\lambda)$ is the absorption coefficient, $\phi(\lambda)$ is the normalized line profile, L is the absorption length, and n_{OH} is the OH density in the ground state level. The general definition of B and description of equation 2.26 can be found in [97]. The specific details related to the experimental setup for O_3 and OH densities will be given in section 3.1 and 7.1, respectively.

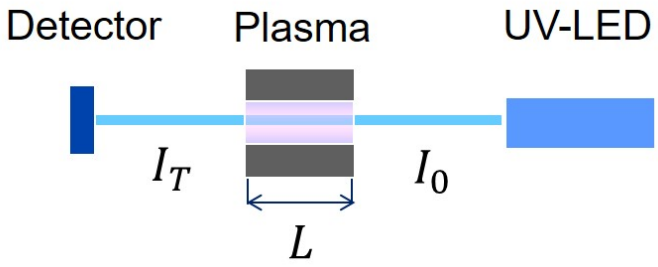

Fig. 2.12 Schematic of simple absorption spectroscopy.

2.5.2 Rotational gas temperature

There are many techniques used to determine the gas temperature, such as Rayleigh scattering, laser-induced fluorescence [98], Raman scattering [99], optical emission spectroscopy and thermal probes. One of the most commonly used techniques is optical emission spectroscopy, which is based on the emission spectral line profiles. According to [70], atomic and molecular transitions can radiate at a specific wavelength corresponding to the energy transfer between the upper and lower levels. Practically, the emission, or absorption transition always includes spectral width, which is induced by different mechanisms. These usually are the finite lifetime of the states (natural broadening), Doppler broadening, Stark broadening and van der Waals broadening or resonance broadening (pressure broadening). However, each effect is significant in different regimes.

At low gas temperature and atmospheric pressure, the van der Waals broadening significantly contributes to a line profile, resulting in the Lorentzian shape. When pressure is assumed to be constant, the gas temperature can be obtained from the FWHM of a Lorentzian line profile (w_{vdW}) [70, 100].

$$w_{vdW} = A\frac{p}{T_g^{0.7}} \tag{2.27}$$

where A is a constant depending on the radiator, collision partner and transition.

One of commonly used excited states for gas temperature determination is the rotational spectrum of N_2 ($C\ ^3\Pi_u^+ \rightarrow B\ ^3\Pi_g^+$, $\upsilon = 0 \rightarrow 2$) at 380 nm, which is called the second positive system of nitrogen. Basically, the rotational temperature equals the gas temperature based on the assumption that a translation-rotational equilibrium exists. The equilibrium can be reached when fast rotational energy transfer (RET) occurs. In atmospheric pressure, collisions between a excited diatomic molecule and background gas occur during its lifetime. These collisions thermalised a rotational population distribution (lowest rotational level) before the emission. Under this approximation, a thermal distribution of $N_2(C)$ can be achieved. Therefore, the rotational temperature of $N_2(C)$ is preferably used for gas temperature determination in atmospheric pressure plasma. The detailed description can be found in [70], and the related experimental technique is discussed in section 4.2.

2.5.3 Spectroscopic instruments and detectors

In this section, all fundamental concepts are summarised based on [97] that covers relatively modern technology on plasma spectroscopy.

Basic spectroscopic principle

The basic schematic of a spectrometer is illustrated in figure 2.13 [97]. It composes of an entrance slit (width w_{en}, area A_E), a dispersive element, an optical system, and a detector in the exit plane. The angular dispersion is defined by equation 2.28, which characterizes the dispersive elements.

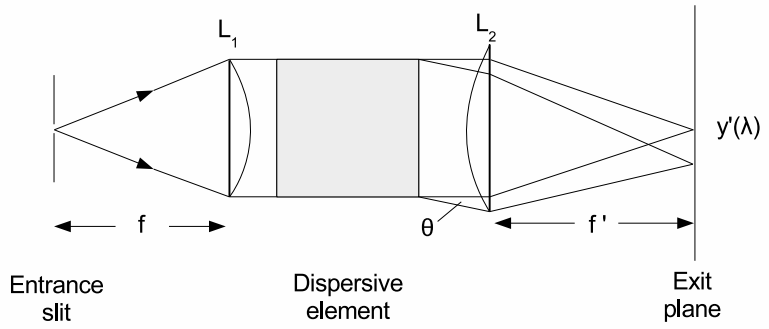

Fig. 2.13 Schematic of a spectrometer with details for basic spectroscopic principle [97].

$$\frac{d\beta}{d\lambda} \tag{2.28}$$

where dβ is the different angle between the transmitted and the incident optical path directions to a different wavelength dλ in unit of rad/mm. At the focal plane, the beam which diffracts from the dispersive element with angle θ is focused by L_2 at $y' = f' \tan\theta$. The separation of different wavelengths in the focal plane is therefore defined by equation 2.29.

$$\frac{dy'}{d\lambda} = -\frac{f'}{\cos^2\theta}\frac{d\beta}{d\lambda} \tag{2.29}$$

Furthermore, the resolving power R is defined as a minimum separation $\delta\lambda$ of the central wavelengths of two closely spaced equally intense lines and can be expressed by equation 2.30.

$$R = \frac{\lambda}{\delta\lambda} \tag{2.30}$$

The optical system forms an image at the entrance slit to the exit plane. Due to the paths and structure of the instrument elements, the shape of the line can be produced, which is called the *apparatus profile*. The image of the slit width, w_{en}, is broadened by the me-

chanical defects, optical aberrations and diffraction at the edge of the dispersive element. Narrowing the entrance slit width reduces the spectral line width and maximizes the resolving power.

Czerny-Turner spectrometer

In this work, the used spectrometer is Czerny-Turner mount type and the schematic is shown in figure 2.14. Principally, two adjacent mirrors are used, one to collimate the light from the entrance slit to the grating and another to focus the dispersive light from the grating to the exit slit.

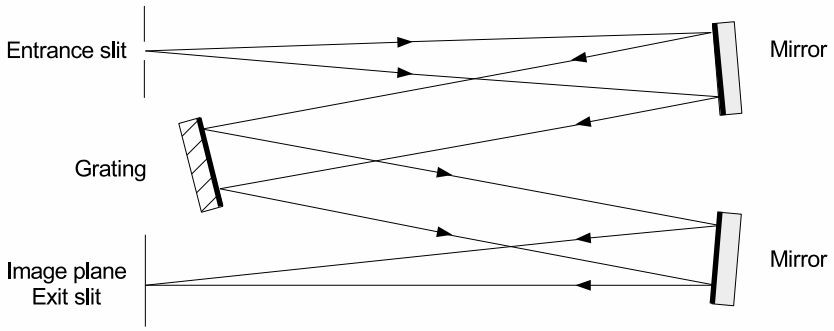

Fig. 2.14 Schematic of Czerny Turner mount [97].

For the dispersive element, the diffraction, transmission and reflection gratings are the general types of the grating. The used grating is the reflection plane grating. It consists of equally spaced identical structures, which are called grooves. It is produced by mechanical ruling technique that shapes the groove into a triangle and is finally coated with a thin reflecting metallic layer. This grating is called a ruled diffracting grating as shown in figure 2.15

The fundamental grating equation can be expressed in equation 2.31. The parallel beam from the collimating mirror incidents the grating at the angle α. The principal maxima of the diffraction which gives the spectral lines are at angle β.

$$m\lambda = d(\sin\alpha + \sin\beta) \tag{2.31}$$

where m is the diffraction order and d is the groove spacing. A commercial spectrometer usually provides groove density $1/d$ in grooves or lines per millimeter. Theoretically, the

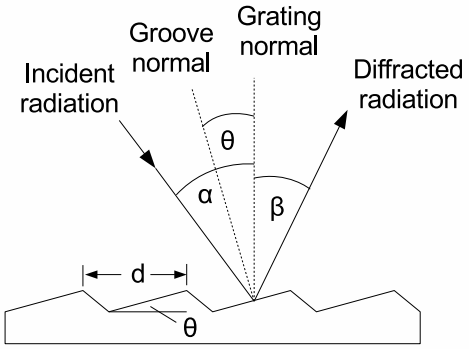

Fig. 2.15 Profile of a ruled diffracting grating [97].

resolving power of a grating is defined as

$$R = mN = W\frac{m}{d} \tag{2.32}$$

where N is the total number of illuminated grooves and W is the illuminated width of the grating. The higher spectral resolution can be achieved by higher number density of grooves. As the grating width defined as $W = Nd$, the resolving power R is obviously limited by the groove spacing and the grating width. However, the resolving power can be limited by non-diffraction theoretical factors such as slit width, detection pixel size and quality of the spectrograph optics. Suppose the spectrum is an infinite number of images of the slit width projected on the detector slightly shifted in wavelength; in order to maximize the spectral resolution, the slit width should be as narrow as possible, ideally less than the diffraction limit of the spectrograph. On the other hand, too narrow a slit reduces the detection signal or loses part of object image. Therefore, the optimization usually is taken into account as discussed in following chapter for the developed setup.

CCD camera

Two-dimensional charge coupled device (CCD) detectors compose of the basic elements which are called pixels. Each pixel is made up of metal-oxide-semiconductor (MOS) capacitor on a doped silicon substrate [97]. Silicon dioxide acts as an insulator. When a voltage is applied and photons are absorbed, electrons and holes are created. These are collected and change the charge on each MOS capacitor. The pulse-modulated voltage then transfers the charge packets through the pixel array until the last pixel of the row. Each voltage change is read by an A/D converter and stored for the data processing step. The readout time of CCD

detectors can be varied depending on the required condition such as signal-to-noise ratio, operational time and detection limit.

LED source

In this low absorption 10^{-3}, the statistical average over the long period of time is one approach to improving the signal-to-noise ratio. The baseline drift of the light source can limit the possibility of this improvement of the experiment. Therefore, the stable light source is crucial. The UV-LEDs, which provide more advantages than UV lamps [101], are used in this work. First, the UV-LEDs are monochromatic, providing only a specific wavelength. There is no need for a filter, as in the case of UV lamps, leading to less additional optical devices and lower costs to measure at a very specific wavelength.

Second, UV-LEDs have a short on/off cycle, consuming less energy and providing longer replacement periods. Their full brightness and stability can be reached within a microsecond due to efficient management of junction temperature and power supply operation. On the other hand, UV lamps cannot be switched on and off instantly and more factors affect the stability.

Third, LEDs are driven by lower currents that easily to be regulated through the LED. However, UV lamps require higher voltages and more complex power supplies and electronic controlling units. This also implies the benefits in safety, thermal control, cost and ease of operation perspectives.

Chapter 3

Two-beam UV-LED Absorption Spectroscopy

In atmospheric pressure plasmas, the electrode separation is typically in the order of micrometres to millimetres, leading to small plasma volumes [53]. With regard to diagnostics, these relatively small-scaled plasma volumes are a challenge and require sensitive non-intrusive measurement techniques. The aim of the developing two-beam UV-LED absorption spectroscopy in this chapter is to overcome these challenges.

Various spectroscopic methods have been employed to investigate densities of short-lived RONS [42, 43, 48, 102, 103]. For example, atomic oxygen densities have been measured using two-photon absorption laser-induced fluorescence (TALIF) spectroscopy [86], VUV synchrotron absorption spectroscopy [34], and energy resolved actinometry (ERA) [35]. Singlet delta oxygen densities have been measured using infrared optical emission spectroscopy [36, 37].

O_3 is a long-lived reactive species in the complex reaction chain of short-lived oxygen atoms and excited molecules produced in the active plasma region. Included with some theoretical predictions of important coefficients, this leads to a large uncertainty of ozone density in plasma chemistry model simulation [51]. Alongside with the experimental aspect, less than 1% concentration of ozone is found to be in a sensitive regime by non-plasma parameter disturbance. Furthermore, the precise tailoring of the delivered production of APPJs to match the requirement in biomedical applications is highly required. Therefore, a very precise diagnostic tool for ozone density is essential.

UV absorption spectroscopy is fundamentally used to measure O_3 density due to a relatively large UV absorption cross section around 255 nm (Hartley band) in order of 10^{-17} cm^2 [52] and it is independent of quenching data [104]. Recently, O_3 densities in APP

have been experimentally and numerically investigated under different plasma conditions, for example in an argon background gas [55] or in the effluent in air [54, 93, 105, 106].

To obtain the fundamentals of plasma chemical kinetics, ozone density inside the plasma channel needed to be measured directly. However, it is found to be quite challenging due to the spatial variation of ozone density and its low signal within short single-pass absorption length. Furthermore, with a mm gap, a large electrode temperature variation introduced a significant fluctuation on the signal. Therefore, UV absorption spectroscopy have developed in Mach-Zehnder configuration as we called two-beam UV-LED setup for improving signal-to-noise ratio and suppressed non-plasma parameter factor. Consequently, the developed setup is able to measure O_3 in this typical high-sensitivity level and also in spatial-resolved variation in the investigated single-pass small-absorbance regime.

3.1 O_3 density by UV-LED absorption spectroscopy

According to Beer-Lambert's law, equation 2.25, the absorption ratio can be expressed in the experimental perspective as

$$\frac{I_T(\lambda)}{I_0(\lambda)} = \frac{I_{PL}(\lambda) - I_P(\lambda)}{I_L(\lambda) - I_{BG}(\lambda)} = \exp(-\sigma(\lambda, T) \cdot L \cdot n_{O_3}) \tag{3.1}$$

where all quantities are listed in table 3.1

Table 3.1 Details of calculation notations for O_3 density.

Notations	Quantities	Values and Conditions
n_{O_3}	Density	cm^{-3}
L	Plasma absorption length	11 mm [34]
$\sigma(T, \lambda)$	Ozone cross-section	wavelength variation [107] and approximately temperature constant
I_T	Transmitted intensity of the probe beam	
I_0	Incident intensity of the probe beam	
I_{PL}	UV-LED light and plasma background	UV-LED on and plasma on
I_P	Plasma background	UV-LED off and plasma on
I_L	UV-LED light	UV-LED on and plasma off
I_{BG}	Room background	UV-LED off and plasma off

The absorption cross section of O_3 is shown in figure 3.1 [52]. The largest absorption cross section is in the Hartley band with the centre wavelength $\lambda = 254 - 255$ nm. The absorption changes 1.14% from temperature 229 K to 295 K [108] and about 0.86% from

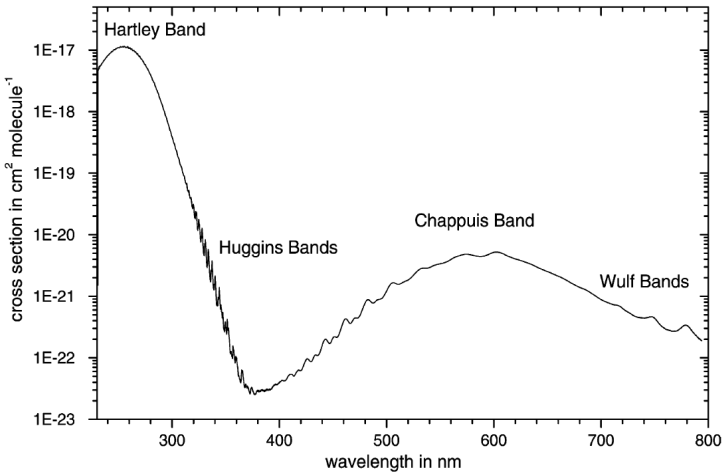

Fig. 3.1 Ozone absorption cross section from 240 - 790 nm shows the highest value at Hartley band around 255 nm [52].

226 K to 298 K [107], which is relatively not temperature sensitive. However, the cross section is more wavelength dependent up to 8% between 250 - 260 nm [52, 107]. In this work, the O_3 absorption cross section is approximately temperature constant and wavelength dependent. The values are between 1.080 and 1.173 $\times$ 10^{-17} cm^2 at wavelength from 249.5 to 260.5 nm [107].

In this typical plasma, He with 0.5% O_2, O_3 is created and only a fraction of the incident light will be absorbed by O_3 density. The absorption is approximated by about 1%, and it is sensitive to any external influence. Therefore, the setup will need a very stable light source and additional technique to reduce these relatively large effects on the experiment.

3.2 UV-LED Absorption setup and optical alignment

According to the effective ozone cross section in Hartley band, the UV-LED light source (UVTOP, 255-TO18-FW) is narrowband spectrum with the centre wavelength at 255 nm and full-width half-max (FWHM) at 11 nm as shown in figure 3.2. It is attached to a mounting head that is actively temperature-controlled through a piezo element, and driven by a stabilized current/power supply unit (Thorlabs, LTC100). The typical LED current is 20 mA, the typical optical output power is 150 μW, and the stability of the current supply is specified to be better than 10^{-4}.

UV-LED at light source position in figure 3.3 (a) was imaged 1:1 by 100-mm focusing lens (L1) and aligned through the vertically orientated plasma channel. From the plasma

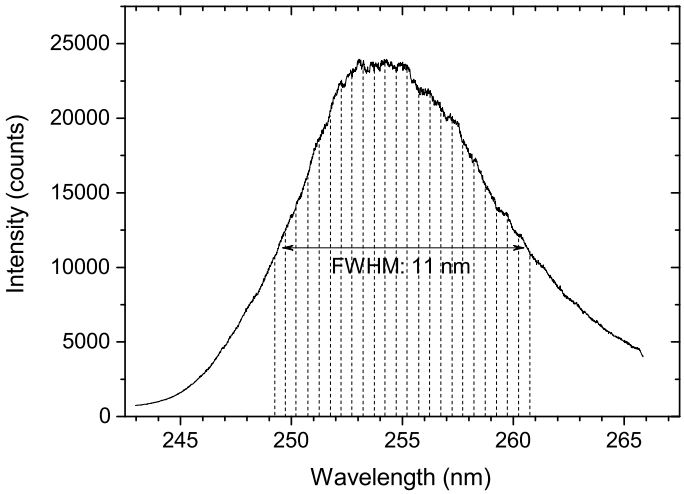

Fig. 3.2 Measured spectrum of the UV-LED and region of interest (ROI) defined by 11-nm FWHM.

source position, 1:1 was projected with an identical lens (L2) onto the vertically orientated entrance slit of the spectrograph via the reflection from mirrors (M1). This represents the *probe beam* (green solid path). Additional mirrors (M2), beam-splitters (BS1, BS2), and a third lens (L3) are used to symmetrically couple out a *reference beam* of similar intensity that bypasses the plasma source. In order to recognise two beams, the reference beam was shifted its vertical position higher than the probe beam by the adjusting mounting angle of BS1 and MR2, as shown in figure 3.3 (b). Both beams are fully separated by a horizontal blocking aperture in front of the entrance slit.

Based on the absorption theory, four quantities need to be measured. Three modulation frequencies were used to operate and control the light source, plasma source and the camera as shown in figure 3.4.

3.3 Data acquisition

In order to measure the optical transmission of the plasma in terms of the required four quantities (I_{PL}, I_P, I_L, and I_{BG}) with correction for the thermal and readout noise of the CCD camera, we make use of four 'switches': An opto-mechanical shutter for the LED, an TTL input for RF generator on/off operation, an opto-mechanical shutter behind the entrance slit of the spectrograph that blocks all incoming light onto the CCD camera chip, and the camera acquisition trigger input. The temporal triggering scheme as utilized with

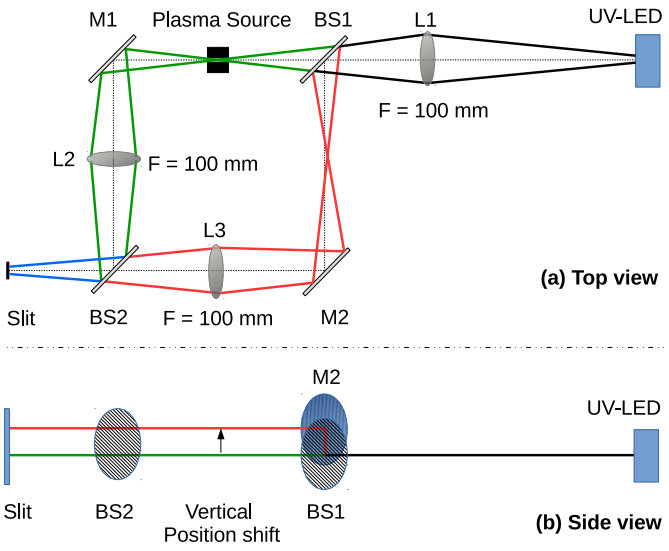

Fig. 3.3 Optical alignment in Mach-Zehnder configuration illustrated details of beam path.

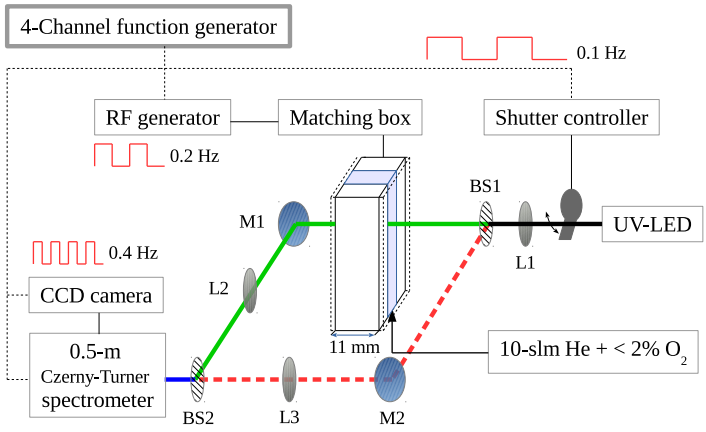

Fig. 3.4 Schematic of UV-LED absorption setup.

a 4-channel arbitrary function generator (TTi, TGA 12104, 100 MHz sine) is illustrated in figure 3.5. Note, the shutter behind the slit is ON for a CCD camera chip exposure time of 1.2 s and is OFF for the corresponding chip readout time of 1.29 s. The former was chosen to be much longer than the response time of the opto-mechanical switches (typically 10 ms) and the plasma build-up time (a few milliseconds).

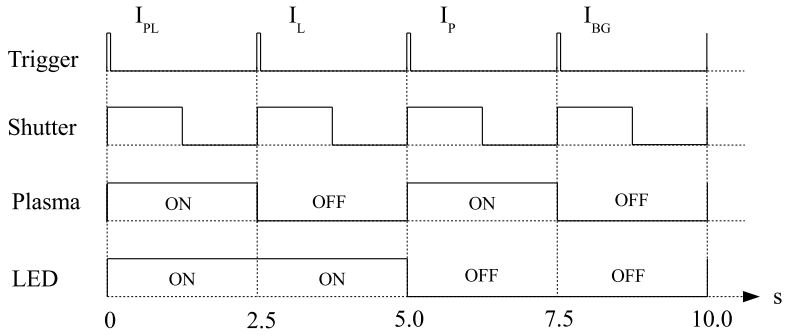

Fig. 3.5 Triggering scheme for measuring the four quantities.

With these optical alignment and synchronization of modulation frequencies, both beams and four quantities were imaged onto the spectrograph entrance slit. The used spectrograph is a 0.5 m-Czerny-Turner imaging spectrograph (Andor, SR-500i) equipped with AL + MgF_2 coated optics including a ruled 2400 lines/mm grating that is blazed for λ = 300 nm. Attached to the spectrograph is a non-intensified CCD camera (Andor, Newton DU940P-BU2, 2048 $\times$ 512 pixels of 13.5 μm x 13.5 μm size) providing high and spectrally constant quantum efficiency of about (60 $\pm$ 10)% in the relevant spectral range, low-noise fast-readout electronics (1 MHz at 16 bit), as well as low dark current due to internal cooling (here -80 °C).

The reference beam goes onto the lower half of CCD chip, rows 0-256, and the probe beam is imaged on the upper part, rows 257-512. The spectrograph's grating disperses the incoming light in the horizontal direction onto 2048 pixel columns, which relate to a wavelength range of about 23 nm, (see figure 3.6).

For the ozone broadband absorption measurement the CCD chip samples the vertically separated probe and reference beams within the entrance slit height of 14 mm over a spectral interval from about 243 to 266 nm, see figure 3.6. The width of the entrance slit was adjusted to 950 μm resulting in a spectral resolution of 0.30 nm. The spectra of the probe and reference beam on the CCD chip appear to be displaced by about 0.4 nm, as a result of imperfect alignment. The required probe beam intensity values (I_{PL}, I_P, I_L, and I_{BG}) were obtained by summing-up the recorded pixel counts within the relevant areas (**R**egions **O**f

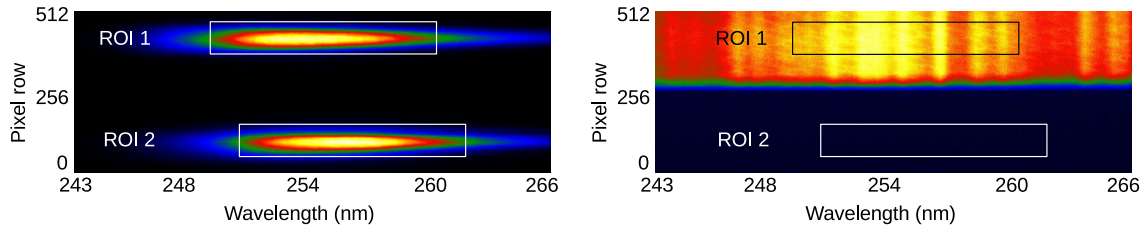

(a) I_{PL} (b) I_P

(c) I_L (d) I_{BG}

Fig. 3.6 CCD images of probe beam (pixel row 370-470 (ROI 1)) and reference beam (pixel row 40-140 (ROI 2)) intensities obtained with (a) LED and plasma, (b) plasma only, (c) LED only, and (d) without LED and plasma. (The colour indicate the counts per pixel on a linear colour scale from min(blue)-to-max(yellow) value, respectively.)

Interest) of the CCD chip and by subtracting the corresponding value for the thermal- and readout-noise of the camera that is obtained from the subsequent spectrograph shutter-off interval, respectively. The ROI was chosen to cover the full spatial beam profile in vertical direction and the spectral full-width at half maximum (about 11 nm) in horizontal direction, as illustrated in figure 3.6a. The same procedure was applied to derive the corresponding reference beam intensity values ROI 2 (I_{PL-ref}, I_{P-ref}, I_{L-ref}, and I_{BG-ref}) that provide additional insight in stability and drifts of the experimental setup.

3.4 Two-beam technique

Monitoring the probe and reference beam intensities over time allows us to access the stability of the experimental setup as well as to identify warm-up time and drift of individual components. In figure 3.7, after switching-off steady-state plasma operation, the I_L was relatively strongly drifted over time due to the changes of conditions inside the plasma source. It was indicated by the change of electrode temperature from 313 K to 294 K (room temperature) measured at a side of power electrode by infrared thermometer (Precision GOLD, N85FR).

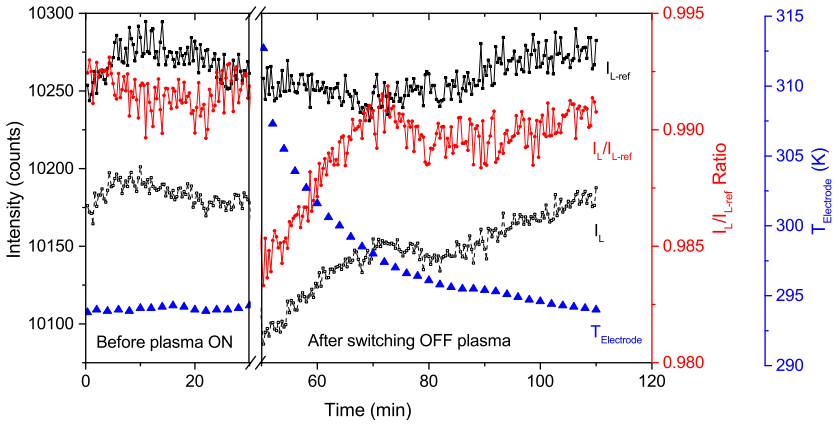

Fig. 3.7 Time-dependence measurements of probe UV-LED intensity (I_L), reference UV-LED intensity (I_{L-ref}), I_L/I_{L-ref} ratio and corresponding electrode temperature monitored before and after switching-off 'steady-state' plasma operation.

In order to suppress the large drift and to reduce the operational time, one image of each four quantities was designed to be measured within a few seconds time period. This was optimised with reasonable readout time, number of averaging and minimum noise level of the detector, where the details are described in the following paragraphs. In addition, the I_L warm-up time was 30 minutes indicated by the absolute value of the intensity level as shown in figure 3.8.

In the steady electrode temperature period, the constant ratio of both beams as shown in figure 3.7 has been taken into account for the transmission $T(\lambda)$ of O_3 density by equation 3.2 or two-beam ratio calculation.

$$T(\lambda) = \frac{I_T(\lambda)}{I_0(\lambda)} = \frac{\left(\frac{I_{PL}-I_P}{I_{PL-ref}-I_{P-ref}}\right)}{\left(\frac{I_L-I_{BG}}{I_{L-ref}-I_{BG-ref}}\right)} \tag{3.2}$$

A single sample for each of the four quantities (I_{PL}, I_P, I_L, and I_{BG}) and the respective ozone density value, according to equation 3.2, is obtained from one full triggering cycle of 10 s (see figure 3.5). In this contribution, 50 consecutive samples were recorded over a total duration of 8 min 20 s and statistically averaged to derive our stated ozone density results.

In one-beam system, since the condition between the electrode gap is relatively varied compared to other quantities, this directly effects the intensity of the probe beam going through the gap. These hence are the main source of the uncertainty in one-beam system. In

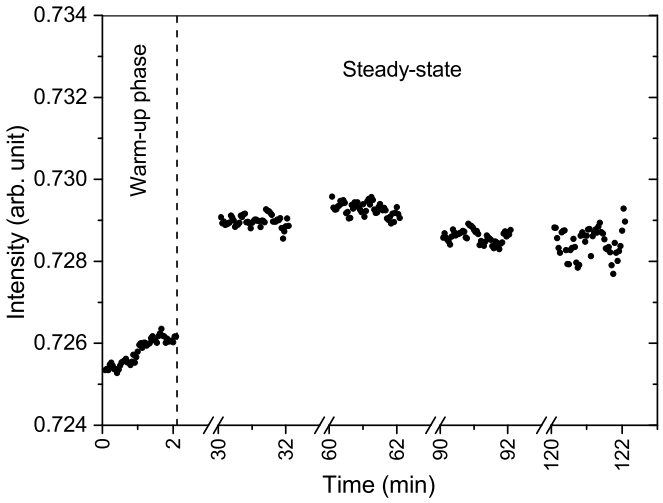

Fig. 3.8 Probe beam intensities I_L monitored from switching-on the LED supply/control unit and optical detection system (no plasma).

two-beam system, the ratio technique significantly cancelled out the fluctuation of the probe beam and O_3 density compared to one-beam direct calculation as shown in figure 3.9.

For this example case, at 6 W RF power and 10 slm He with 0.1% O_2, O_3 density from one-beam direct calculation was $7.75 \pm 3.06 \times 10^{13}$ cm^{-3} compared to $7.62 \pm 0.89 \times 10^{13}$ cm^{-3} of the ratio calculation. Obviously, the two-beam ratio calculation significantly reduced the standard deviation by a factor of 3 or into one order magnitude below the density. Over all the measurement range, the average uncertainty is about 1.0 - 0.9 $\times$ 10^{13} cm^{-3}. Therefore, at 11 mm absorption length, the detection limit of this developed technique is suggested to be at 0.9 $\times$ 10^{14} cm^{-3} with one order magnitude of the uncertainty lower. In previous studies [55, 93, 94], the main focuses are the measurement of spatial O_3 density in the effluent and the Abel inversion technique. The O_3 density is relatively high compared to inside the plasma channel and the sensitivity of the measurement. So, there is no significant information of the relation between the uncertainty of the system and the measured density which can directly be compared with the developed two-beam technique.

3.5 Spatially resolved O_3 density measurement

The capacitively-coupled RF plasma is generated between 1 mm electrode gap along 30 mm of plasma channel enclosed by UV transparent window along the channel side. The electrodes of 11 mm width are defined as an absorption length, which the details of the

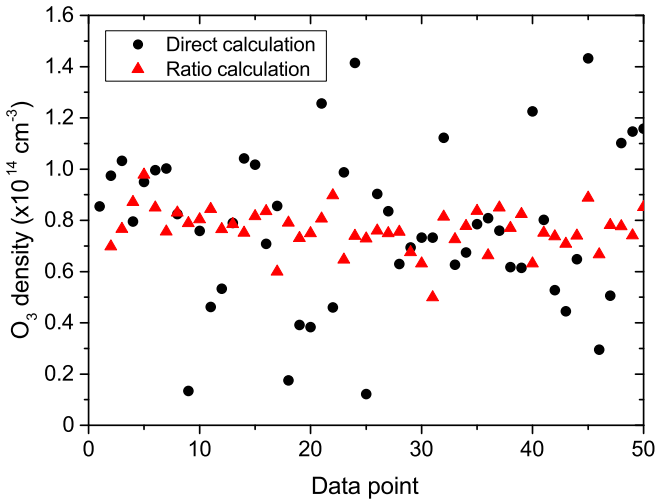

Fig. 3.9 Comparison between 50 data points of O_3 density by direct calculation (one-beam system) and two-beam ratio calculation (two-beam system) measured at 6 W RF power, 10 slm He with 0.1% O_2.

source are given in section 4.1. The plasma source, which was attached to a three axis manipulation stage (Zaber, XY series with built-in Controllers) was able to measure the spatial resolved O_3 density along the 30-mm long plasma channel as seen in figure 3.10. As a result, the O_3 density rose up linearly from the gas inlet side to the centre. Then, the equilibrium range started from -15 mm away from the nozzle where the probe beam position used for all other measurements (presented in this work) was -7.5 mm, so (in) the centre of the plateau.

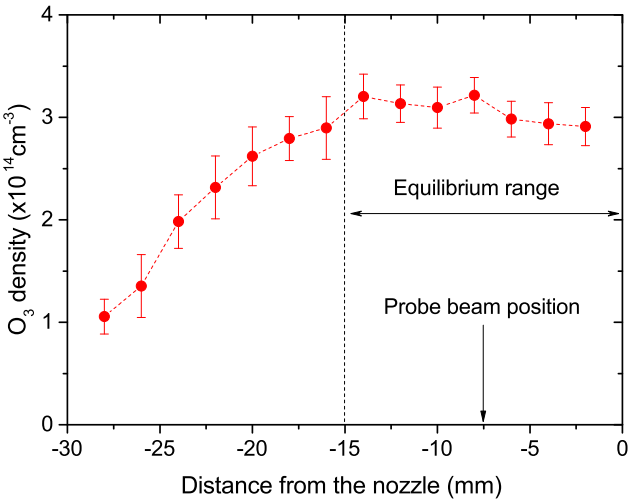

Fig. 3.10 Spatial resolved O_3 density along the 30-mm long plasma channel and probe beam position. He-flux 10 slm, O_2 admixture 0.5 %, rf-power 15 W.

Chapter 4

O_3 Density Measurements

Cold atmospheric-pressure plasmas, known as an efficient source to control and create reactive species, normally operate at near-ambient temperature and pressure [18, 56]. This provides unique opportunities for biomedical applications [19, 20, 109, 110], e.g., wound healing [111, 112], bacteria inactivation [113], sterilization [114], plasma-induced DNA damaging [115], and cancer cell treatment [116–120]. It is found that the quantification of number density of the main reactive species is the key for fundamental investigations of underlying mechanisms [60, 72, 121] as well as the development of future technologies [57, 75, 122, 123].

In this chapter, we investigate absolute O_3 densities in the plasma core of a homogenous He-O_2 capacitively coupled radio frequency (13.56 MHz)-driven plasma using the developed two-beam UV-LED absorption setup in chapter 3. Input plasma parameters such as plasma power and O_2 admixture are the main factors to control delivered O_3 density. Theoretically, plasma power relates to the energy coupled into electrons and the electron energy distribution function. This contributes to primary reactions such as electron impact excitation and ionization. These reactions are directly proportional to the number density of O_2 admixture and, consequently, influence the heavy-particle reactions and O_3 formations. Therefore, it is worth investigating O_3 density with the RF plasma power and $\%O_2$ admixture in order to understand the fundamental relation with the controlling plasma parameters.

Furthermore, the production and destruction of ozone are strongly gas temperature dependent [124]. Accurate measurements of the gas temperature are therefore crucial to the interpretation of the chemical kinetics involving ozone. We determine gas temperatures using measurements of the rotational temperature of the N_2 optical emission spectrum. The details of this diagnostic technique as well as alternative techniques are described in the literature to a great extent [70, 125]. An analytical description for the chemical kinetics based

on a full plasma chemistry model [51, 126] is discussed to correlate the measured ozone densities and gas temperatures.

4.1 The APP source

The investigated radio frequency (RF) atmospheric-pressure plasma source is described in reference [34] and shown in figure 4.1. It produces a cold, homogeneous-glow-like α-mode plasma with a mean electron temperature of about 2 eV and electron densities of up to 10^{17} m^{-3} [57]. The source comprises a plane-parallel rectangular stainless-steel electrode configuration with a gap distance of 1 mm. Ultraviolet (UV) transparent MgF_2 windows enclose the discharge region along the sides, and define a plasma channel with an optical absorption path length of 11 mm along the width of the electrodes, perpendicular to the feed gas flow along the length (30 mm) of the electrodes. The feed gas flux is that of 10 slm of helium with an oxygen admixture of up to 1 vol%. The flow condition is laminar through the cross-section of the plasma channel and the gap between the electrode and window, the mean gas flow velocity is about 8 m/s, and the gas residence time is about 3.7 ms. One electrode is capacitively driven by a 13.56 MHz RF generator through an L-matching impedance network (Coaxial Power Systems, RFG 150-13 and MMN 150-13), while the other electrode is grounded.

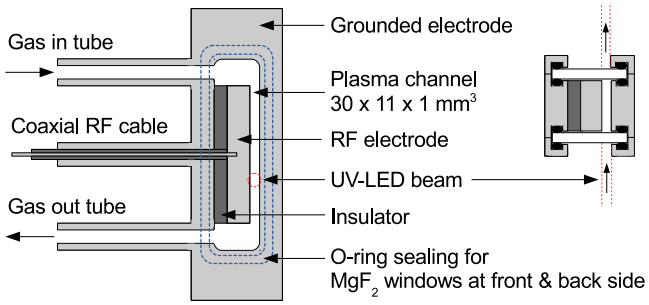

Fig. 4.1 Schematic of RF plasma source at side view (left) and cross-section top view (right). The original version of this figure has been published in [34], and the copyright permission was granted.

The investigated plasma source closely matches the key dimensions and properties of an existing well-characterized micro-plasma jet source [58, 80, 86, 127], apart from the up-scaled plasma channel width, here 11 mm instead of 1 mm, thus offering a longer absorption path and a lower ozone absorption detection limit; the corresponding surface-to-volume

ratios, and the guidance of the exhaust gas through tubes over about 50 cm in length into an air extraction, instead of directly into ambient air. For both plasma sources, the actual electrical power inputs into the core plasma are precisely measured by A. West [128]. The plasma power densities of both sources are the same as shown in figure 4.2. A comparison is possible, since our measurements cover the complete power range from the minimum limit for plasma sustainment to the upper limit just before transition into an unwanted constricted arcing mode, using those two limits as relative reference points.

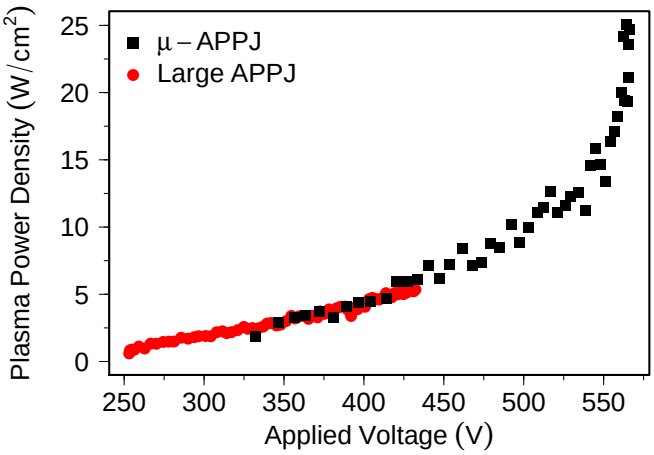

Fig. 4.2 Plasma power density of the standard μAPPJ and the large APPJ measured by A. West [128] at 13.56 MHz RF with He and 0.5% O_2 admixture.

4.2 O_3 density and gas temperature

In low-temperature atmospheric-pressure plasma with biomedical applications, one of the main factors is gas temperature which should be kept low and not thermally damage the thermally sensitive biological sample. The O_3 density was measured with RF power and $\%O_2$ variation. At the same time, the gas temperatures for each variation were also measured by the fitting emission spectrum of the N_2.

4.2.1 Gas temperature measurement

The same optical detection system - the spectrograph and camera in the experimental setup described in section 3.2 - is also used to record optical emission spectra of molecular nitrogen impurities from the center of the plasma channel. Those spectra are then analyzed to

deduce the gas temperature. Among the observed spectral features of the N_2 (C $^3\Pi_u^+ \rightarrow$ B $^3\Pi_g^+$) second positive system, see figure 4.3, we chose well-separated vibrational transition $\upsilon' = 0 \rightarrow \upsilon'' = 2$ with a band head position near $\lambda = 380$ nm. A simulated rotational band spectrum on the basis of a thermal population distribution among the rotational sub-levels of the upper N_2(C) state is numerically fitted to the measured spectra, as shown in figure 4.4.

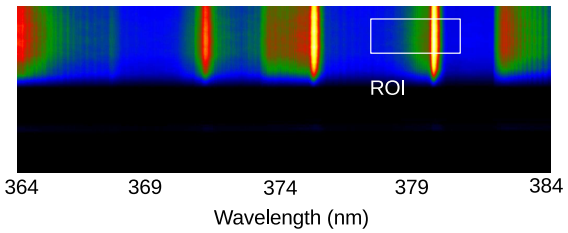

Fig. 4.3 CCD image of the optical emission from the N_2 second positive band system. The white rectangle illustrates the chosen region for investigating the $\upsilon = 0 \rightarrow 2$ vibrational transition.

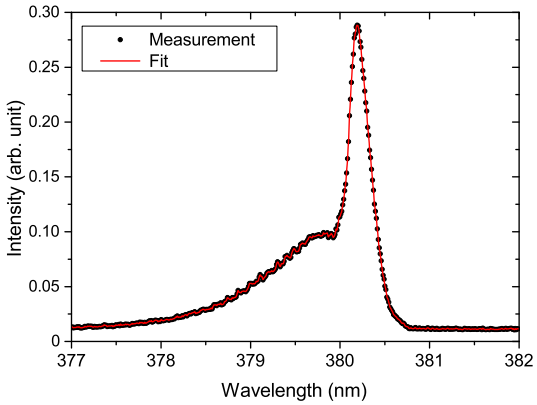

Fig. 4.4 Optical emission spectrum of the N_2 (C $^3\Pi_u^+ \rightarrow$ B $^3\Pi_g^+$) ($\upsilon = 0 \rightarrow 2$) rotational band. The solid curve represents a best fit to the measuring points; for details see text.

This spectroscopic method is well established (see, for example, [41] and references within), since the high collisionality under atmospheric pressure ensures a full rotation–translation equilibrium. The applied numerical spectra simulation and fitting procedure has successfully been cross-checked against other commonly used software, e.g., LIFBASE, and applied before [129]. In order to conduct the gas temperature measurements, a very small air gas leak in the feed gas tube of the plasma source had to be introduced (< 40 ppm according to minimum 2% control limit of 20 sccm N_2 MFC (MKS Type 1179A) in 10 slm He). Its influence was checked as not to influence the ozone density within the corresponding measurement accuracy and the optical emission lines of He and O as shown in figure 4.5. The detection system was operated at near-optimal performance in term of a spectral FWHM resolution of 0.25–0.31 nm at $\lambda = 380$ nm, with a longer camera exposure time of 30 s. The results for the gas temperature exhibit uncertainty from ± 10 to ± 19 K, varied within a parameter variation range of this experiment.

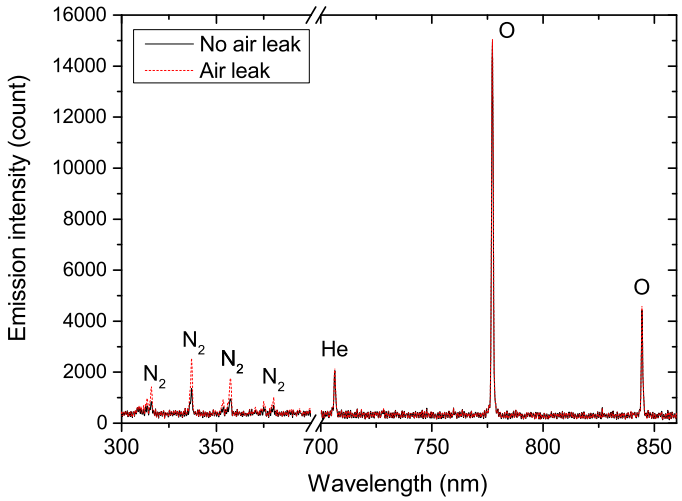

Fig. 4.5 Optical emission spectrum of N_2, He (706 nm), and O (777 and 844 nm) of He/0.5% O_2 plasma with and without air leak.

4.2.2 O_3 density with anti-correlation with gas temperature

The developed absorption setup for ozone density measurements provides a minimum fluctuation level for the unabsorbed baseline signal of about 4×10^{-4}, determined over 50 consecutive images in a steady state of the UV-LED in figure 3.8. This limit is mainly determined by changes in the absolute intensity of the UV-LED light source due to the stability of the corresponding current/power supply unit, rather than signal-to-noise limitations of the used CCD camera. An impact of possible spectral fluctuations can be excluded, since we evaluate the UV-LED intensity integrated over its spectral FWHM of about 11 nm, and it fits well within the broader and smooth ozone absorption cross-section profile. As described in section 3.4, the corresponding ozone density detection limit amounts to about 9.0 $\pm$ 0.9 $\times$ 10^{13} cm^{-3} on the basis of the absorption path length of 11 mm and the absorption cross-section data with maximum value 1.173 $\times$ 10^{-17} cm^2 at λ = 255.5 nm. The detection limit is equal to 3.66 $\pm$ 0.37 ppm, which is in the order of bio-technologically relevant concentrations. For example, the growth of E. coli bacteria was found to retard at ozone concentrations above 4 ppm [130].

The O_3 and gas temperature focuses on the discharge operation in homogeneous alpha-glow mode in the equilibrium range as described in section 3.5 at a constant He-flux of 10 slm. The RF generator power is varied in the full range from 6 W, required for sustainment, to 27 W, just below the arcing limit. All RF powers were read from forward RF on the RF

generator with 0 W reflect RF powers and without changing matching throughout the power variation range. The O_2 admixture is varied from 0.1% to 0.9%, which is motivated by reports of an atomic oxygen density maximum at around 0.5% O_2 [34] and, consequently, relevant for technological applications. All density results stated in the following are based on mean average and standard deviation statistics over 50 consecutively taken samples (see section 3.3 and 3.4). Note that some of the data points fall below the above-stated detection limit. Each ozone density measurement is accompanied by a spectroscopic measurement of the gas temperature.

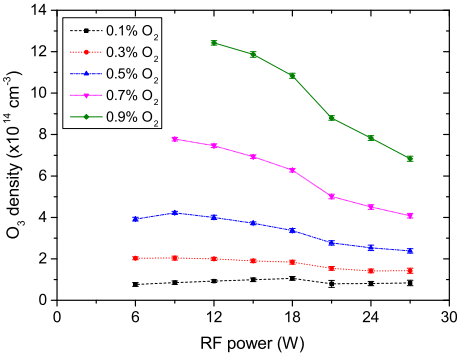

Fig. 4.6 Measured O_3 density as a function of the RF power for different O_2 admixtures. He-flux of 10 slm.

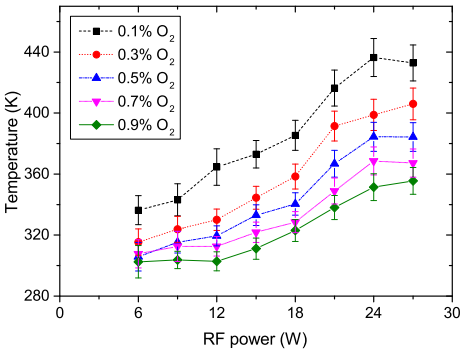

Fig. 4.7 Measured gas temperature as a function of the RF power for different O_2 admixtures. He-flux of 10 slm.

Figure 4.6 shows the measured ozone density as a function of the RF power for different O_2 admixtures. All of these dependencies exhibit a similar shape with a maximum at around 9 W. However, at large O_2 admixture and low RF power (e.g., 6 and 9 W for 0.9% O_2 admixture) the measurement could not be taken due to partly ignition inside the plasma channel. The ozone density decreases almost linearly from its value at the maximum down to about one half at 27 W RF power in 0.5, 0.7, and 0.9% O_2 admixture conditions. However, the decreases are slightly less at 0.3% and difficult to observe at 0.1% O_2 admixture. For fixed RF power, the dependence of the ozone density on the O_2 admixture is found throughout to be slightly over-linear, which can be seen, for example, in figure 4.10. The total ozone density increases of about one order of magnitude which is reasonable as the O_2 admixture increase over a factor of 9.

Figure 4.7 shows the correspondingly measured gas temperature as a function of the RF plasma power for different O_2 admixtures. Regardless of O_2 admixture, the temperature shows in most parts the expected linear increase with increasing RF plasma power. An exception is the behavior of low RF plasma powers and large O_2 admixtures, which seem to

be limited to room temperature (300 K). We conclude that the feed gas flow (mainly helium with the largest heat conductivity of all chemical elements) is capable of transporting the heat away from the plasma volume up to a certain RF plasma power limit. Above this limit, the solid stainless-steel electrodes presumably heat up to an elevated temperature with respect to room temperature [131] (see figure 4.8), while the mean gas temperature adjusts to an intermediate value, which remains approximately proportional to the RF plasma power.

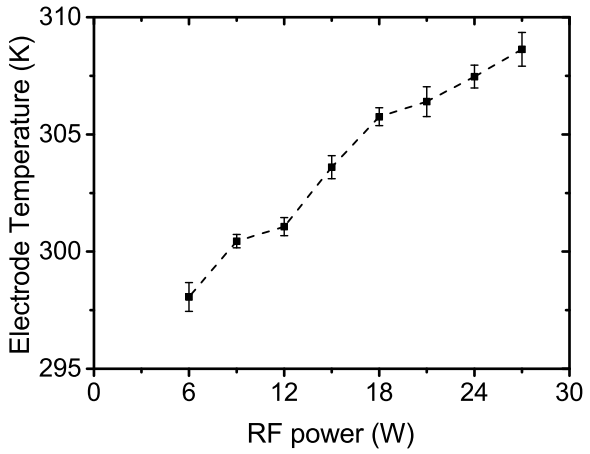

Fig. 4.8 Electrode temperatures as a function of RF power were averaged over all O_2 admixture conditions. The electrode temperatures were measured at a side of power electrode by infrared thermometer (Precision GOLD, N85FR)

Figures 4.9 and 4.10 show the direct comparison of the ozone density and gas temperature measurement results as a function of the RF power at fixed 0.5% O_2 admixture (figure 4.9) and as a function of the O_2 admixture at fixed 15W RF power (figure 4.10), respectively. In both cases, ozone density and gas temperature exhibit clearly opposite trends.

4.2.3 Spatial O_3 density and gas temperature

According to the spatial ozone density measurement in section 3.5, the spatial gas temperature along the plasma channel was also measured. The results are presented in figure 4.11. In the first half of the plasma channel, where the ozone density is in the build-up time before reaching the equilibrium level, the gas temperatures increases from 310 K at gas-input position to 331 K at the centre. This trend is similar to the ozone density. However, in the second half, where ozone density reaches the equilibrium level, there is a slightly drop of ozone density toward the nozzle that opposite to the lightly increase of gas temperature. This confirms the anti-correlation between ozone density and gas temperature when it is in

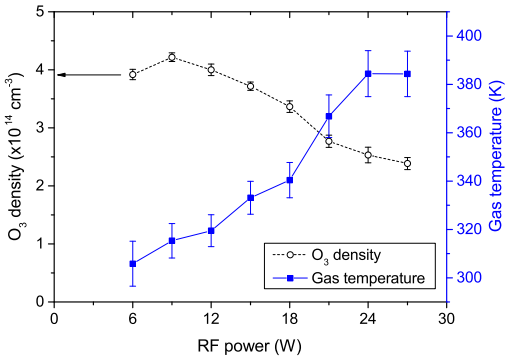

Fig. 4.9 Measured O_3 density (open circles) and gas temperature (filled squares) as a function of the RF power. He-flux of 10 slm, O_2 admixture of 0.5%.

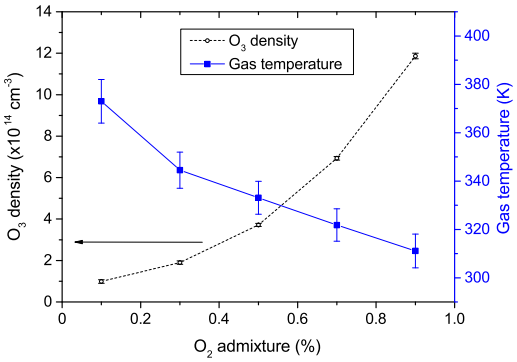

Fig. 4.10 Measured O_3 density (open circles) and gas temperature (filled squares) as a function of the O_2 admixture. He-flux of 10 slm, RF power at 15 W.

the equilibrium. In addition, the spatial gas temperatures provide important information for simulation model of ozone density along the plasma channel since the dominant reaction rates are gas temperature dependence.

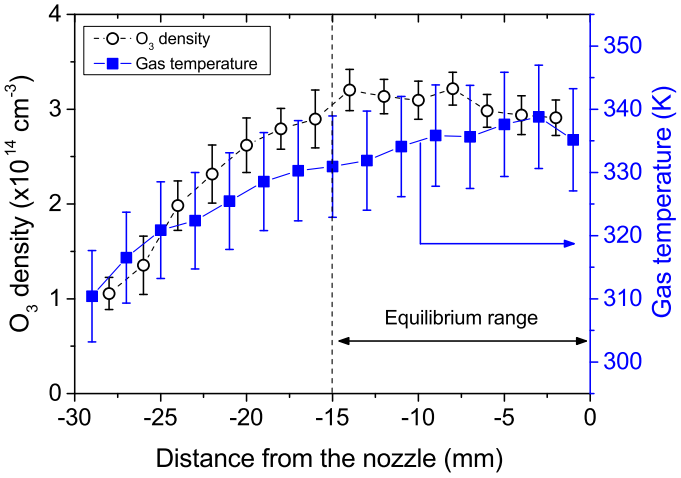

Fig. 4.11 Spatial resolved O_3 density with gas temperature along 30-mm long plasma channel. The plasma was sustained by 13.56 MHz RF, 15 W RF power, at 10 slm He with 0.5% O_2.

4.3 Model of gas temperature and O_3 density

In this section, the influence of the gas temperature on the ozone density as functions of RF-plasma power and $\%O_2$ admixture is investigated using a reduction version [126] of a full plasma chemistry model developed by M. Turner [51]. The reduced reaction set is appropriated to used as it is able to be identified the main pathway of the used plasma conditions [126]. The simulation results were performed by S. Schröter. The He-O_2 system included 11 species and 50 reactions. The pathway analysis has been investigated for the dominant productions and destructions of O_3, as expressed in table 4.1. The dominant producing reaction is three-body reaction R44, while the dominant quenching reactions are R42, R43, and R35.

Table 4.1 Dominant reactions and rate coefficients for O_3 in reduction version of the helium-oxygen plasma chemistry model [126].

No.	Reaction	Rate coefficient**
R44	$He + O + O_2 \rightarrow He + O_3$	$3.0 \times 10^{-46}\ (300/T_g)^{2.6}$
R42	$He + 2O \rightarrow He + O_2(a^1\Delta_u)$	$2.0 \times 10^{-45}\ (300/T_g)\exp(-170/T_g)$
R43	$He + 2O \rightarrow He + O_2(b^1\Sigma_u^+)$	$2.0 \times 10^{-45}\ (300/T_g)\exp(-170/T_g)$
R35	$O_2(b^1\Sigma_u^+) + O_3 \rightarrow O + 2O_2$	$2.4 \times 10^{-17}\ (300/T_g)^{0.5}\exp(-135/T_g)$
R49	$He + O^- + O_2^+ \rightarrow He + O + O_2$	$2.0 \times 10^{-37}\ (300/T_g)^{2.5}$
R12	$e + O_2 \rightarrow e + O_2(b^1\Sigma_u^+)$	$3.97 \times 10^{-16} T_e^{-0.089}\exp(-2.67/T_e)$
R13	$e + O_2 \rightarrow e + O_2(b^1\Sigma_u^+)$	$2.88 \times 10^{-14} T_e^{-0.84}\exp(-7.07/T_e)$
R6	$e + O_2 \rightarrow e + O + O(^1D)$	$3.12 \times 10^{-14} T_e^{0.017}\exp(-8.05/T_e)$
R28	$O + O_2(b^1\Sigma_u^+) \rightarrow O + O_2(a^1\Delta_u)$	8.0×10^{-20}
R45	$He + O + O_2(a^1\Delta_u) \rightarrow He + O_2 + O$	4.0×10^{-45}

**Rate coefficient in MKS unit with T_g in K and T_e in eV.

The general trend of the experimentally observed increasing ozone densities with larger oxygen admixtures can be qualitatively understood by the more efficient production of ozone through the three-body collision reaction. More quantitative predictions are however difficult for varying oxygen admixtures due to multiple plasma parameters changing simultaneously, in particular the mean electron energy and the electron density associated with a change in the gas temperature. The change in ozone density with varying input power is easier to analyse since the mean electron energy is almost independent of the input power for a given oxygen admixture [57]. This can easily be understood in the frame of a simple global particle balance [49].

The electron density increases with increasing input power, as described in [57]. On the one hand this leads to an increase of electron-impact reactions in the main production processes of O and O(^1D) through R6, and consequently in more ozone production through R44. On the other, hand the higher number densities of these species also decrease the O_3 densities preliminary through electron-impact excitation R12 and R13 and consequently through dissociation reaction R35 and recombinations R42 and R43. Additionally, these electron-impact excitation reactions (R6, R12, and R13) reportedly have a less than 10% contribution in either the production or the destruction of the ozone, and thus the ozone density would stay relatively constant overall as a function of power, neglecting gas temperature effects. This implies the stronger gas temperature dependent of O_3 density which could be confirmed by the discussion on the rate coefficient of the main O_3 production reactions in the next paragraph.

The gas temperature, however, also increases with increased power input and plays a key role in the chemical kinetics of the ozone. In the following we will exemplarily discuss the case of a power variation for a 0.5% O_2 admixture in He using the full plasma chemistry model [51]. According to the anti-correlation presented in figure 4.9, the experimentally determined gas temperatures were put into the gas temperature-dependent rate coefficients, while the rate coefficients with electron temperature dependence are varied based on the measured plasma powers.

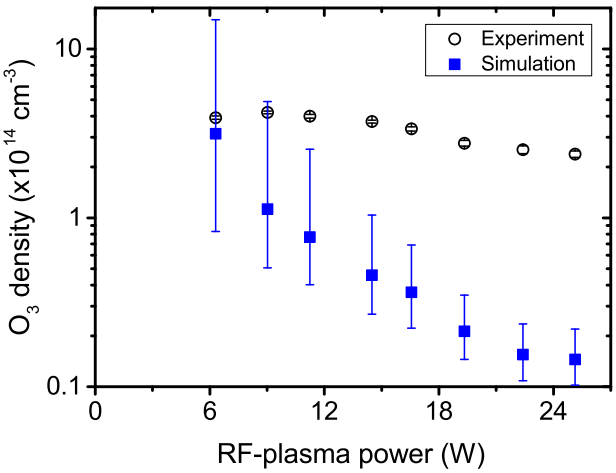

Fig. 4.12 Measured and modelled O_3 densities as a function of RF-plasma power at 0.5% O_2 admixture in He. The simulation has been done by S. Schröter.

Based on this simulation, figure 4.12 shows an agreement for the decreasing trend of O_3 densities as a function of RF-plasma power, with a stronger power dependence of the O_3

density in the model than in the experiment. While the qualitative trend can be explained well by the considered gas temperature dependence, the absolute value of O_3 densities in the model is about the same order of magnitude at the lower powers and drops to one order magnitude lower at higher powers than the experimental results. Furthermore, the uncertainty limits ($\pm$ 30 K) of the measured gas temperature were taken into account. The simulation shows high gas-temperature sensitivity in low plasma power due to the gas-temperature-dependent rate coefficient of the main pathway production of $O_2(b^1\Sigma_u^+)$ (69%), which is the species in the dominant uncertainty reaction (>90%) in ozone density.

This extensive model with a comprehensive error analysis [51, 126] has revealed that $O_2(b^1\Sigma_u^+)$ plays an important role, introducing significant uncertainties. The upper and lower limits of O_3 densities were up to one order of magnitude different in an intermediate regime (0.3 - 0.6% O_2) due to the strong coupling between O_3 and $O_2(b^1\Sigma_u^+)$. Furthermore, since O_3 was produced by a long reaction chain, large uncertainties can gradually build up from the uncertainty of the rate coefficient and the density variations of O, $O_2(a^1\Delta_g)$ and many minor excited species. This is one important issue for future studies, though it is outside the scope of the present work.

Chapter 5

O_3 density in pulse-modulated RF atmospheric pressure plasmas

One of the main characteristics of atmospheric pressure plasma is to control delivered reactive species. Excitation frequency is found to be the fundamental parameter to work with, since electrons strongly depends on it. Most of the dominating reactions are functions of electron energy distribution function (EEDF) and density. The influence of dual frequency technique was investigated in tailoring the EEDF in non-equilibrium RF radio frequency atmospheric pressure plasma [56, 57]. In RF plasmas, this has relatively high plasma intensity and low excitation voltage when compared to DBD kHz plasmas. However, RF plasmas consume higher power and generate higher gas temperature.

The pulsed-modulated RF excitation potentially influence power consumption and gas temperature [132, 133]. It allows a finite number of RF-cycle to generate plasma and repeat at a frequency in kHz range. Three different modes under modulation RF plasma were observed [134] and their mechanisms depended on the means of the residual electrons left between two consecutive discharges. Based on these studies, the pulse-modulated RF plasmas significantly reduced power consumption and gas temperature with the decrease in the duty cycle. Even though there was an example study of the pulse-modulated DBD RF atmospheric pressure plasma in sterilization [135], it is still unclear how this pulse-modulation mechanisms influence the main reactive species in different plasma conditions.

The main challenge of this chapter is to investigate the effect of kHz-pulsed-modulated driven frequency on O_3 densities in RF (13.56 MHz) atmospheric pressure plasma. The UV-LED setup was additionally set to study O_3 density with the modulation of the excited frequency. The duty cycle variations with the spatial measurement in the plasma channel provided an understanding of the time derivation of O_3 density. This further showed an

effective method in controlling reactive species. For the characteristics of the sustaining mode, the excitation frequency was 13.56 MHz radio frequency, modulated by the kHz frequency ranging from 1 - 50 kHz.

5.1 Experimental setup

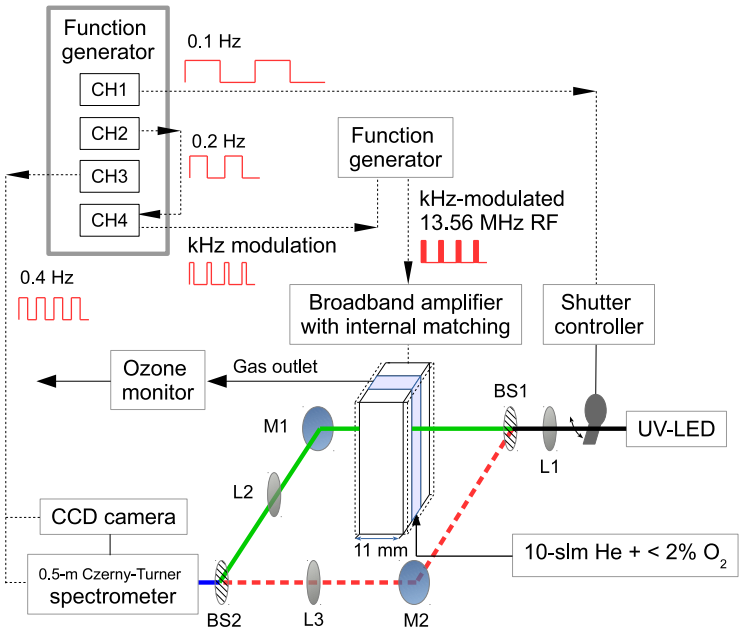

Fig. 5.1 Schematic of the two-beam UV-LED setup with frequency modulation setup.

As illustrated in figure 5.1, a 4-channel function generator (TTi, TGA 12104, 100 mHz) was utilized to generate four controlling signals. The signals of channel 1 - 3 and their characteristic waveforms of the setup were synchronized to define I_{PL}, I_L, I_P and I_{BG} as shown in figure 5.2 (a). The first three signals at 0.1, 0.2 and 0.4 Hz were used to control the UV-LED-blocking chopper, plasma source ON-OFF and CCD camera, respectively. The CCD camera was triggered by the rising edge of the 0.4 Hz signal, and the exposure time at 1.2 s was defined independently by the Andor Solis program [136]. Here, as the plasma needed to be frequency and duty cycle modulation, the fourth signal was used to provide different duty cycle and frequency modulation signals triggered by 0.2 Hz signal. The modulation signals were used as an external trigger of an arbitrary function generator which generated 13.56 MHz RF frequency, see figure 5.2 (b) and (c). The signal details was expressed in table 5.1.

For some technical points, since the squared wave form is not recommended for precise synchronization of the used function generator, the sinusoidal waves of three controlling signals were used in phase synchronization. These generated squared signals, with precise phase shift in each transistor-transistor logic (TTL) output channel. However, the chopper controlling box needed +5 V as a trigger, but the TTL maximum voltage was 4.6 V. So, the TTL output of channel 1 was changed to sinusoidal waveform with 10-Vpp with +2.5 V offset in the main output channel as mentioned in table 5.1.

Table 5.1 Description of channel connection of devices used in O_3 density measurement in kHz-frequency and duty-cycle modulated APP.

Device	**Channel**	**Characteristic**	**Description**
4-CH function generator	1 (Main)	Sinusoidal, 0.1 Hz 10 Vpp, 2.5 V offset	Master channel, for chopper
	2 (TTL)	Square, 0.2 Hz	Slave channel, for plasma
	3 (TTL)	Square, 0.4 Hz	Slave channel, for camera
	4 (Main)	Square,1 - 50 kHz, 10 - 90% duty cycle	- Be triggered by CH-2 - To modulated 13.56 MHz
2-CH function generator	Trigger	Square	- Be modulated by CH-4 of 4-CH function generator
	Output 1/2	Sinusoidal, 13.56 MHz, 632 mVpp	- Be amplified by broadband amplifier
Broadband amplifier	RF Input		- As an output of 2-CH function generator
	RF Output	Sinusoidal, 13.56 MHz, $\sim$ 550 - 600 Vpp	- With internal matching and applied to RF source

The excitation frequency of the plasma source, sinusoidal 13.56 MHz radio frequency with 632 mVpp was generated by an arbitrary function generator (100 MHz, WSB102, Tabor Electronic). The signal was amplified to about 600 Vpp and tuned by an internal matching unit of the broadband amplifier (10 kHz - 220 MHz, 100 W, SCCX100, IFI) to sustain the plasma. Finally, the operated plasma source was aligned with the two-beam UV-LED absorption setup as explained in 3.2.

5.1.1 Data acquisition and analysis

The O_3 density was investigated in He plasma gas with 0.1% artificial air N_2:O_2 (4:1) admixture . Data acquisition was taken using Andor program as a controlling unit with external

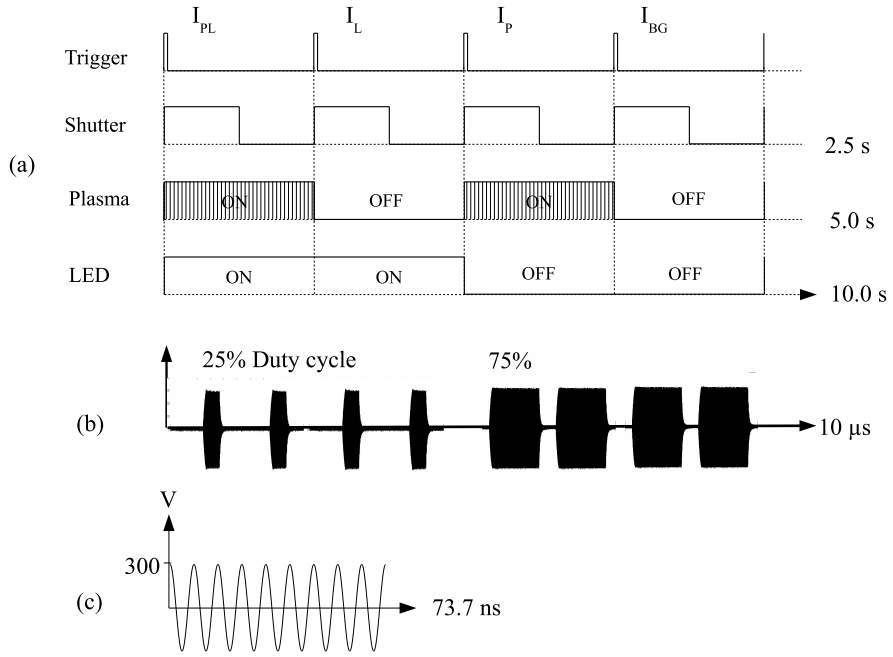

Fig. 5.2 (a) Synchronisation of three operational signals of camera, plasma source and UV-LED-blocking chopper at 0.4, 0.2 and 0.1 Hz, respectively, (b) 25% and 75% duty cycle at 100 kHz modulation frequency as triggered by 0.2 Hz signal and (c) sinusoidal 13.56 MHz radio frequency with 300 V amplitude as modulated by signals in (b).

triggering signals from function generator. The beams were resolved by Spectrometer and detected by CCD camera where all details are described in section 3.3. It provided images of four measured quantities, as shown in figure 5.3. With this $\%N_2$ admixture, the strong emissions dominated the intensity of the UV-LED light and background in figure 5.3 (a) and (b), respectively. Parts of the absorption spectrum in figure 5.4 (a) and 5.4 (b) were also dominated, which cannot be used for O_3 density calculation. Therefore, the unaffected parts were defined as ROI 1-a (248 - 250.5 nm) and ROI 1-b (260 - 262 nm) for the density calculation.

The 50 consecutive images of each quantity (I_{PL}, I_L, I_P and I_{BG}) were taken, and the intensities in each ROI were averaged. The preliminary O_3 densities from two ROIs were insignificantly different. So, 2-nm wavelength width of the ROI can be used for calculation purpose.

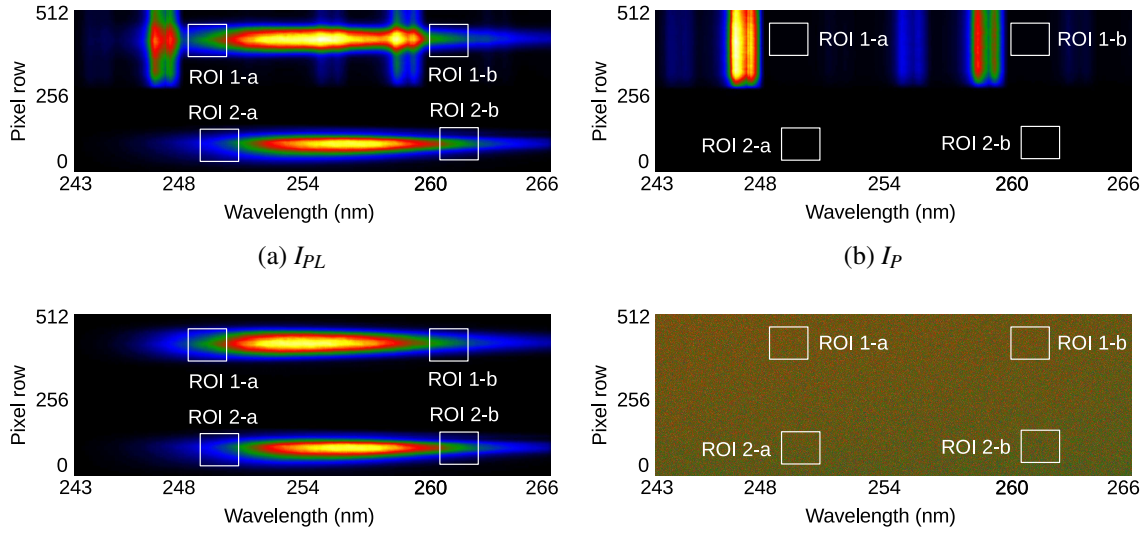

(a) I_{PL} (b) I_P

(c) I_L (d) I_{BG}

Fig. 5.3 CCD images of probe beam (pixel row 370-470 (ROI 1)) and reference beam (pixel row 40-140 (ROI 2)) intensities obtained with (a) LED and plasma, (b) He/N_2:O_2 (4:1) plasma only, (c) LED only, and (d) without LED and plasma.

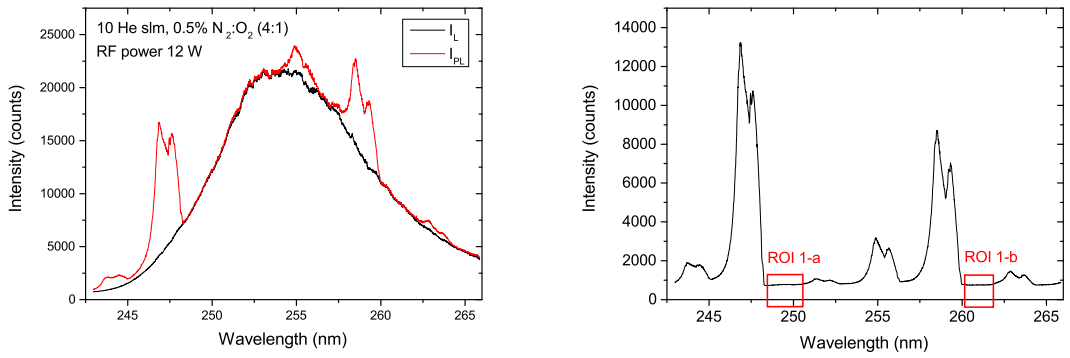

(a) I_{PL} and I_L (b) I_{BG}

Fig. 5.4 The spectrum of (a) UV-LED (I_L) is dominated by the emission spectrum of plasma (I_{PL}). Two unaffected ROIs are defined for the O_3 density calculation as ROI 1-a (248 - 250.5 nm) and 1-b (260 - 262 nm) in (b) plasma background, 10 slm He with 0.5% N_2:O_2 (4:1).

5.2 O_3 density with kHz-frequency modulation of 13.56 MHz RF APP

In this section, the O_3 measurements were taken using the similar structure of the plasma source introduced in the previous chapter, section 4.1, with the same 1 mm gap but different in an 8.6 mm absorption length and 27.5 mm plasma channel. The 8.6-mm absorption plasma source was previously measured for O and N density using VUV absorption technique in modulation frequency mode by J. Dedrick et al. However, O_3 density profile was also required. To have identical condition, this shorter absorption plasma source was therefore used throughout this chapter. In this experimental configuration, the beam position was located at about -6 mm from the nozzle regarding to the equilibrium rage in the continuous mode. The O_3 densities were measured with the variation of modulation frequency at 1, 2, 5, 10, 20, and 50 kHz. The 13.56 MHz radio frequency at 12 W on-phase RF power was used to sustain the 10 slm He plasma with 0.5% N_2:O_2 (4:1) admixture. The results are shown in figure 5.5.

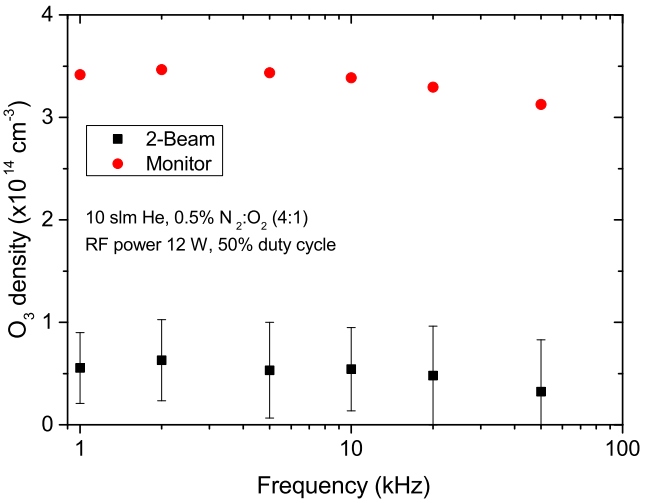

Fig. 5.5 Ozone densities as a function of frequency modulation at 50% duty cycle, with 2 slm He and 0.5% N_2:O_2(4:1) admixture.

In figure 5.5, the O_3 density does not strongly depend on the modulation frequency. The slight decrease of the average density with the modulation frequency falls within the error bar range. So, based on this two-beam UV-LED setup, the decreasing trend of O_3 can be observed, but it will be below the accuracy limit of the system. The more sensitive device, the O_3 monitor (2B Tech, model 205), was used to compare with the results of the two-beam

absorption measurement. As illustrated in figure 5.6 [137], the detector is more sensitive than the two-beam technique due to a longer absorption path. However, the monitor can be used to measure O_3 density in the effluent, only without spatial resolution.

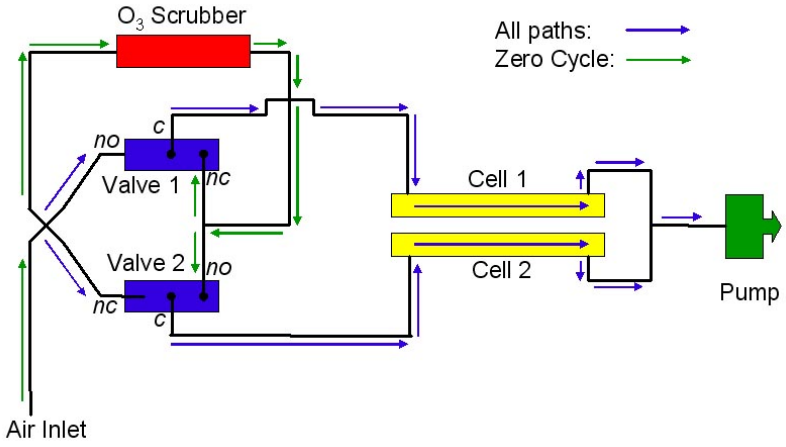

Fig. 5.6 Schematic diagram of O_3 monitor (2B Tech, model 205) shows the absorption Cell 1 and 2 which provide lower detection limit at 2.0 ppb for 10-s average [137].

As introduced above, the O_3 monitor requires the investigated gas flowing through the long absorption tube for determination, but it cannot be used for measurements inside the discharge channel. The monitor is used to measure O_3 density in the gas extraction tube at 20 cm away from the plasma active area as shown in figure 5.1 . The results from the monitor show a higher absolute value of O_3 density than in the plasma core. In addition, using the VUV absorption technique measured by J. Dedrick et al., the O densities as a function of modulation frequency are about 1.2×10^{14} cm^{-3} in the plasma core at 0.1% N_2:O_2 (4:1) and 10 slm He, as shown in figure 5.7. The O density can be approximately higher at 0.5% N_2:O_2. Theoretically, the O density strongly relates to the difference between the O_3 densities in the plasma core and in the effluent. Regarding the afterglow chemistry model [72], in the effluent region the O_3 production increases mainly through a three-body recombination of O, O_2 and He. On the other hand, this is the main loss mechanism of O. Furthermore, since the O was completely converted rapidly, two main loss pathways of O_3 density consequently disappear. The other reactions depend on the O_2, O_2^* density, which have a relatively constant reaction rate in the effluent. So, the absolute O_3 density in the effluent mainly increases due to the destruction of the O density. This explains the difference found by the two measurements.

For the frequency modulation dependence, the results show a slight drop of O_3 density when modulation frequencies are higher. The drop is particularly seen at 50 kHz. In prin-

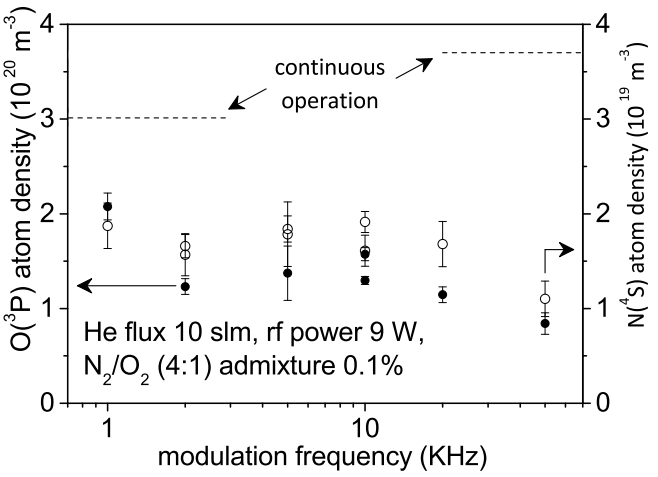

Fig. 5.7 O density as a function of frequency modulation ranging from 1 kH to 50 kHz was measured by the VUV absorption technique with 10 slm He and 0.1% N_2:O_2 (4:1). These results have been measured by J. Dedrick et al.

ciple, with the same 50% duty cycle of all frequencies, the plasma powers were equally coupled during the on-phase period. However, the on-phase time at 50 kHz and 50% duty cycle is 10 μs. According to the plasma excitation pulse characteristic in figure 5.8, the rising time of about 5 μs largely contributes to the on-phase time more than in the lower modulation frequency, which has a longer full-pulse time. The significant lack of full-pulse time leads to a decrease of the O density production period. Less O density consequently produces lower O_3 density in the off-phase period. On the other hand, in the lower modulation frequency regime, the rising time can be neglected due to the much longer full-pulse time. The O producing times are relatively in a longer equilibrium period, and then O_3 densities are about equally created. Based on this discussion, the lower kHz frequency is relatively more energy efficient for the RF plasma modulation than in a higher frequency regime.

5.3 O_3 density with duty cycle modulation of 13.56 MHz RF APP

At constant modulation frequency, duty cycle is one of the controlling plasma parameters, because it is able to confine the plasma operation time, and it consequently modulates the delivered important reactive species. In this section, the effect of duty cycle on O_3 density

was investigated in He with N_2:O_2 (4:1) RF atmospheric pressure plasmas. The modulation signals were frequency-constant at 10 kHz and duty cycle variations from 10% to 100%. The signals were generated by a 4-channel function generator and used as an external trigger of the 13.56 MHz RF function generator, where all detailed descriptions can be found in the previous experimental setup section.

The plasma pulse characteristics were measured by the HV probe (PMK 14KVAC) and recorded by the digital oscilloscope (LeCroy, Wavejet 354A, 500 MHz) as shown in figure 5.8. Based on this setup, it is found that the rising time of the pulse is about 4.8 μs with amplitude of about 600 Vpp. The 10 slm He with 0.5% N_2:O_2 gas was used with 12 W RF power for sustaining plasma. The examples of the pulsed modulation frequency with 25% and 75% duty cycle are shown in figure 5.9 (a) and (b), respectively.

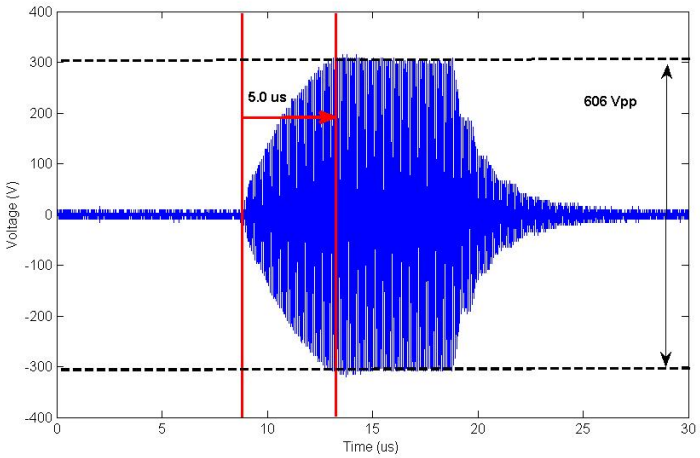

Fig. 5.8 Characteristic of the plasma excitation pulse at 10% duty cycle, 10 kHz modulation frequency, 12 W RF power. The characteristic rising time is about 5 μs.

The results are presented in figure 5.11. O_3 density increased with the % duty cycle. Based on the detailed description, the higher % duty cycle led to a higher power density (W/cm^3) and consequently, introduced higher gas temperature as shown in figure 5.10. In chapter 4, O_3 density shows the anti-correlation with gas temperature in He with O_2 admixture plasmas. The O_3 density is expected to decrease with the duty cycles.

However, in this case, 0.5% artificial air was added and investigated. The amount of N_2, four times higher than O_2 density, may play major roles in the discharge and introduce more complicated ozone production and destruction mechanisms [138]. As a result, the O_3 density increased with the duty cycle under this condition. The more specified reactions required very delicate and complex model description, beyond the scope of this work. The

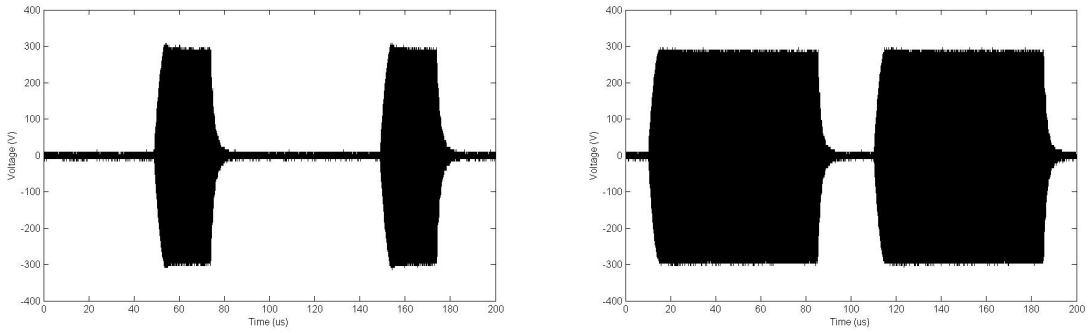

(a) (b)

Fig. 5.9 Modulation pulses at (a) 25% and (b) 75% duty cycle, 10 kHz frequency.

chemical modeling study of He with real air [139] was investigated in the high pressure glow discharge. Major reactions were transformed from oxygen-based species to nitrogen-based species. The significant contribution of O_3 density was not mentioned.

Furthermore, another chemical kinetics model in He-O_2 with humid-air impurities was studied, including 59 species and 1048 elementary reactions [59]. In the different regimes of the admixture concentration, the reactive oxygen species were found to be decreased with an increase in the humid-air fraction, due to the consumption through the production of nitrogen-based species, such as NO, NO_2, and N_2O. However, the O_3 density as a function of modulation controlling plasma parameter was not covered. Therefore, the delivered reactive species, as a function of modulation excitation frequency in He with a typical air admixture, are still in question for their mechanisms.

5.4 Spatial O_3 density with duty cycle

Regarding to the strong duty-cycle dependence of O_3 density in the previous section and the important of spatially resolved O_3 in section 3.5, the O_3 density due to these two factors in plasma channel was interesting to investigated. In this section, the spatial O_3 density profiles inside the 30-mm long plasma channel were investigated with different duty cycles. The RF plasma was sustained with 10 slm He with 0.5% O_2 admixture at 15 W RF power. The results are shown in figure 5.12, O_3 densities with 50% and 75% duty cycle of 10 MHz modulation frequency were compared to 100% duty cycle or continuous RF plasma.

At 100% duty cycle, O_3 density built up from 1.0×10^{14} cm^{-3} at the gas-inlet side (-30 mm from the gas-outlet nozzle) to reach the equilibrium level of about 3.0×10^{14} cm^{-3} from the center of the plasma channel to the nozzle (-15 mm to 0 mm). For 75% duty cycle,

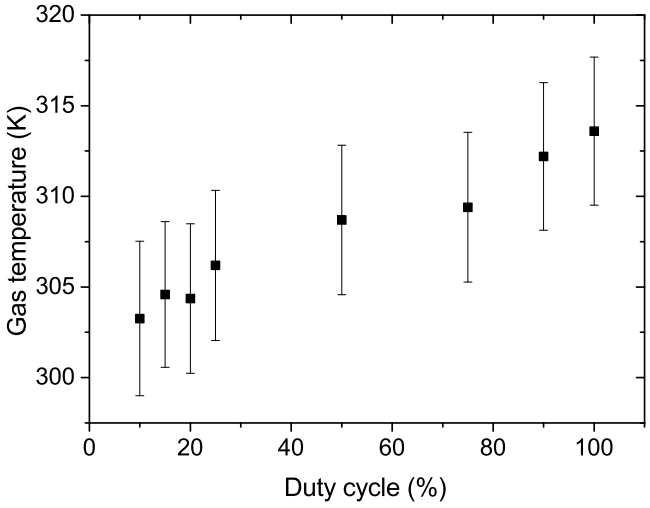

Fig. 5.10 Gas temperature as a function of duty cycle at 10 kHz modulation frequency, with 10 slm He and 0.5% N_2:O_2(4:1) admixture.

the O_3 densities showed a longer time to reach the equilibrium at about -7.5 mm. However, in 50% duty cycle case, the O_3 could not reach the equilibrium within the 30-mm plasma channel.

The temporal O_3 density calculated by the global model in He with 0.5% O_2 admixture RF atmospheric pressure plasma showed the build-up time to reach the equilibrium level at about 2 ms [59]. In the used plasma source, the mean gas flow velocity is about 8 m/s and the gas residence time is about 3.75 ms. So, it is possible to have an equilibrium start just after the center of the 30-mm plasma channel, especially in case of 100% as the build-up time is about 2 ms.

For lower % duty cycle, the plasma operational times were 0.075 and 0.050 ms, for 75% and 50% duty cycle of 10 kHz modulation frequency respectively. These yielded a longer plasma-off or after-glow time for the lower duty cycle. According to chemical kinetic model [72, 105], O_3 can be built up by the rapid quenching of O and O_2 species. So, lower % duty cycle with longer plasma-off time allowed more O and O_2 quenching reaction, and thus, produced more O_3 density. Moreover, since the density of quenching species are not able to reach its equilibrium level within the plasma-off time, the equilibrium range of O_3 density obviously cannot be observed in case of the 50% duty cycle. The results can be confirmed by an increase in the gas temperature or power density as a function of duty cycle [134] which anti-correlates to the O_3 density. Therefore, the delivered O_3 density in 13.56 MHz atmospheric pressure plasma can be significantly controlled by %duty cycle at

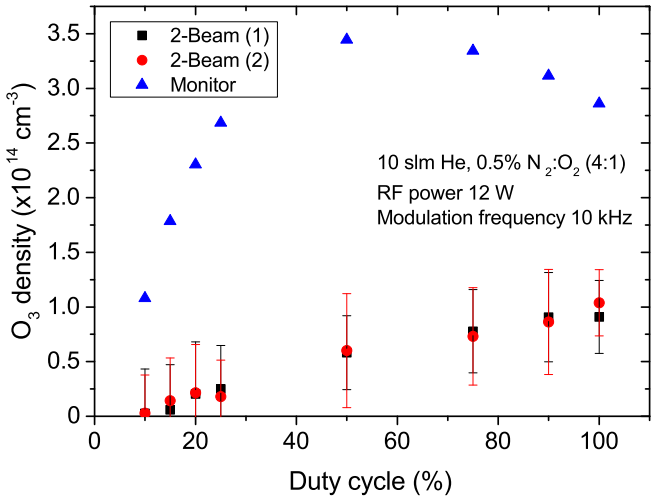

Fig. 5.11 Ozone densities as a function of duty cycle at 10 kHz modulation frequency, with 10 slm He and 0.5% N_2:O_2(4:1) admixture.

the modulation frequency in the kHz range.

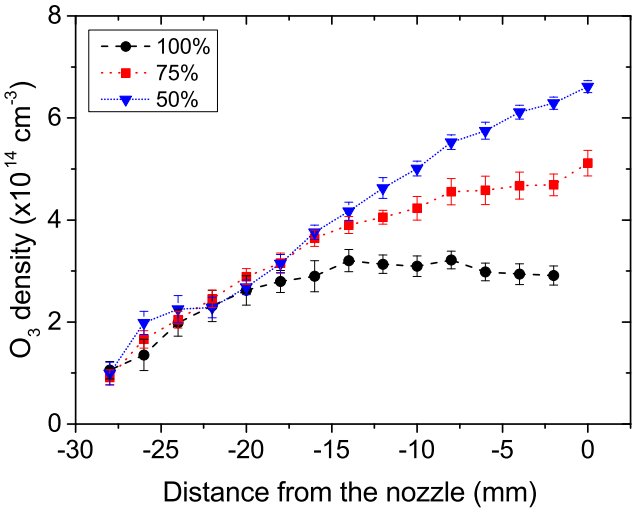

Fig. 5.12 Spatially resolved O_3 density inside the plasma channel with different duty cycles at modulation frequency 10 kHz, 10 slm He and 0.5% O_2.

Chapter 6

Spatial O_3 density in the effluent region of a co-axial DBD kHz-driven APPJ

In plasma applications with thermal sensitive living cells and organisms, it is very important to identify the role of dominant radicals to related effects on biological samples. The plasma production, charged species, vacuum ultraviolet (VUV) radiation, heat, and radical species have been investigated with respect to their interaction with treated surfaces. Plasma treatment in contact with a sample that is a combination of all plasma production is reported as the most effective condition in bacteria inactivation [26, 140]. Further investigation [141] showed that the contact and non-contact treatments of bacteria with a dielectric barrier discharged (DBD) kHz-driven atmospheric pressure plasma jet (APPJ) using He/N_2(3 %) created the same small areas of bacterial inactivation areas (or killing zones as commonly used in biology research field), which presented the minor role of the charged species. However, it clearly showed the larger killing areas of both treatments in the case of He/O_2(3%), which presented the crucial role in the inactivation process of reactive oxygen species (ROS), such as atomic oxygen (O), singlet delta oxygen ($O_2(a^1\Delta_g)$), hydroxyl (OH), hydrogen peroxide (H_2O_2), and ozone (O_3).

Regarding the role of VUV radiation, no inactivation was found in samples treated for 1 and 3 minutes, which showed the weak effect of VUV radiation [142]. Furthermore, the model and an experiment in the effluent have been studied to recognize the interaction and the absolute value of the main ROS [105]. The final main production was found to be a higher O_3 density with distance. In addition, the study by [140] assumed the possible crucial role of O_3 in the inactivation process since it has a relatively longer lifetime than other ROS, but a more precise diagnostic tool is needed to investigate the issue.

For well-known O_3 properties in sterilization, O_3 is the main species to destroy a variety

of bacteria, viruses, and spores by interfering with their respiratory system. The correlation of the population inactivated with the O_3 dose is one of the effective factors [143]. Moreover, DNA damage is induced by lipid peroxidation at the cell wall which is the result from stimulation by O_3 oxidation attacking the cell wall. In this case, the threshold concentration on bacterial inactivation by O_3 has been discussed [144].

Therefore, in this chapter, the UV-LED absorption technique with potential in spatially resolved measurement is used to investigate the O_3 density distribution in the effluent region of co-axial DBD kHz-driven APPJ applied to the biological samples. The jet was applied downward perpendicular to the sample surface at 30 mm from the jet nozzle. The surface was treated with the visible plasma plume ended at 25 mm, which allowed us exclude the contribution of high energetic electrons and probably charge species. So, there are no further charged species interactions but the chemical reactions between neutrals and low-energetic excitation species still remain in the invisible plasma regime.

The axis symmetry absorption profiles were measured in Cartesian coordinates and transformed by an Abel inversion [145, 146] into radial O_3 density distribution profiles. The O_3 density profiles are spatially investigated at 1 mm above the standard plastic Petri dish with the variation of the O_2 admixture. This enables us to get into the local O_3 density when the jet is applied to the sample surfaces. The same conditions have been applied to the bacteria growth on an agar plate. The correlations between the two aspects will be discussed for the role of O_3 in the inactivation process. Furthermore, the O_3 density profiles with distance variations within 30 mm between the nozzle and the sample are investigated. The results of the density distribution in two-dimensional spaces in the effluent region, including the effects of the air flow conditions, are discussed as well.

6.1 Absorption principle and Abel inversion

According to the experimental aspect as shown in figure 6.1 (left), the jet is downward applied to the circular plastic surface at 30 mm from the nozzle and the effluent is assumed to have a radial axis symmetry distribution. In figure 6.1 (bottom right), the UV-LED light of the diagnostic system is monitored at a fixed position directed along the y-axis throughout the radial distribution region of the effluent.

Four quantities (I_{PL}, I_P, I_L and I_{BG}) were measured and calculated for the line-of-sight absorbance at one x position ($A(x)$) by equation 6.1 along the line-of-sight (-y to y). The jet and surface samples were attached to the moving stage while the beam was in a fixed position. Spatial $A(x)$ was measured along the x direction with a 2.5-mm step as shown

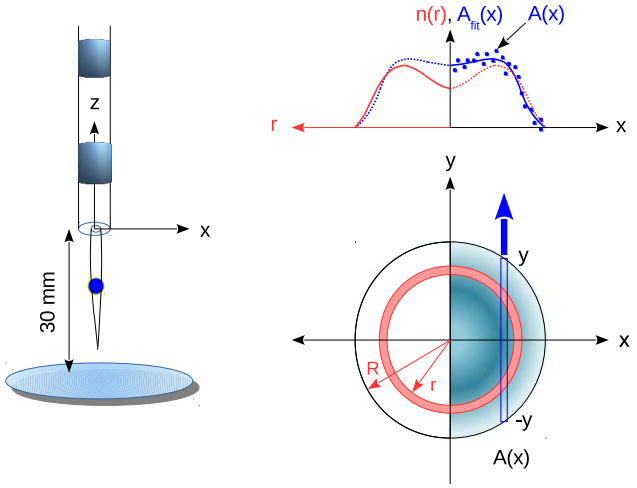

Fig. 6.1 Schematic of Abel inversion related to the experimental aspect; left: the jet is downward perpendicular applied to the surface; bottom right: top view of the absorption path of the UV-LED light; top right: experimental intensity profile (blue dots), fitting curve (blue line), and ozone density profiles (red line).

in figure 6.1 [top right, (blue solid dot)]. Then, the measured absorption profile was fitted by the fitting function [$A_{fit}(x)$, blue solid line], which is required in an inversion. The Cartesian-coordinate profile of $A_{fit}(x)$ were transformed by Abel inversion into the radial symmetry density profiles [$n(r)$, red solid line] in equation 6.2.

$$A(x) \approx A_{fit}(x) = -ln\left(\frac{I_{PL} - I_P}{I_L - I_{BG}}\right) = \int_{-y}^{y} \sigma(T,\lambda) n(r) dy \tag{6.1}$$

$$n(r) = -\frac{1}{\sigma(T,\lambda)\pi} \int_{r}^{R} \frac{\partial A_{fit}(x)}{\partial(x)} \frac{dx}{\sqrt{x^2 - r^2}} \tag{6.2}$$

where $\sigma(T,\lambda)$ is the ozone cross section assumed to be constant at 1.14×10^{-17} cm^2 (λ = 254.5 nm and T = 298 K) [107] and R is the plasma radius.

6.1.1 Abel inversion with different assumptions

The standard inversion technique above assumes the absorption to be 0 at R, but this is not actually true for any choice of R based on the measured data set. Therefore, the absorption definition is re-defined as shown in equation 6.3. These new basis function assumption and

method have been introduced by R. Vann.

$$A_{fit}(x) = \int_{-\infty}^{+\infty} \sigma(T,\lambda) n(r) dy \; = \; 2\sigma(T,\lambda) \int_{x}^{\infty} \frac{rn(r)}{\sqrt{r^2 - x^2}} \mathrm{d}r \tag{6.3}$$

To process on inversion, the radial density $n(r)$ is considered based on the following assumptions:

1. $n'(0) = 0$ since $A'(x)$ must be continuous at $x = 0$
2. $n(r)$ is differentially an arbitrary number of times everywhere
3. $\int_0^\infty rn(r)\mathrm{d}r < \infty$ (i.e. the area integral is finite)
4. $n(r) \to 0$ as $r \to \infty$
5. $n'(r) \to 0$ as $r \to \infty$

Then, $n(r)$ is proceeded as a linear combination of basis functions: $n(r) = \sum_i a_i n_i(r)$, where the $\{a_i\}$ are a set of coefficients (to be found) and we choose the $n_i(r)$ such that each of them satisfies conditions (1)-(5). A good choice of basis functions means that only a few of them is required in order to achieve a good fit to the data.

The basis functions $n_i(r) = r^{2i} e^{-(r/\sigma)^2}$ are chosen, where the parameter σ is the same for all i; i.e., $n(r) = e^{-r^2/\sigma^2} \sum_{i=0}^{\infty} a_i r^{2i}$. Please keep in mind that this σ is the FWHM of the density function, which is different from the ozone cross section $\sigma(T,\lambda)$. The basis function choice has the following properties:

1. Each $n_i(r)$ satisfies condition (1)-(4) above.
2. These $n_i(r)$ are a complete basis; i.e., any function that satisfies properties (1)-(5) can be written as a linear combination of these functions.
3. If we truncate the representation to $0 \leq i \leq M$, say, $n(r)$ can have a maximum of M turning points (excluding that at $r = 0$).
4. The form of this representation is invariant under Abel transform i.e.

$$2\int_x^\infty e^{-r^2/\sigma^2} \sum_{i=0}^{\infty} \frac{a_i r^{2i+1}}{\sqrt{r^2 - x^2}} \mathrm{d}r = e^{-x^2/\sigma^2} \sum_{j=0}^{\infty} b_j x^{2j} \tag{6.4}$$

for some new coefficients $\{b_j\}$, where $b_j = b_j(\{a_i\})$

Suppose a particular experimental data set is represented by $\{(x_k, A(x_k), \varepsilon_k) : -N \leq k \leq N\}$, where $\{x_k = k\Delta x\}$ are the coordinates at which measurements were taken (where Δx is the grid spacing), $\{A(x_k)\}$ are the corresponding absorption measurements, $\{\varepsilon_k\}$ are the standard deviations of the mean for each point and the number of points is $(2N+1)$. The initial fitting strategy is to pick a sensible value for M (we chose $M = 1$ throughout) and then minimize the fitting least squares cost function.

$$C(\sigma, a_0, a_1) = \frac{1}{2N+1} \sum_k \left(\frac{A(x_k) - A_{fit}(x_k)}{\varepsilon_k} \right)^2 \tag{6.5}$$

with respect to the parameters $\{\sigma, a_0, a_1\}$. This gives a best fit to the parameterized model with corresponding cost C_{bf}.

To obtain a quantitative measure of the reliability of this fit, two further optimizations are performed: we separately minimize and maximize $a_0 = n(0)$ under the constraint that $C \leq (1+\delta)C_{bf}$ for some (usually small) number δ. Since the measurements were made for both $x < 0$ and $x > 0$, the left-right asymmetry in the data is taken into account for a characteristic background noise level in the cost function:

$$C_0 = \frac{1}{2N+1} \sum_k \left(\frac{A(x_{+k}) - A(x_{-k})}{\varepsilon_k} \right)^2 \tag{6.6}$$

Then $\delta = C_{bf}/C_0 - 1$ is chosen. The validity of this inversion is compared with the simple discretization method and the sum-of-cosine method when the absorption length is finite as defined in equation 6.1 and the Abel inversion form of the density is expressed in equation 6.2. Equation 6.7 is based on direct discretization of equation 6.2 by which the algorithm is applied on $2N+1$ of the discrete fitting function $(A_{fit}(x))$ [145].

$$n(r_j) = -\frac{1}{\pi} \sum_{i=j}^{N-1} \frac{A_{fit}(x_{i+1}) - A_{fit}(x_i)}{\sqrt{\left(x_i + \frac{\Delta x}{2}\right)^2 - r_j^2}} \tag{6.7}$$

where $x_i = i\Delta x$ and $i = -N, ..., 0, ..., N$ are used to obtain $N+1$ points of $n(r)$ profile which $r_j = j\Delta r$ and $j = 0, ..., N$. Also, $\Delta r = \Delta x$, $r_0 = x_0 = 0$ and $r_N = x_N = R$. In this case, Δx and Δr denote a 1-mm spatial distance.

Equation 6.8, the summation-of-cosine method, is introduced by [146] and is available online in MATLAB code [147]. The distribution $n(r)$ is expanded similar to a Fourier series.

$$n(r) = -\sum_{n=M_l}^{M_u} A_n n_n(r) \tag{6.8}$$

where A_n is an unknown amplitude, $n_n(r)$ is a set of cosine-functions, and M_l and M_u are the lower and upper limits of the number of cosine functions, respectively.

$$n_0(r) = 1, \qquad n_n(r) = 1 - (-1)^n \cos(n\pi \frac{r}{R}) \tag{6.9}$$

Two independent fitting functions were performed as shown in figure 6.2. The fitting absorption is based on the basis-function format expressed by equation 6.10 determined by Mathematica [148]. Another absorption was fitted by MATLAB [149] and expressed by a Gaussian function of order three in equation 6.11.

$$A_{fit}(x) = \frac{Ae^{-x^2/q^2\sigma^2}\sqrt{\pi}(2a_1x^2 + (2a_0 + a_1)q^2\sigma^2)}{2q\sigma} \tag{6.10}$$

where A is the amplitude at $x = 0$ and q is the variation coefficient of σ.

$$A_{fit}(x) = a_1 \exp^{-(\frac{x-b_1}{c_1})^2} + a_2 \exp^{-(\frac{x-b_2}{c_2})^2} + a_3 \exp^{-(\frac{x-b_3}{c_3})^2} \tag{6.11}$$

where a_i, b_i and c_i are best-fit coefficients.

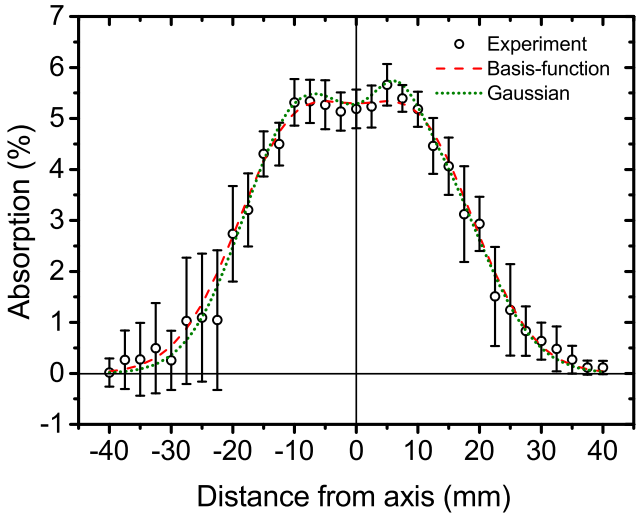

Fig. 6.2 Absorption with two fitting functions independently used for cross checking between different inversion algorithms.

The densities determined by three inversion methods are compared in figure 6.3. A cross check with a theoretical function was also required for algorithm verification. The theoretical function and inversion were taken from [150] as expressed by equation 6.12 and 6.13, respectively. The performance by discretization and sum-of-cosine algorithms was

compared to the theory as shown in figure 6.4.

$$A_{theory}(x) = \frac{16}{105}\sqrt{1-x^2}(19+34x^2-125x^4+72x^6) \tag{6.12}$$

$$n_{theory}(r) = (1+10r^2-23r^4+12r^6) \tag{6.13}$$

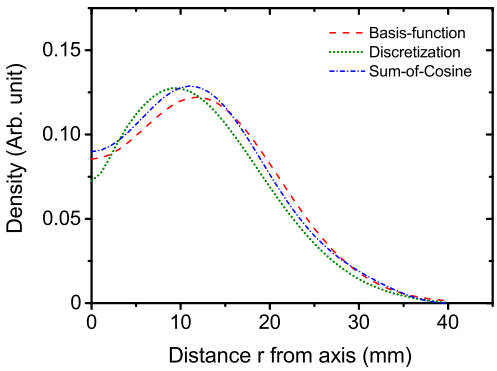

Fig. 6.3 The comparison of absolute ozone densities determined by basis-function, discretization and sum-of-cosine inversion methods.

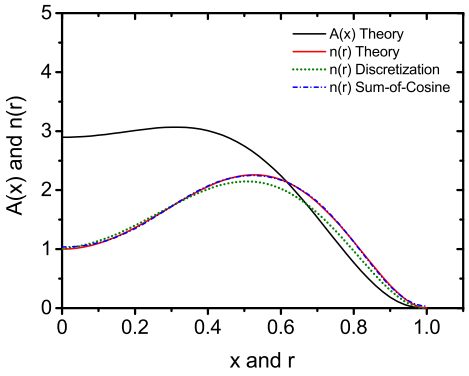

Fig. 6.4 The test function was transformed by sum-of-cosine and discretization algorithms and compared with the theoretical function.

6.2 Co-axial DBD kHzdriven APPJ and operational control system

The investigated kHz-APPJ comprises a cylindrical capillary quartz tube with an inner diameter of 1 mm and an outer diameter of 5 mm, as shown in figure 6.5. It is driven by two tubular copper electrodes, 10 mm wide, wrapped around the tube with a 20 mm gap. This structure is a dielectric barrier discharge type. At 10 mm from the nozzle, the downstream power electrode is driven by a sinusoidal excitation frequency at 30 kHz with high voltage at 12 kVpp. Another electrode is grounded. The gas flow inlet is 2 slm He or 2.55 slm/mm^2. To quantify the reasonable value of the measured O_3 density, the O_3 density of a co-axial kHz microsecond pulse APPJ [151] which has similar structure and operational condition was used in comparison. However, the airflow of the used jet is about 16 times higher than 0.16 slm/mm^2 in a comparative jet which operated at 6 kV and 20 kHz. The absolute O_3 density with the same $\%O_2$ admixture at the nozzle of the kHz APPJ in this work could be

more or less because of the obvious different gas flow rate but should be in the same order of magnitude.

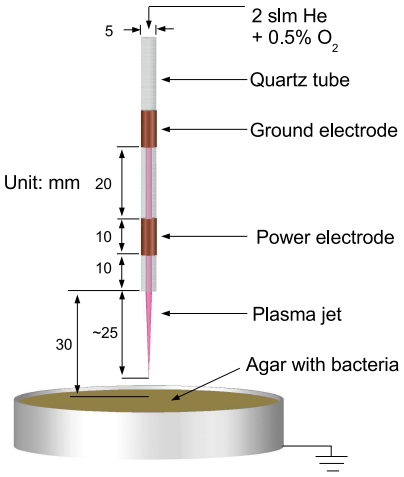

Fig. 6.5 Schematic of DBD kHz-driven APPJ applied to the surface sample.

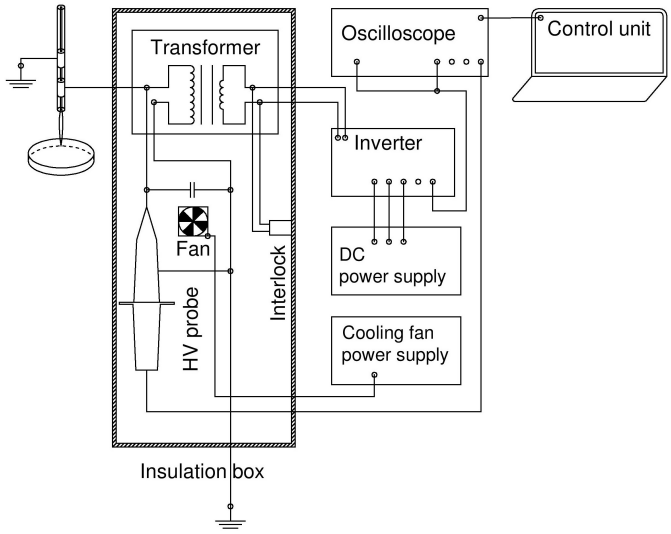

Fig. 6.6 Schematic of the control circuit of the system.

In figure 6.6, the direct current (dc) signals 20 Vpp at 800 mA were generated by a digital control DC power supply [TENMA, 72-10495 (0-30V 5AX2)] and converted into a sinusoidal signal by an in-house inverter with a modulation frequency at 30-kHz generated by a digital storage oscilloscope (Agilent Technologies, InfiniiVision, DSO-X 2004A). The 30-kHz frequency signal was then transformed to high voltage at 12 kVpp. The feedback of

the high-voltage signal was measured by a high-voltage probe (Tektronic, P6015A) which stability was controlled by an in-house controlling program.

6.3 Experimental setup

The UV-LED in the light source position in figure 6.7 was imaged by a 100-mm focusing lens (L1) and aligned through the effluent region of the plasma. It is defined as a probe beam (green solid path). Throughout the effluent region of about 100 mm in diameter, the beam size was about 2 mm in diameter at the edge and focused to 1 mm in diameter at the center. The beam divergence was relatively small compared to the absorption length of about 90 mm, so we assumed that the probe beam was parallel over the effluent region according to the Abel inversion assumption. Another beam, the reference beam (red path), was also split by a UV beam splitter (BS1; UVFS, 50/50, BBAR 250 - 450 nm, fused silica plate, BSW20, Thorlabs), to detect the beam stability. Both beams were then symmetry imaged to the slit position. To recognize two beams, the vertical position of the reference beam was shifted so that is was higher than the probe beam by adjusting the mounting angle of BS1 and MR2; details are explained in section 3.2.

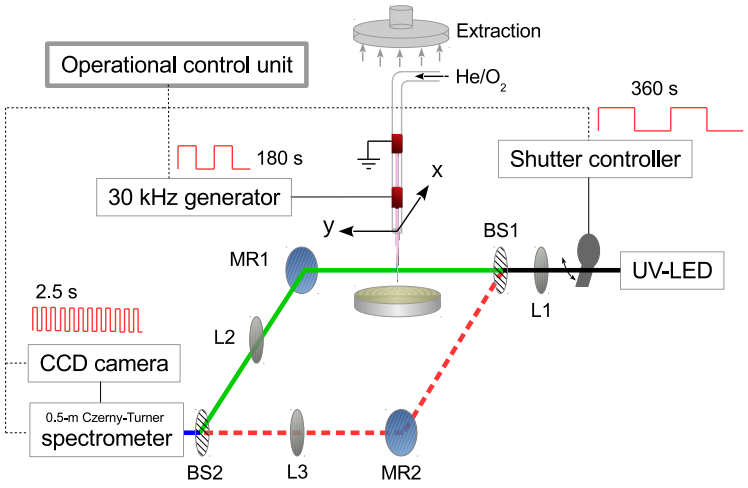

Fig. 6.7 Schematic of UV-LED absorption spectroscopy spatially measured ozone density in the effluent region of the coaxial DBD kHz-driven APPJ when applied to the surface sample.

In addition, the biological sample treatment time was taken into account the conditions of this experiment. The plasma treatment of 90 s was defined from the most effective bi-

ological test with the variation of time. The treated Bacteria, *Salmonella enterica* serovar Typhimurium, were cultured and prepared on agar plates by A. P. Maldonado, PhD student from Department of Biology, University of York.

6.3.1 Data acquisition and O_3 density calculations

According to 90 s of plasma treatment time on bacteria and four quantities required for the measured absorbance $A(x)$ in equation 6.1, the modulation frequencies were synchronized to operate the experiment, as shown in figure 6.8.

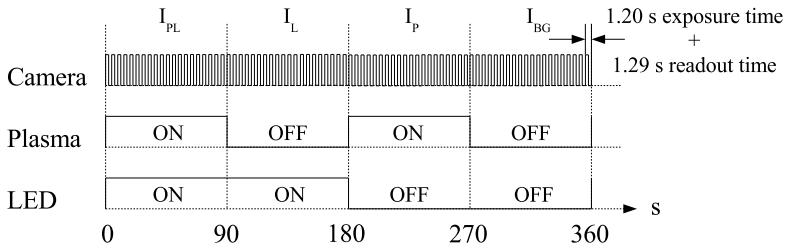

Fig. 6.8 Synchronization of modulation frequencies for four quantities used for ozone density calculation.

Based on the signal synchronization and the optimization of data acquisition conditions, which included a signal intensity at 80% of the saturation level of the CCD chip, a reasonable readout time, and low thermal/readout noise, each quantity was measured for 90 s using 36 images. One image period included 1.20 s of exposure time and 1.29 s of readout time. Four CCD images 512 $\times$ 2048 pixels in size were in spatial resolution (14-mm slit height) and wavelength resolution (242.96 - 265.86 nm), respectively, as shown in figure 3.6. The jet and the sample surface attached to the motorized moving stages (Zaber Technology, T-XY-LSM100A) were moved for each $A(x)$ points with a 2.5-mm step.

The full-width half-max (FWHM), as shown in figure 3.2 was determined from the fitting function of the beam spectrum and defined as a region of interest (ROI). Since O_3 cross sections vary for each half nanometer over 11-nm FWHM [107], we separated the ROI into a half nanometer width corresponding to each cross section. The $A(x)$ of each image can be determined from the sub-half-nanometer ROI and was averaged over the 11-nm of the ROI. Last, the final mean $A(x)$ was averaged from 36 images. The fitting function of spatial $A_{fit}(x)$ profiles were numerically calculated for the radial O_3 density distribution by the basis-function method as described in section 6.1.

6.4 Surface O_3 density distribution with correlation to the bacteria killing zone

The absorbance $A(x)$ profiles (in percentage units) at 1 mm above the surface or 30 mm from the nozzle were measured in the effluent regions of 2 slm He gas with 0.2%, 0.5%, and 1.2% O_2 admixtures. The data were fitted by the basis function described in section 6.1 and are shown in figure 6.9. The large error bars of the absorption profiles between $\pm$ 15 - 30 mm away from the axis were influenced by turbulence. This typical turbulence is generated by the combination of the jet-downstream spreading outward on the surface, the side ambient air inflow and the centre-upward gas-extraction flow. These large variations were the main error on the O_3 density in this area. Then, the three absorbance fitting functions were inverted by Abel inversion into radial O_3 density distribution profiles. The inversion provides radial ozone densities with consideration of the minimize, maximize and best-fit conditions of the centre density as shown in figure. 6.10 (a), (b) and (c) for 0.2, 0.5, and 1.2% O_2 admixtures, respectively. The best fit will be used to correlate to the biological samples.

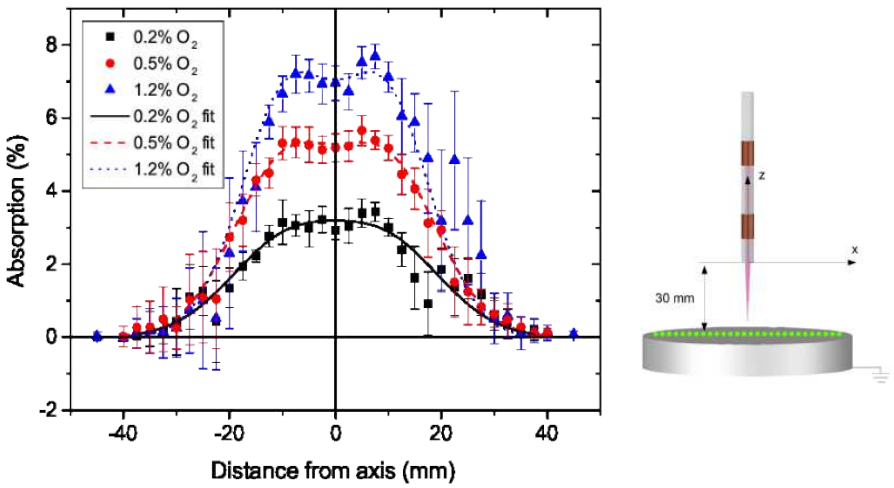

Fig. 6.9 Absorption profile with different %O_2 admixture in 2 slm He measured 1 mm above the agar surface. The distance between the surface and the nozzle is 30 mm.

Additionally, the absorption profiles over a plastic surface in this section are slightly higher than the value over the agar surface used in the plasma bacteria-inactivation experiment, as shown in figure 6.11. The lower ozone density on the biological surface potentially implies the existence of ozone reduction by a treated agar surface. The actual interactions between ozone density and biological results or with the contribution of other species are

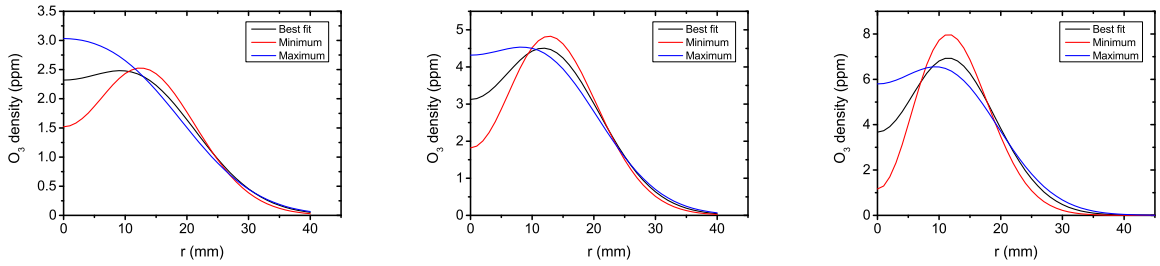

(a) 0.2% O_2 (b) 0.5% O_2 (c) 1.2% O_2

Fig. 6.10 Abel inverted density profile $n(r)$ as a function of the radius r for the different oxygen concentrations. At the centre density, the black curve is the best fit to the data. The red and blue curves minimum and maximum, respectively.

beyond the scope of the measurement. However, the correlation between the radial ozone density profiles and the bacterial inactivation result is possible.

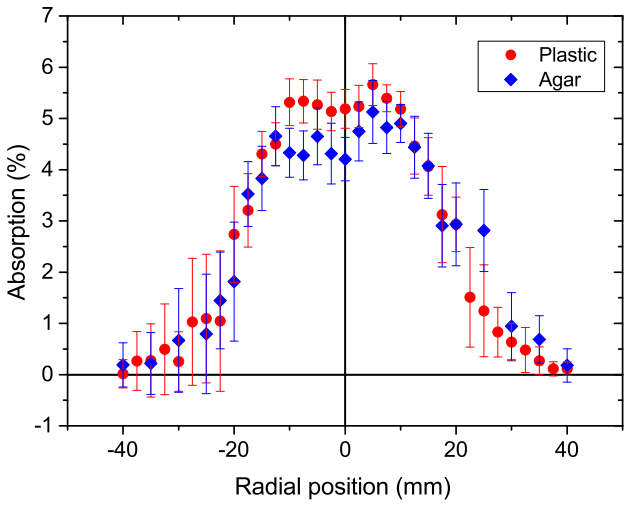

Fig. 6.11 Comparison of ozone absorption profiles measured on plastic and agar surfacees.

The cross section areas of the absolute value of the O_3 density profiles show the detailed correlations with the bacteria killing zone areas, as shown in figure 6.12. The effective gaseous O_3 concentrations that retard and inhibit the growth of E. Coli were found to be at 4 ppm and 10 ppm, respectively [130]. In figure 6.12 (a-right), at an 0.2% O_2 admixture, 8-mm killing area radius is related to about a 2.5 ppm O_3 density in figure 6.12 (a-left), which is considered slightly less than the effective range. However, about 2.5 ppm level, it also corresponded to distances 8 mm to 12 mm from the axis of the O_3 density distribution;

see also in figure 6.10 (a).

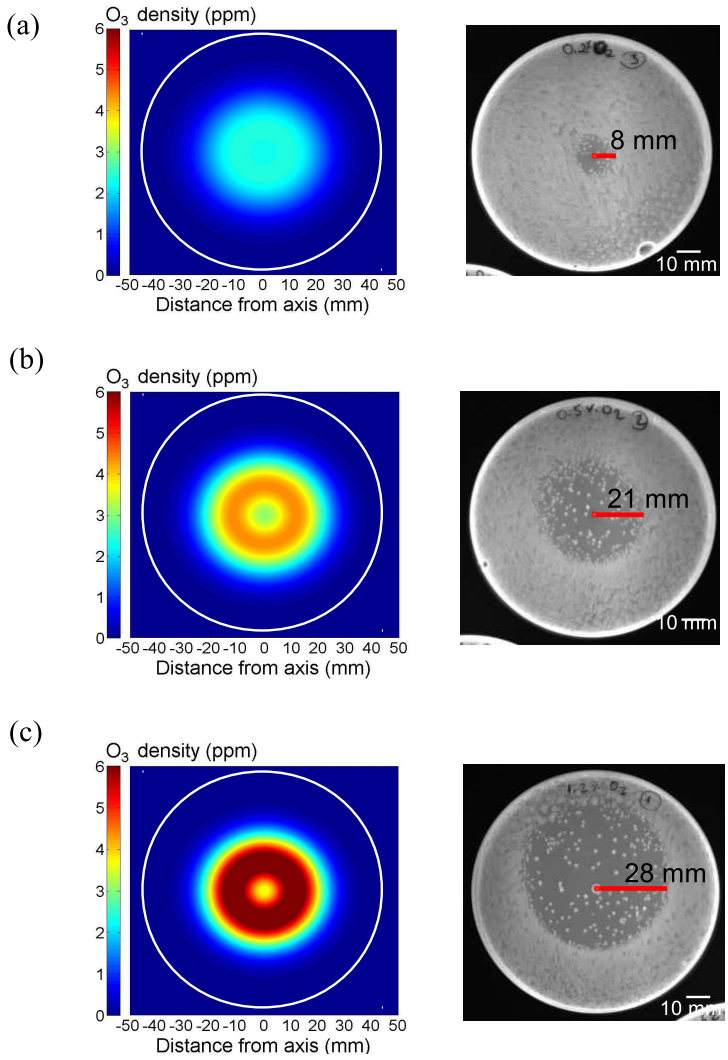

Fig. 6.12 Correlation between the absolute O_3 densities with the killing zones of bacteria: (a) 0.2% (b) 0.5% and (c) 1.2% O_2 with 2 slm He of co-axial DBD kHz-driven APPJ. The radial ozone densities were measured at 1 mm above the surface placed 30 mm below the jet nozzle. The biological results have been done by A. P. Maldonado.

In the case of the 0.5% O_2 admixture, as shown in figure 6.12 (b) and 6.10 (b), the concentration level at 2.5 ppm is related to the radius of the O_3 density distribution at 21 mm. The areas agreed well with the killing zone. However, the O_3 radius of 25 mm with 1.2% O_2 admixture, as shown in figure 6.12 (c), was less than the bacteria killing radius of 28 mm. The effective density cross section area can be relatively underestimated in turbulence region because the fitting function of the absorption profile takes into account

only the numerical average value of the measurement. However, the bacterial inactivation area was physically treated by either a higher-density or larger-density profile, as clearly indicated by the large error bar in the turbulence region (figure 6.9).

Though the increasing size of the bacteria killing zones with $\%O_2$ admixtures was found to be related to the increasing the radius of O_3 density profiles at one typical effective concentration level, it is not precisely correlated. The inversion technique uses the fitting function which equivalent to the average value profile of the absorption for the density calculation. This technically excludes the high error bar in the density cross-section area. Additionally, the treated surface is relatively more sensitive and could be effected by the spatial and quantitative fluctuation of the ozone density as indicated by large error bar. For the effect of thermal stability of the plasma source, since the driving power of plasma source was checked by the feedback signals during the operation, it was controlled to operate relatively more stable. This might not be a significant factor of the fluctuation in the turbulence region. With these discussions, O_3 may be one of the main reactive species for bacteria inactivation; a more precise measurement technique is required to identify its roles. The contribution along with other main reactive species should be considered; for example, singlet delta oxygen can also be found in the effluent and can reach the surface sample [36], which requires further investigation.

In the case of charged species, the sample surface was 30 mm away from the nozzle and the jet downstream can be observed by the naked eye up to 25 mm. This shows the quenching of the charged species and confirms that only the reactive neutral species reach the surface. Furthermore, the main chemical mechanisms of O_3 and the effect of the ambient air are equally important, which must be discussed with respect to two-dimensional spatially resolved O_3 density in the next section.

6.5 Spatially resolved O_3 density in the effluent region applied above the surface

The absorption profiles with distances of 1, 10, 20 and 30 mm from the nozzle, as shown in figure 6.13 were transformed into radial O_3 density profiles. Then, the radial density profiles were interpolated and plotted in two dimensions, as shown in figure 6.14. On the propagation axis, at 1 mm from the nozzle, about 1 ppm of O_3 density increased to about 3 ppm at 30 mm or 1 mm above the surface and up to 4.5 ppm at $\pm$10 mm off-axis. The increasing trend with distance agreed well with O_3 density in the effluent region of the

RF-driven He with a 0.6 $\%O_2$ micro atmospheric pressure plasma jet (μAPPJ) measured by molecular beam mass spectrometer (MBMS) [105]. Even though, two plasmas are different, they can only be used as a confirmation of the increase of O_3 density in the effluent. Note that, the ppm unit used in figure 6.14 was converted from molecules/cm^3 unit using ideal gas law equation which taking into account the temperature in the effluent region. The temperature were locally measured by thermocouple.

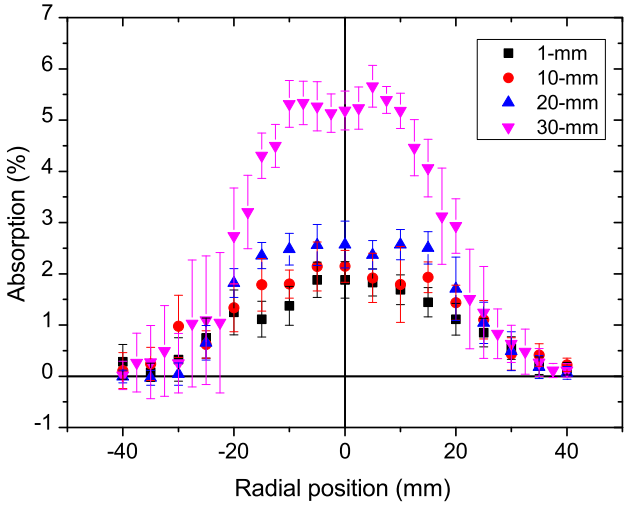

Fig. 6.13 Absorption profiles with different distances from the nozzle.

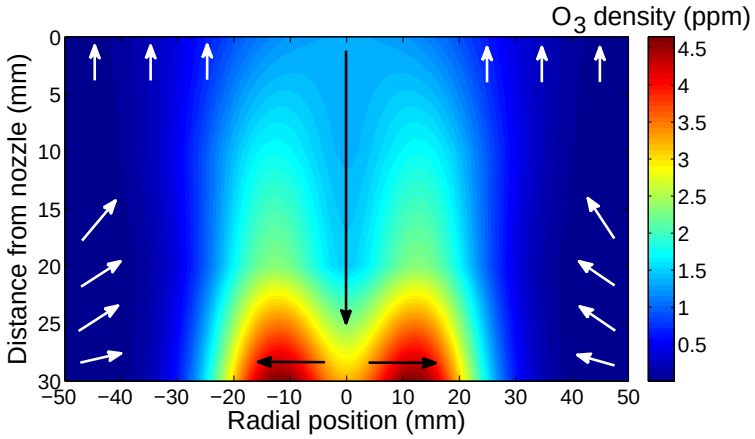

Fig. 6.14 The spatially resolved ozone density in the effluent region of the coaxial DBD kHz-driven APPJ with 2 slm He and 0.5% O_2 when applied downward 30 mm above the surface.

According to the fluid model of plasma effluent by Jeong et al. [37], the chemical kinet-

ics and transport of the main reactive oxygen species, O, O_3, $O_2(^1\Delta_g)$, and excited oxygen (O_2^*), are simulated by a diffusion-convection transport equation. The O_3 production by the O recombination with O_2 and background gas He and N_2 are the dominant chemistry processes, as shown in equations 6.14-6.17. N_2 admixtures from the ambient air start to mix in the effluent after 4 mm and rise up with the distance away from the nozzle [105]. In addition, interactions with ions and electron are negligible because of their very low densities in the effluent. Metastable helium (He^*) atoms are also immediately dropped because the end of electric excitation. OH, with a short lifetime in microseconds, can reach the surface but with very low density [140, 141] under this gas admixture condition.

$$O + O_2 + He \rightarrow O_3 + He \tag{6.14}$$

$$O + O_2 + O_2 \rightarrow O_3 + O_2 \tag{6.15}$$

$$O + O_2 + N_2 \rightarrow O_3 + N_2 \tag{6.16}$$

$$O_2^* + O_2 \rightarrow O_3 + O \tag{6.17}$$

In terms of boundary conditions, the jet stream is operated downward to the surface and the inflow of ambient air is symmetrically flowed from the sides. All particles are forced upward by the extraction. These three flow directions created a turbulence at distances between $\pm$15 and 30 mm from the axis. These can be observed by the large error bar within this range of the absorption profile in figure 6.9. The fitting functions on the absorption profiles technically excluded this large error as discussed in section 6.4. Finally, the shape of O_3 density can be narrower by this excluding. In addition, the long lifetime O_3 can stay in the upward flow to the extractor and mix with the absorption profile near the nozzle. As a result, the O_3 density profiles look relatively broad compared to the 1-mm of diameter of plasma plume close to the nozzle.

As shown in this chapter, the frequency modulation UV-LED absorption technique can spatially measure O_3 density in the effluent region of low-temperature kHz-driven APPJ applied perpendicularly downward to the surface sample. This provides information on the local O_3 density to identify its crucial role in biological applications.

At the selected 2.5 ppm effective level of O_3 concentration for bacteria inactivation, the radial O_3 density profiles with different $\%O_2$ admixtures showed the correlation with the

bacteria killing zone on the agar plates but not precisely. Based on the non-contact treatment aspect, the minor role of VUV on bacteria inactivation, the study of ROS in the effluent, and the correlation found in this work showed the possibility of O_3 as a key reactive species in bacteria inactivation. However, another ROS, singlet delta oxygen species, should also be investigated under this condition for any possible contributing role in bacteria inactivation.

Under the application aspect of this work, the O_3 density in the effluent region in two-dimensional space showed the increasing of the O_3 density by a factor of three. Furthermore, the contour plot showed the physical combination effects of the downstream plasma jet flow, the side ambient air inflow, and the centre-upward gas extraction. The turbulence caused by these flow combinations and the calculation technique significantly influence parts of the O_3 density distribution. In addition, because of the long lifetime of O_3 and the center position of the gas extraction, O_3 can stay until it leaves the upper boundary and travels parallel close to the nozzle. This can also broaden the O_3 density profiles near the nozzle area.

Chapter 7

OH and O_3 densities measurement in water-containing plasmas

With a general application prospective of atmospheric pressure plasmas, an ambient environment obviously contains water in both liquid and vapour forms [152]. An interaction of plasma with water produces reactive oxygen and hydrogen species such as hydrogen peroxide (H_2O_2), hydroxyl (OH), and hydroperoxyl (HO_2) [153]. OH which is one of the main production channels of H_2O_2, and has non-selective strong oxidizing properties, has gained much interest for its mechanisms. Atmospheric pressure plasmas with a water contribution environment have been used for many applications such as biomedical applications [154, 155], sterilizations [156, 157], and surface treatments [158].

Plasma chemistry and its dominant species and pathways are commonly studied by numerical models and experimental diagnostic techniques. In the simulation, a (zero-dimensional) global model has been used to study the low-temperature atmospheric pressure He + H_2O plasmas [50]. The model includes 46 species and 577 reactions. The Penning ionization was report as a key ionization mechanism of this discharge condition while the main reactive species are O, OH, and H_2O_2.

For the measurement, many diagnostic techniques have been used to measure OH density in low-temperature atmospheric pressure plasma. Laser induced fluorescence (LIF) spectroscopy [38, 39, 159] can be used to obtain density but this technique depends strongly on the quenching rates of the excited state which also vary under different discharge conditions. This contributes to the uncertainty of the densities. Moreover, the cavity ring-down technique was also applied to obtain OH density in the microwave atmospheric pressure plasma jet [160]. This technique is relatively less dependent on the assumption but it is more complicated to implement [161].

OH absorption cross sections in the UV range (center at 308 nm) are in the order of 10^{-16} cm^2 [162], which is one order of magnitude higher than the O_3 absorption cross section. So, a UV absorption spectroscopy is commonly used to investigate the OH density; for example, in the diffuse atmospheric pressure He-H_2O RF glow discharge [41, 42] and in Ar-H_2O dielectric barrier discharge [163]. Theoretically, the OH absorption spectrum are split into each narrow spectral line with less than 0.1 nm wavelength shift.

Hence, the main challenging of this chapter is modifying the developed UV-LED absorption setup to be able to measure OH density in this typical plasma condition. First, the time resolved OH density was measured for determining the steady condition of the plasma source. Then, OH density was investigated as a function of H_2O concentration in He and He/air/O_2 plasma with H_2O vapour. The results on the RF plasma show a good agreement with the broadband UV absorption technique developed by Laboratoire de Physique des Plasmas (LPP), Ecole Polytechnique, Paris.

7.1 OH density by UV absorption spectroscopy

The OH ($A^2\Sigma^+ \leftrightarrow X^2\Pi, v' = v'' = 0$) rotational band spectrum from transition $Q_1(1)$ (307.844 nm) to $P_1(2)$(308.639 nm) [162] as presented in figure 7.1 is used in absorption spectroscopy based on equation 2.26.

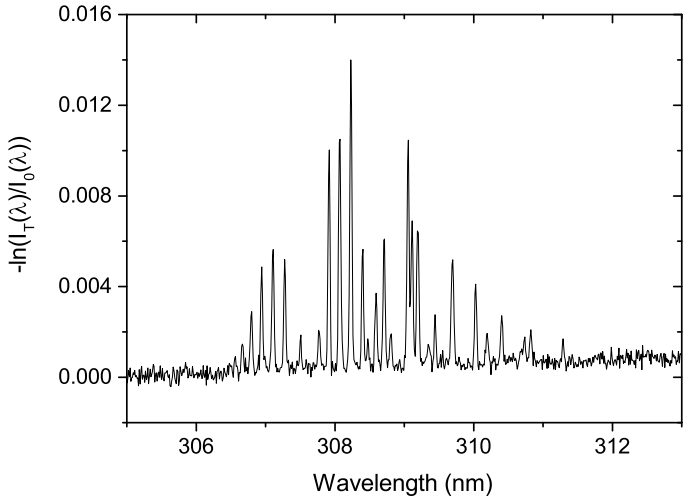

Fig. 7.1 OH absorption spectrum is expressed by the absorbance, $A(\lambda)$, defined from four measured parameters.

Experimentally, four measured parameters including the intensity of the LED with plasma

emission ($I_{PL}(\lambda)$), the intensity of LED only ($I_L(\lambda)$), the plasma emission only ($I_P(\lambda)$) and the background ($I_{BG}(\lambda)$) are required and equation 2.26 can be rearranged as

$$-ln\left(\frac{I_{PL}(\lambda)-I_P(\lambda)}{I_L(\lambda)-I_{BG}(\lambda)}\right)=h\lambda B(\lambda)\phi(\lambda)\cdot L\cdot n_{OH} \tag{7.1}$$

The absorbance on the RHS needs to be rearranged for each ro-vibronic transition at wavelength λ_i. This finally forms the practical expression for OH density measurement by UV absorption spectroscopy as

$$-ln\left(\frac{I_{PL}(\lambda)-I_P(\lambda)}{I_L(\lambda)-I_{BG}(\lambda)}\right)=L\cdot\sum_i h\lambda_i B(\lambda_i)\phi(\lambda_i)n_i \tag{7.2}$$

where n_i is the fractional population of the rotational level of the transition i.

For details of the software used for OH density determination, the measured OH absorption spectrum as an input was fitted with the numerical spectra simulation software, which has been developed by K. Niemi [164] (see figure 7.2). The term $L\cdot n$ on the right hand side of equation 7.1 is an output of the fitting program. This finally needs taking into account the absorption length to determine the OH density. The concept and rotational constant were taken from [165] and line strengths for intermediate coupling from [166]. The software calculated relative Einstein coefficients and normalized to experimental lifetime value τ_0 = 0.688 μs from [167] of the non-rotational upper state, F_1 (J' = 0.5 , K' = 0). This results in the absolute Einstein coefficients which, agreed with [168]. In addition, the cross-check of the simulated absorbance spectrum with the high resolution measurement from [41] showed a quantitative agreement. A similar concept to determine the OH density by UV absorption spectroscopy is reported in [163] where all details and assumptions, such as rotational transition levels and instrumental broadening effects, are explained as well.

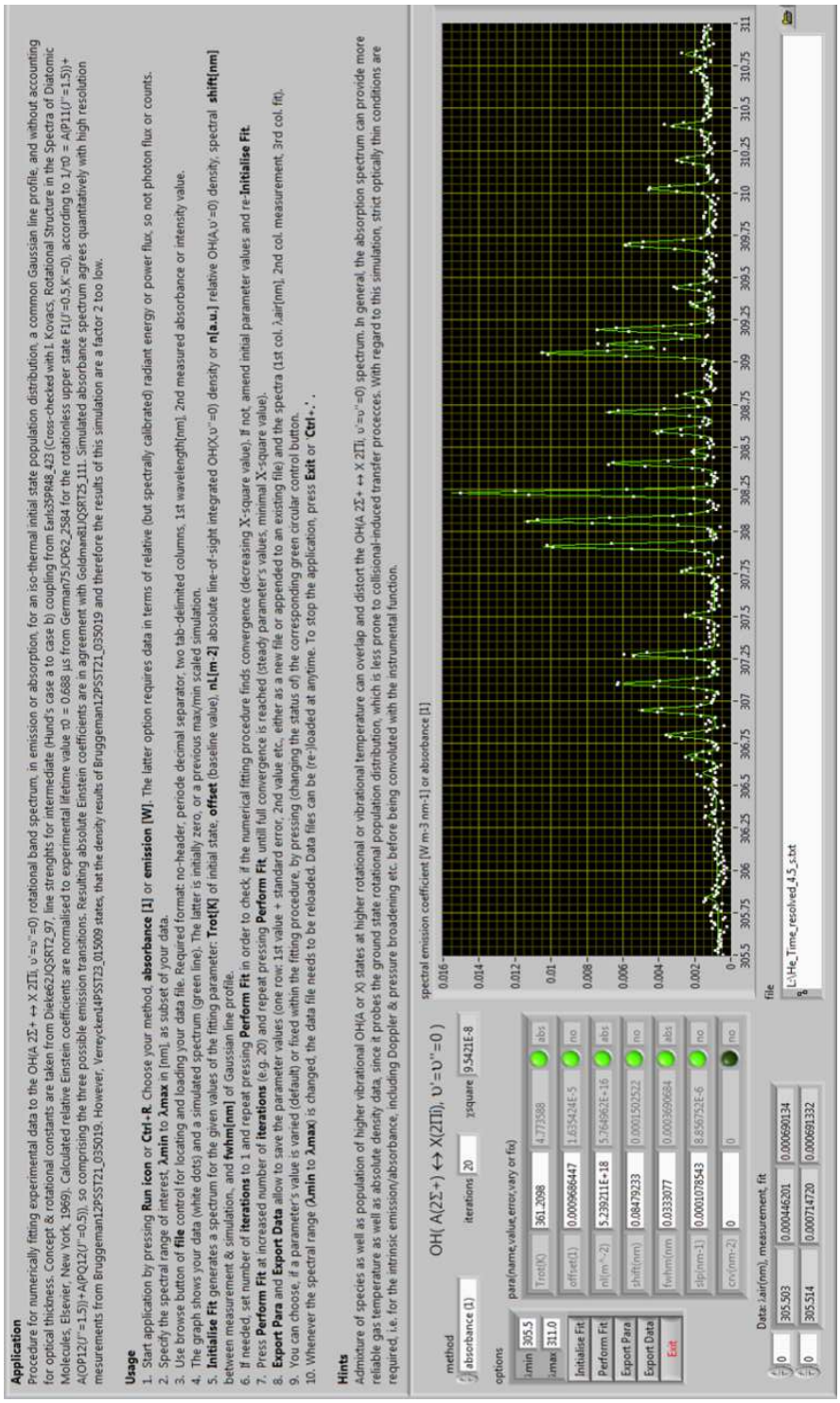

Fig. 7.2 OH(A-X) fitting spectra program developed by K. Niemi used for OH density calculation where all details described in the text.

7.2 UV-LED absorption setup for OH density measurement

As seen in figure 7.3, the plasma is generated between the two parallel electrodes with a 1-mm gap. The length of the electrode is 27.5 mm by 8.6-mm width. The 13.56-MHz RF discharge is driven by a RF generator (Coaxial-Power, MN 150-13.56) and coupled to the plasma with a L-matching network (Coaxial-Power, MMN 150).

In order to mix the water vapour to helium flow, the He tube was separated into two channels: channel 1 is pure helium and channel 2 goes through a water bubbler for carrying the water vapour. In channel 2, the He flow after the bubbler was assumed to be water vapour saturation satisfying the water vapour concentration determination [169]. The different flows of the two channels were controlled by two mass flow controllers (Brooks). The water-vapour helium flow in channel 2 varies from 50 to 2000 sccm and is mixed with pure helium to keep the total He inlet of the plasma source at 5 slm.

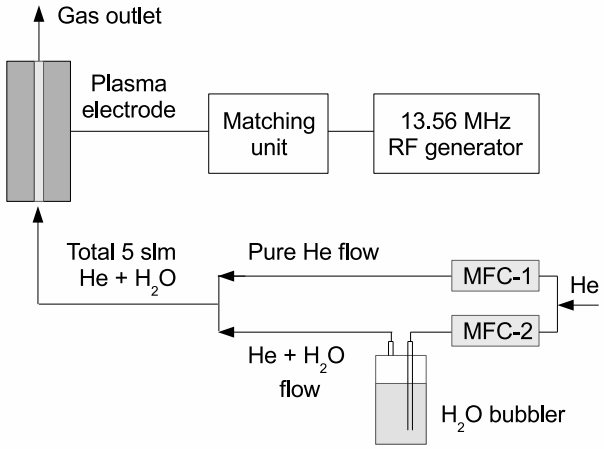

Fig. 7.3 Setup diagram for OH density measurement. Channel 2 of the He gas flowed through the H_2O bubbler for carrying water vapour.

The plasma channel was aligned with the optical path of the UV-LED setup. Based on the OH absorption principle in the previous section, the slit width is reduced to 50 μm from 950 μm in O_3 absorption setup in order to increase the wavelength resolution. The resulting FWHM of the OH spectrum is found to be about 0.032 nm, which still be able to isolate at least one transition line $P_1(2)$. The broadband UV-LED (Roithner Lasertechnik, UVTOP305-FW-TO18) was the light source, the spectrum of which is shown in figure 7.4, with center wavelength at 308.5 nm. In the experimental setup, the UV-LED for the OH measurement was attached in another controlling mounting box. It can replace the existing

mounting box used in the O_3 measurement and requires minor adjustment on the optical alignment. The LED signal was optimized with the controlling LED current at 19 mA and LED temperature at 21 °C.

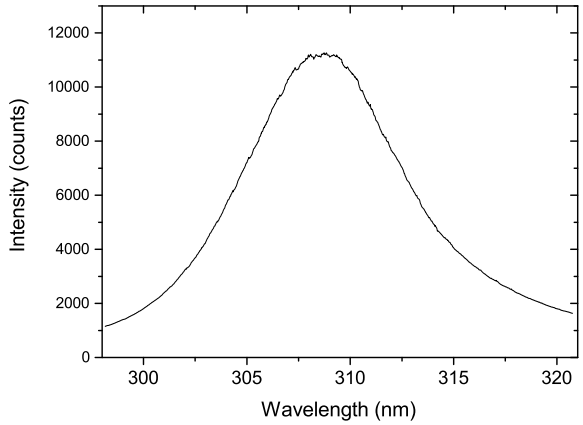

Fig. 7.4 UV-LED spectrum for OH density measurement, with the center wavelength at 308.5 nm.

The controlling signals were generated by the function generator to trigger the camera, plasma source, and LED-blocking chopper with different frequencies, at 0.20, 0.10, and 0.05 Hz, respectively. All signals were synchronized and optimized with the data-acquisition setup of the camera defining the conditions to measure I_{PL}, I_L, I_P and I_{BG} consecutively, as shown in figure 7.5. The camera operational time 2.5 s includes the exposure time 350 ms and the read-out time 1.29 s.

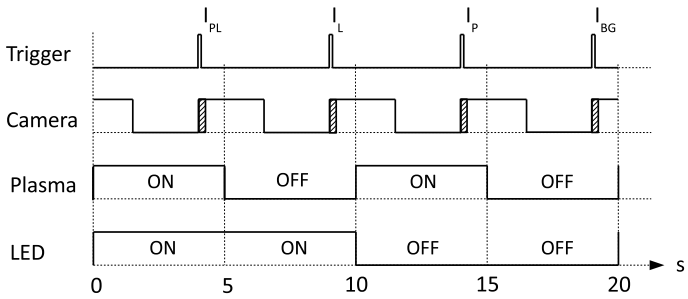

Fig. 7.5 Operational control signals for OH density measurements

The images of four quantities were resolved by the 0.5-m Czerny-Turner spectrograph (Andor, SR 500i) and taken by the equipped CCD camera (Newton). Further details are described in Chapter 3. The measured four images are presented in figure 7.6 and the ROI

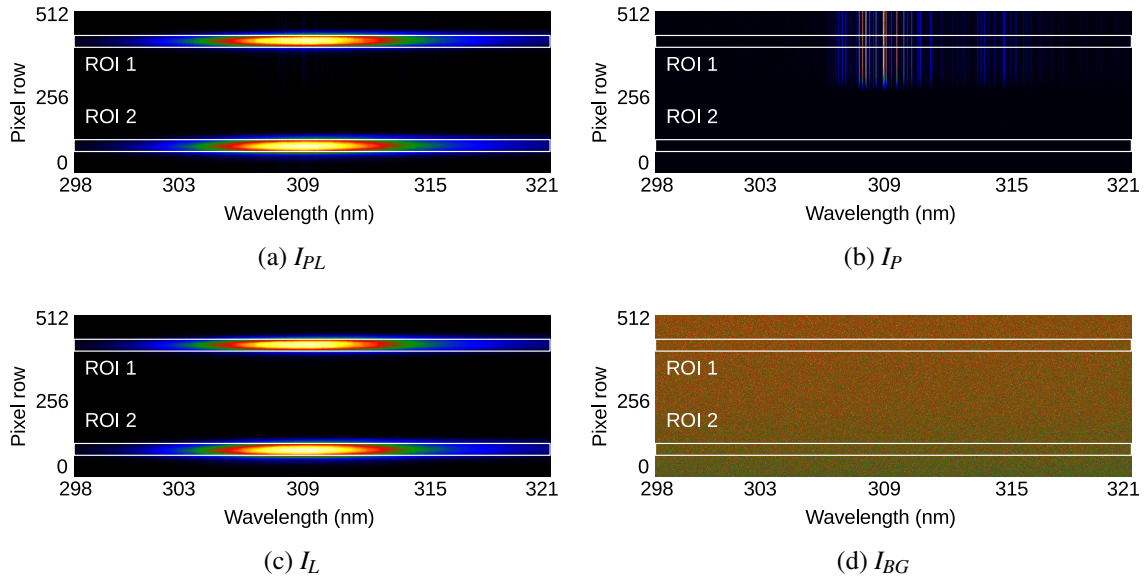

(a) I_{PL} (b) I_P

(c) I_L (d) I_{BG}

Fig. 7.6 CCD images of probe beam (pixel row 405-445 (ROI 1)) and reference beam (pixel row 70-110 (ROI 2)) intensities obtained with (a) LED and plasma, (b) He/H_2O plasma only, (c) LED only, and (d) without LED and plasma. The colours indicate the counts per pixel on a linear colour scale from min(blue) to max(yellow) values, respectively, where the maximum in (a) and (c) is approximately 2.75×10^4 counts.

1 of the probe beam is defined by FWHM in pixel rows (number 405-445) and covers all pixel columns (298-321 nm of wavelength). The signal of the probe beam was determined from the average on 40 pixel rows of the ROI. To increase the signal-to-noise ratio, the 50 consecutive images of each quantity were taken and averaged for the last spectrum signals used in equation 7.2.

According to the chemistry model in atmospheric pressure He-O_2 plasma with humid-air impurities [59], the OH density reaches the equilibrium state within a few ms. However, in the experiment condition, there is a possibility of non-plasma parameter effect on the OH density that need to be investigate. In the preliminary test, the OH density was found to be time-variation after plasma ignition. So, the time resolved measurement based on the UV-LED setup was employed to investigate for the equilibrium state of OH density after the ignition.

In this section, OH density was observed in the APP which was sustained by a total of 5 slm He:He+H_2O (4:1) or 4400 ppm H_2O concentration and 15 W RF power. The results are presented in figure 7.7. The density increases from 4.46×10^{14} cm^{-3} at about 500 ms after the ignition to about 4.70×10^{14} cm^{-3} after 3 s; then, the equilibrium condition can be found as the OH density keeps relatively more constant until 5 s. This could be caused

by the contribution of the plasma-power-coupling time and gas-temperature time variation. However, these effects are required different technique to investigate that beyond the scope of this part. Regarding to this discussion, in order to measure OH density with other plasma parameters, the equilibrium state, which based on the contribution of experimental parameter effects, should be taken into account and also be used to design the measurement.

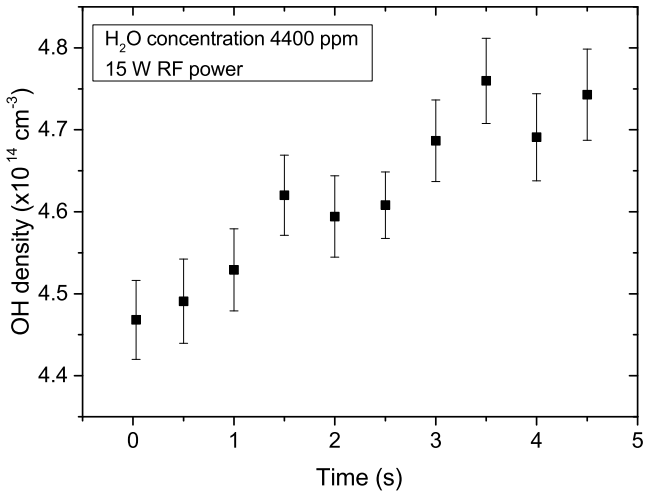

Fig. 7.7 Time resolved OH density in 13.56 MHz RF plasma with H_2O concentration 4400 ppm.

7.3 OH density in He + H_2O RF atmospheric pressure plasma

He/H_2O RF atmospheric pressure plasmas principally generate many reactive species such as O, OH, and H_2O_2. These species are potentially used in various applications. The study shows the strong dependence of these main species and the electrical discharge on the concentration of water in the plasmas [50, 170]. The densities are found to be increased with higher water concentration. Therefore, in this part, OH density as a function of H_2O admixture is based on this UV-LED setup and plasma operational regime. The results are shown in figure 7.8.

In figure 7.8, OH densities increased sharply from 0.8×10^{14} cm^{-3} at 220 ppm H_2O admixture to about 3.0×10^{14} cm^{-3} at 4400 ppm H_2O. Then, the densities slightly vary around 3.0×10^{14} cm^{-3} until the concentration is reached at 6600 ppm H_2O concentration, which was the saturation range of the OH density. Note that the ppm unit of H_2O concentra-

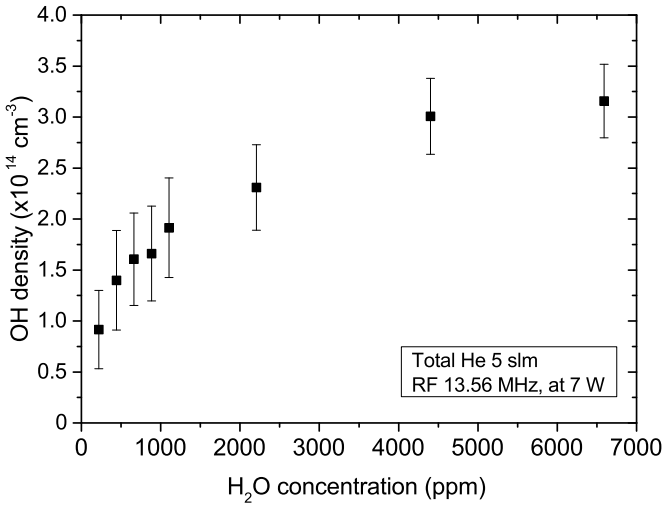

Fig. 7.8 OH density with water vapour concentration variation in 13.56 MHz RF APP, 7 W RF power and total 5 slm He.

tion was determined from the saturation vapour pressure formula (Magnus formula) [171]. This requires the temperature of the bubbler which was 19°C in this experiment.

The results were cross checked with measurements that has been done by S. Schröder using the broadband UV absorption. The compared technique was developed by Laboratoire de Physique des Plasmas (LPP), Paris. With the same plasma source and relatively high He+H_2O concentration range, the OH densities at 3.0 - 3.2 $\times$ 10^{14} cm^{-3} in the overlap range between 4400 and 6600 ppm H_2O showed a good agreement. The absolute OH densities are very close to each other at about 4400 ppm H_2O. Hence, this shows the potential of this UV-LED setup that can be adjusted to measure OH density.

7.3.1 Global model description

A global model is used to describe the physical and chemical mechanisms of the atmospheric pressure He + H_2O plasma and then identify the main reactive species and interactions. The He+H_2O plasma model, which developed by Liu et al. [50], includes 46 species. The dominant species of each particle type are, for example, electrons, OH^+, H_2O^+, $H_2O_2^-$ for charged species, He*, O(^1D) and OH(A) for metastables, H_2O_2, OH, O and H for neutrals. These species relate to 577 reactions taken from all possible relevant species considered in different typical plasmas, such as He+O_2 [124], He [172], and He+air [139].

The OH density can be obtained by the assumption that the production and destruction

processes of OH are balanced. Based on the assumptions and detailed description in [173], the detailed balance equation can be expressed in equation 7.3.

$$n_e n_{H_2O} k_d = n_{OH}^2 k_{loss} \tag{7.3}$$

where n_e, n_{H_2O} and n_{OH} are electron, water, and hydroxyl densities, respectively. The destruction rate coefficient k_d of H_2O acts as the production rate of OH. The main channel mechanisms of OH are the electron impact dissociation of H_2O (e + H_2O → H + OH + e) and the dissociative electron attachment to H_2O (e + H_2O → OH + H^-). For k_{loss}, the losses are due to the self-destruction of OH (OH + OH → H_2O_2) and destruction by H (OH + H → H_2O). It can be stated that OH density strongly depends on the H_2O vapor concentration by these main production and destruction mechanisms.

7.4 O_3 density in He + O_2 + H_2O atmospheric pressure plasmas

In biomedical plasma applications, RONS have been investigated for their significant roles and mechanisms in the observed biological responses. For the practical environment, water is contributed due to the humidity of ambient air and the moistness of biological samples. Therefore, He + O_2 + H_2O discharges are of particular importance to investigate. The mechanisms were studied by McKay et al. [174] using one-dimensional fluid simulations, which included 61 species and 878 reactive species. For the application, this kind of plasma was applied for sterilization [156]. With the potential of the UV-LED setup, in this section we concentrate on the O_3 density in He + O_2 + H_2O RF atmospheric pressure plasmas.

The experimental setup is the same as presented in figure 7.3. The 0.5% and 0.7% O_2 admixtures were added into the total 10 slm He via He channel 1. The O_3 densities were measured as a function of H_2O concentration varied up to 4400 ppm in 13.56 MHz RF APP at 9 W of RF power and 11 absorption length. In addition, 0.1% artificial air N_2:O_2 (4:1) was also added in a 0.5% O_2 admixture case to observe its influence on the O_3 density as well. Under these conditions, the O_3 density results with the variation of the H_2O concentration are shown in figure 7.9.

Related to the mechanism description [50, 174], the presence of water introduces the addition of loss reactions of O_3 by H, OH atoms which are

$$H + O_3 \rightarrow OH + O_2 \tag{7.4}$$

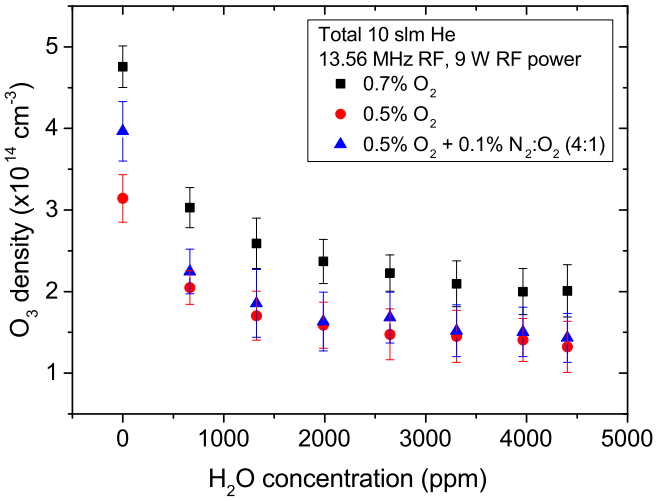

Fig. 7.9 O_3 density in He + O_2 + H_2O atmospheric pressure plasma. The total He is 10 slm He. Artificial air (N_2:O_2 = 4:1) admixture was added for more practical conditions.

$$H + O_3 \rightarrow O + HO_2 \tag{7.5}$$

$$OH + O_3 \rightarrow HO_2 + O_2 \tag{7.6}$$

The production of reaction (7.4) yields the oxygen and oxygen-hydrogen, which are the main pathway of O_3 destruction. With higher H_2O concentration, the destruction mechanism of O_3 increases and produces more O-H species. As a result, the O_3 densities decreased to a saturation level as the water admixture increased. In addition, for two different O_2 admixture cases, it is reasonable that the O_3 density is higher for a higher $\%O_2$ as there are more O_3 production sources.

The analysis in the case of the artificial air admixture has to take into account the spectral emission that dominates the O_3 absorption region, as shown in figure 5.4 (a). The 0.1% additional air shows a slight effect on the absolute value of the O_3 density. The trend is decreasing toward a saturation level, similar to the previous two cases. However, the simulations in this discharge condition have not been covered. So, it is a very interesting investigation for future work since this plasma condition is relatively close to the practical applications.

Chapter 8

O_3 in CO_2-CO conversion condition with plasma power measurement

With the broad range of applications for the atmospheric pressure plasmas, one of the interesting applications which related to the global issues is to convert the greenhouse gas CO_2 into a value-added chemical, carbon monoxide (CO). CO, product of the plasma-CO2-conversion process, is an important molecule of synthesis gas for the synthesis fuels and chemicals. Fundamentally, non-thermal atmospheric pressure plasma can enable thermodynamically unfavorable chemical reaction to occur at close-to-room temperature and atmospheric pressure. At the same time, it still generates a high number of reactive species and electrons. The mean electron energy is between 1 and 10 eV which is the range for exciting atomic and molecular species and breaking chemical bonds. CO_2 dissociation in plasma requires about 5.5 eV in breaking the OC=O bond by stepwise vibrational excitation [64]. Therefore, this shows the potential of non-thermal plasma in an efficient CO_2 utilisation process, as it can overcome the stability of CO_2 without the need of high temperature in thermal catalytic processes.

In this plasma CO_2-conversion process, O_3 density which contributes to the main reactions will be investigated in this chapter. In 0D global kinetic model of CO_2 conversion in RF APP developed by A. Foote. [175], the main channel of CO_2 destructions are most contributed by collision with neutral carrier ($CO_2 + M \rightarrow CO + O + M$) where M is neutral carrier particle. The second most dominant process is reaction with oxygen ($CO_2 + O \rightarrow CO + O_2$). While the less two dominant reactions are Penning dissociation ($CO_2 + M^* \rightarrow CO + O + M$) and electron impact ($CO_2 + e^- \rightarrow CO + O + e^-$). During the residence time, O atom can recombine into O_2 or O_3 and the reactions between O, O_2 and O_3 can then occur. These reactive oxygen species densities have a significant effect on the balance

between the O_2 and O_3 production.

It is obvious that O_3 has a significant contribution to the main reactive species formations and to the conversion reaction products. Therefore, it is important to investigate O_3 density in the CO_2-CO conversion plasma environment. The common plasma types for CO_2 conversion are DBD [61, 176], microwave plasma [177, 178] and gliding arc [179]. This typical microwave plasma [177] gives the highest energy efficiency of up to 90%, but it is needed to operate at a relatively low pressure (100-200 Torr) and requires supersonic gas flow. However, when plasma operates at atmospheric pressure desirable for industrial applications, the energy efficiency decreases to 40% [180] compared to the low pressure case.

Several techniques have been investigated in order to optimize the conditions of the conversion and energy efficiency in atmospheric pressure. For example, inserting a dielectric packing into the reactor, also called packed bed DBD reactor, adding H_2 or CH_4 in CO_2 plasma, and adding fraction CO_2 into Ar or He RF atmospheric pressure plasmas which has been done by M. Ramakers et al. [181]. In this work, the optimization condition is to add CO_2 in He 40.68 MHz atmospheric pressure plasma. As discussed above and in the previous studies, the high frequency plasma in microwave frequency (GHz) at 100 W [182] and the RF plasma at 13.56 MHz at 1kW [63] yielded very high conversion, but there was an issue of conversion energy efficiency between these two frequencies that sill needed to be optimized. Therefore, the 40.68 MHz (one of frequencies between) RF plasma was taken for the study.

Furthermore, the energy efficiency of the conversion is one of the main interesting factors. Plasma power is needed to be investigated by power measurement technique which will be discussed in the last section. O_3 density as a function of the plasma power is presented under this typical condition, and the results are discussed based on the (0D) global model with Globalkin simulation program done by A. Foote. [175].

8.1 O_3 density in He-CO_2 RF 40.68 MHz APP

In single-frequency capacitively coupled plasmas, electron density is higher with a higher harmonic. Since the electron impact dissociation is the main channel of CO_2 breakdown, the higher number of energetic electron increases the dissociated product of CO_2. The operational RF frequency is preferable at a higher harmonic. However, the higher RF frequency leads to higher electrode temperature that can damage the plasma source. In the used plasma source, the highest driving frequency without the temperature electrode damaging

and requirement of cooling system is at 40.68 MHz, or the 3^{rd} harmonic of 13.56 MHz RF frequency.

8.1.1 Experimental setup

In figure 8.1, the experimental setup is changed to operate the plasma with 40.68 MHz by fixed frequency RF power generator (Advance Energy, Dressler Cesar, 403, 300 W). The matching box is π type with load 49, inductor 132 and tune 113.5 for this operation condition. The admixture gas is CO_2 with 99.90% purity. The operational control system is operated based on 0.4 Hz of LED light (On-Off). Since the plasma power measurement is required for energy efficiency investigation in CO_2 conversion, the HV probe and current probe were connected between the matching unit and the plasma source. The voltage and current signals were collected by the oscilloscope (2 GHz, LeCroy, WaveRunner, 204MXi-A) for the plasma power measurement.

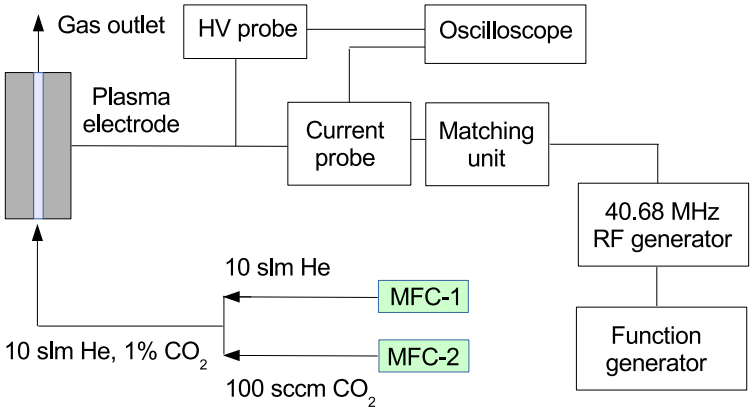

Fig. 8.1 Experimental setup diagram for O_3 density in He with CO_2 admixture and the connection with plasma power measurement devices required in CO_2 conversion for energy efficiency investigation.

For data acquisition details, the measured four images for O_3 density calculation are shown in figure 8.2. In figure 8.2 (b), the emission spectrum pattern was stronger with higher RF powers. Some strong emission lines were generated through reactive excitation carbon-oxygen based species, for example the first negative band CO^+ at 256.75 and 256.66 nm [183] and by CO ($b^3\Sigma$ - $a^3\Pi$ ($v' = 1, v'' = 0$)) at 265 nm [184].

These emission lines dominate the absorption range which cannot be used for O_3 density calculation. However, the non-dominated absorption range was found at 261-262 nm for 1-

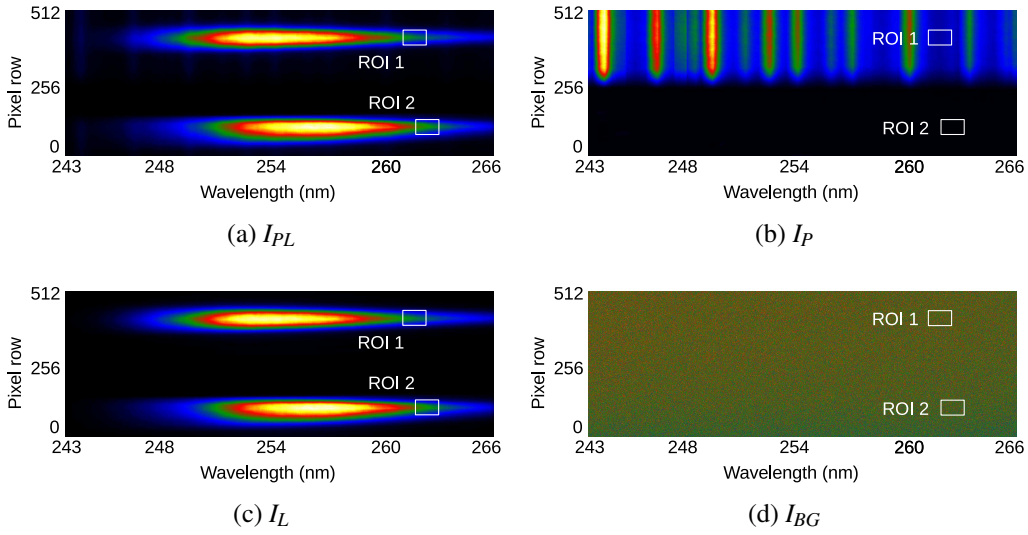

(a) I_{PL} (b) I_P

(c) I_L (d) I_{BG}

Fig. 8.2 CCD images of probe beam (pixel row 370-470 (ROI 1)) and reference beam (pixel row 40-140 (ROI 2)) intensities obtained with (a) LED and plasma, (b) He/CO_2 plasma only, (c) LED only, and (d) without LED and plasma.

nm width, as shown in figure 8.3. This width was defined as the new ROI for O_3 density calculation throughout this section (see figure 8.2 for images of four quantities). Based on the two-beam calculation, the preliminary results showed the error is two order magnitude below the absolute value of O_3 density, which obviously have high enough signal-to-noise ratio.

Additionally, the broader wavelength range is observed through optical emission spectroscopy using HR4000 spectrometer (Ocean Optics, UV-NIR). The spectral lines in CO_2 admixture at minimum and maximum RF powers are compared to the case of O_2 admixture. In figure 8.4, the emission spectrum at the maximum power in CO_2 condition dominates the absorption wavelength regimes. As a result, the nearest unaffected absorption range are at 267-271 nm and 275.5-280 nm, which has about 4 nm width. However, the absorption cross section are about 80-50% of the cross section in 255 range [107]. This could be an option that is worth investigation when the signal to noise ratio in the default ROI is very low.

8.1.2 O_3 density with parameter variations

O_3 density in He/CO_2 with RF power variation

Ozone density with the function of RF power is basically the first fundamental variation to be investigated. The operational RF powers range from the full-channel homogeneous

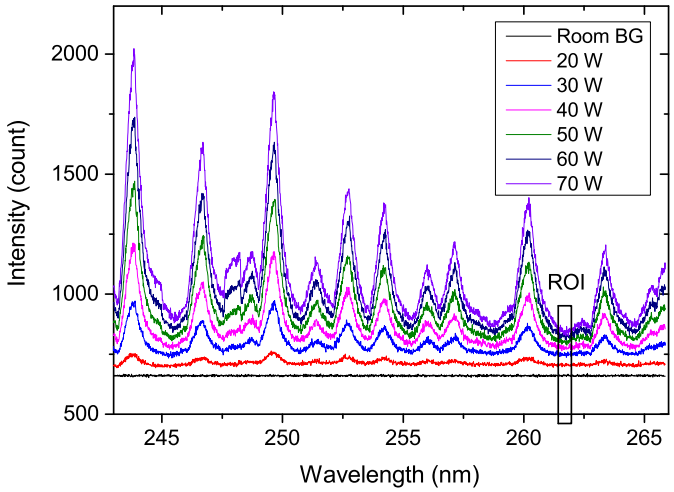

Fig. 8.3 Plasma spectrum include the emission spectral peaks and the 1-nm width absorption wavelength range between 261 - 262 nm.

discharge to near arcing discharged mode. At relatively high radio frequency, 40.68 MHz, the forward RF power with some variation of the reflected power read from the RF function generator can be observed. This implicates the amount of RF power coupled into the system, including the connection cable, adapter and the plasma source with some power reflected back to the generator. The preliminary O_3 density with parameter variation is RF powers while the actual power coupled with plasma will be discussed later.

For the preliminary results, in figure 8.5, the O_3 density increases as a function of RF power by factor of 7 from 3.8×10^{14} cm^{-3} to 25.1×10^{14} cm^{-3}. The approximate power rises from 20/2 W (forward/reflected) to 70/18 W.

Considering a zero-dimension chemical reaction kinetics model in He/CO_2 RF APP developed by A. Foote [175], the most important reactions of CO_2 splitting are the collision with neutral carrier ($CO_2 + He \rightarrow CO + O + He$) into CO and O, reaction with oxygen ($CO_2 + O \rightarrow CO + O_2$) yield CO and O_2, and electron impact dissociation ($CO_2 + e^- \rightarrow CO + O + e^-$) generated CO and O.

For the effect of He, in He with about 1% CO_2 admixture plasma, the electrons do not rapidly lose their energy through inelastic collision with He since He has higher threshold energy than CO_2. So, this increases the mean electron energy, and leads to the relatively high rate constant of electron impact excitation and dissociation.

Additionally, the higher RF plasma power principally implies towards a higher number of electron density [57]. These contributions create higher number of electron impact exci-

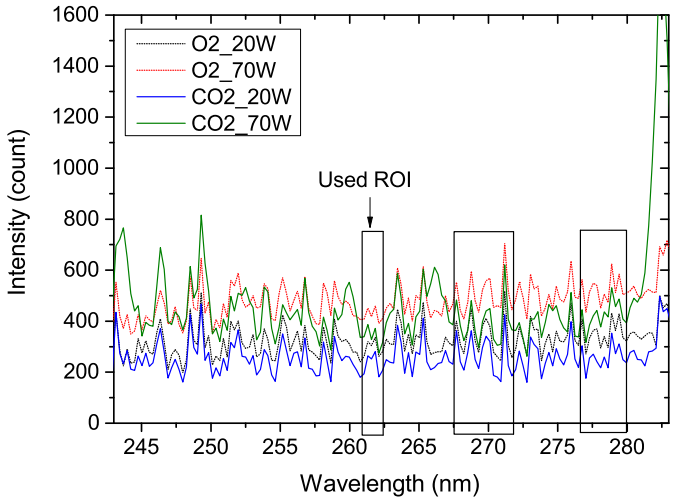

Fig. 8.4 Broadband He+CO_2 plasma spectrum includes the used 1-nm width ROI(261-262 nm) and other unaffected ROI(267-271 nm) and ROI(275.5-280 nm).

tation of CO_2 and leads to CO_2 dissociation, yielding CO and O, ($CO_2 + e^- \rightarrow CO_2^* + e^- \rightarrow CO + O + e^-$). With shorter residence times, the O atom will almost immediately recombine into O_2 and O_3. Therefore, higher RF power increases the atomic O density and leads to higher O_3 density through the recombination of O, O_2 and O^- as shown in figure 8.5.

O_3 density in He/CO_2 with CO_2 admixture variation

Related to the previous section, the O_3 density in He/CO_2 RF plasma was investigated with the variation of %CO_2 variation. The results are shown in figure 8.6. With the increase of CO_2 admixture from 0.1 - 1.0%, O_3 density linearly reduces from 7.34 $\times$ 10^{14} cm^{-3} to 3.26 $\times$ 10^{14} cm^{-3} respectively.

According to the 0D chemical kinetics description above, in the higher CO_2 admixture, the number density of the neutral species is increased comparatively to the electron density. This possibly leads to the reduction of the CO_2 dissociations and lower number of O atom and O_2. Consequently, it reduces the formation of O_3 densities though less oxygen-based species production.

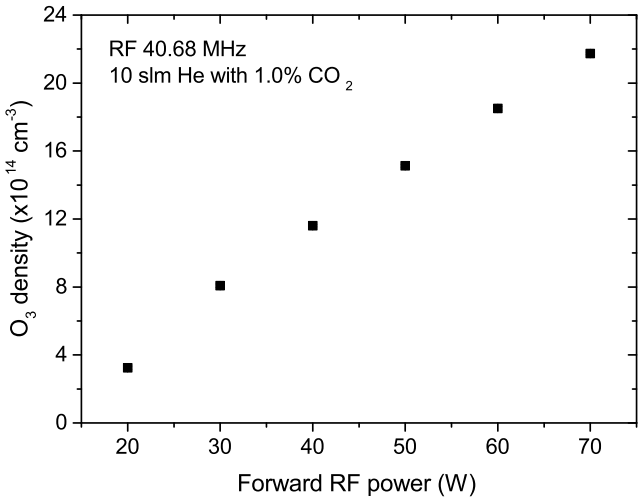

Fig. 8.5 O_3 density increases with the forward RF powers at 40.68 MHz, 10 slm He with 1.0% CO_2 admixture.

8.2 O_3 density with plasma power measurements

The most important factor in CO_2 conversion is the conversion efficiency [178]. This concerns how specific energy has been put into the conversion process. In this He/CO_2 RF plasma, the exact powers which were coupled into the plasma were investigated with the O_3 density measurement. When considering the RF plasma sustaining system, the power read on the power generator provide forward and reflected powers coupled into all electrical components. The actual plasma power needed to be investigated without the electrical contribution of the structures and connection cables. Plasma power can be calculated through equation 8.1. The method of plasma power measurement has been introduced by A. West [128].

$$P_{plasma} = \frac{IV_{on}}{2}\cos(\theta_{on}) - \frac{IV_{off}}{2}\cos(\theta_{off}) \tag{8.1}$$

where θ is the phase angle between the sinusoidal voltage and current signals, subscript on and off denote for plasma on and plasma off conditions, respectively. The plasma off refers to the condition where the background He/CO_2 gas is off and plasma can not be ignited, while the RF power still provide to the electrodes.

For measurement, the voltage and current signals composes of the real and complex parts, which represent the phase difference, defined as $z = x + iy$. Details of signals analysis is needed to be taken into account, as explained in [128], like the fast Fourier transform

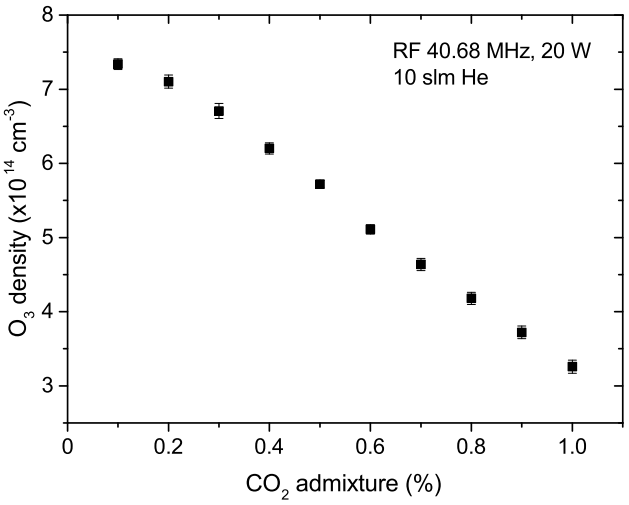

Fig. 8.6 O_3 density decreases with the % CO_2 admixture in 10 slm He, at 40.68 MHz RF and 20 W forward RF powers.

(FFT) for finding the corresponding driving frequency of the voltage and the current signals and the calibration of amplitude of the signals with detection sample size. As an example of the correction factor, the temporal phase angle of voltage, θ_V, and current, θ_I, can be defined as θ_V, $\theta_I = \tan(y/x)$. The different phase angle between both signals is $\theta_{V-I} = \theta_V - \theta_I$ that is subtracted by the instrumental phase angle θ_i. Then, we have $\theta_{plasma} = \theta_{V-I} - \theta_i$. In addition, the instrument phase angle is defined as $\theta_i = \theta_{V-I} - \theta_c$, which θ_c is the known phase angle of the air-boxed capacitor.

With these correction factors, the P_{off} can be determined and interpolated by fitting function for wide range of the current. The function is in the form of $P_{off} = I^2 R_{off}$ which is $20.9I^2$ - $7.14I$ + 6.74, as shown in figure 8.7. Then, equation 8.1 can be developed to

$$P_{plasma} = \frac{IV_{on}}{2}\cos(\theta_{on}) - P_{off}(I) \tag{8.2}$$

In the first term of the right hand side of equation 8.2, the plasma on with some values can be determined, and the results of the power when plasma is on and off are shown in figure 8.7. Then, the absolute power in the final form with the current equivalent is expressed through equation 8.3.

$$P_{plasma} = P_{plasma-on}(I) - P_{plasma-off}(I) \tag{8.3}$$

As a result, the absolute plasma power is shown in figure 8.8. The operational voltages

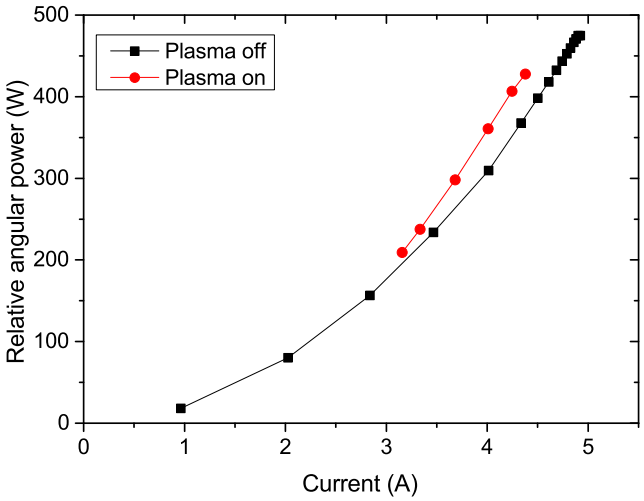

Fig. 8.7 Angular power as a function of current when the plasma on and off are used to determine the exact plasma powers.

range from 147 V to 200 V, with the increase in the coupled plasma power from 16 W to 53 W. The powers are about ten times higher than the coupling power in the μAPPJ [127] at 40.68 MHz. It is reasonable as the discharge area is about ten time larger.

O_3 with the plasma powers are finally plotted in figure 8.9. The final plasma-power data point is found to be lower than the previous data point. It is assumed that the plasma is close to γ mode operational regime, which include filament structure. This mode couples with less power but creates more number of electrons that produce more oxygen species through e-CO_2 splitting processes. Therefore, the O_3 keeps rising with higher number of oxygen species in the last data point.

The results provide information on O_3 density with plasma power in He/CO_2 RF capacitively coupled APP. It is fundamentally important since the first product of the main reactions of CO_2 conversion was oxygen-based species which directly depends on O_3 formation. In addition, the atmospheric pressure plasma with He/CO_2 showed promise in better CO_2 conversion efficiency have been studied for its highest optimisation condition with many chemical kinetic models. The experimental measurement for the main particle species is essential as shown in this section for O_3 density measurement with the developed two-beam UV-LED absorption technique.

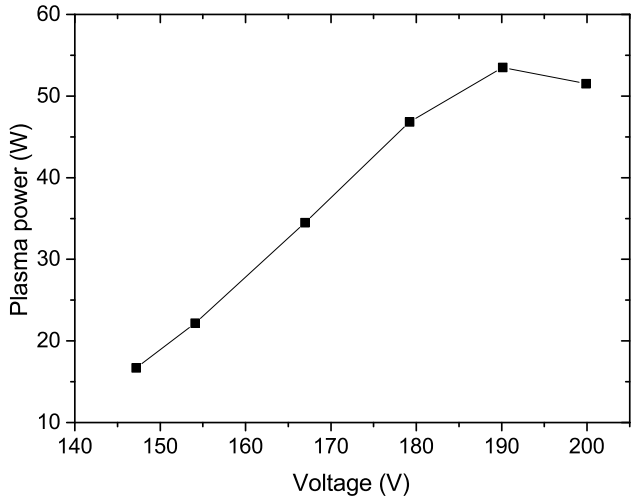

Fig. 8.8 Plasma power at 40.68 MHz, 10 slm He with 1.0% CO_2.

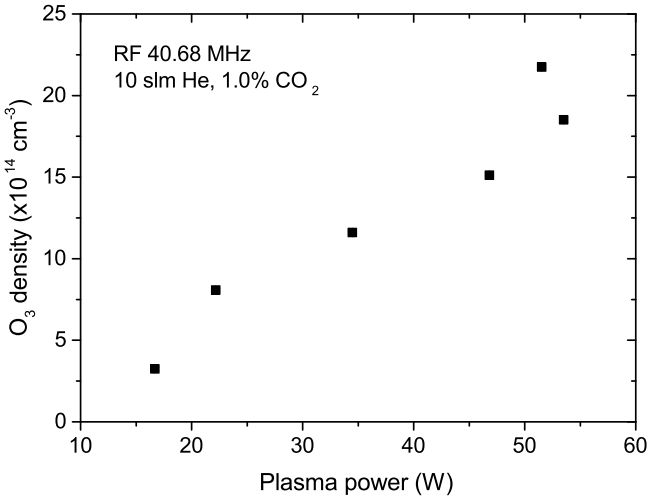

Fig. 8.9 Ozone as a function of plasma power at 40.68 MHz, 10 slm He with 1.0% CO_2.

Chapter 9

Summary and conclusion

9.1 Discussion and summary

In the study of low-temperature atmospheric pressure plasmas for biomedical applications, the key effective radicals for related biological results seem to be one of most challenging issues. These require contributions from different aspects of knowledge, theories based on numerical modeling, and diagnostic techniques for each interesting species. As discussed in all chapters, this work is devoted to the fundamental development of UV absorption spectroscopy. The developed two-beam UV-LED absorption spectroscopy technique provides an improvement in the diagnostics of ozone density, which is principally formed through a complex chain of reactions.

In terms of achieving the optimization conditions for measuring ozone density with plasma parameters in the small plasma volume, the deviation of non-plasma parameters can potentially influence the absolute ozone density. With a 1 mm gap between two electrodes, the probe beam behaviour strongly depends on the condition of the gap, as indicated by electrode temperature variation and compared to the reference beam intensity. This directly effects the measurement of the four absorption quantities since they require that the plasma be turned on and off. It takes approximately 30 minutes to reach the equilibrium condition needed to perform individual absorption quantity measurements. The two-beam UV-LED absorption setup was optimised by timing signals to suppress these electrode temperature variations. The measurement time was optimized with the CCD camera so that readings could be taken in just a few seconds and relatively independently from the electrode temperature variation. Furthermore, the operating signals allowed the setup to consecutively record a high number of measurements, which is essential when it comes to improving the signal to noise ratio.

In addition, the Mach-Zehnder configuration provided an image of both beams while the ratio of their intensities was constant over the measurement period. The ratio was taken into account in the formal absorption equation and significantly reduced the error by a factor of two or three. For the study of a 13.56 MHz RF driven capacitively coupled atmospheric pressure plasma (11 mm absorption length), the minimum ozone density detection limit was $9.0\pm\ 0.9\ \times\ 10^{13}$ cm^{-3} at 0.1% O_2 and 10 slm He. Due to the beam's relatively small 1 mm diameter compared to the approximately 30 cm of optical alignment space, the setup is capable of detailed spatially resolved measurement. The ozone density along the plasma channel showed that the build-up period reached the equilibrium approximately 1.75 ms or so after the middle of the channel. The center of the equilibrium range is the position where the ozone density was measured as a function of plasma parameters.

The ozone density was measured as a function of the plasma properties. Firstly, since most factors in all physical and chemical processes within the plasma are related to the electron energy probability function (EEPF), there was a need to investigate this in particular the relation with the ozone density. The electron density, which relates to the EEPF, proportioned to the plasma coupling power. The ozone density with this primary factor, as represented by plasma powers, was found to be decreased. However, the electron contribution to ozone production and destruction mechanisms was relatively small, which implies that the ozone with the plasma power is relatively constant without the gas temperature effects. On the other hand, the gas temperature strongly depends on the plasma power, as electrons transfer their kinetic energy through elastic and inelastic collision with the gas molecules. Additionally, the destruction rate coefficients of the ozone are proportioned to the gas temperature, thus meaning that the ozone density shows a strong anti-correlation with the gas temperature as a function of plasma power. In the case of O_2 admixture variation with constant power, the gas temperature dropped with higher $\%O_2$ while there was a clear increase in O_3 density.

The driving frequency can also be pulse modulated and was found to influenced the delivered ozone density. In He with O_2 admixture, the pulse modulation frequencies of 10 kHz with different duty cycle strongly affected the equilibrium range in a 30 mm plasma channel. The time period of this kHz modulation frequency is comparable to ozone formation time before reaching the equilibrium. Thus, less duty cycle gives longer plasma-off time and consequently allows for a longer ozone formation period. However, using He with an artificial air admixture, the introduced nitrogen molecules provide a more complex chemical mechanism. The preliminary result for the frequency and duty cycle modulation shows different trends from the case of He with only O_2 admixture. A full investigation of the

reaction mechanisms require a 0D semi-kinetic model description that is beyond the scope of this study.

In terms of the biomedical application aspect, the role of ozone density was investigated in bacterial inactivation. The spatially resolved ozone density was determined in the effluent of the co-axial kHz DBD atmospheric pressure plasma jet when applied downward to a biological sample. The plasma jet was perpendicularly applied to the plate at a distance of 30 mm. Both the jet and the plate were at a fixed distance and attached to an x-y movable stage which is required for spatially resolved measurement. An Abel inversion was used to transform the Cartesian-coordinate symmetric absorption profile into the radial ozone density distribution. The O_3 densities with higher $\%O_2$ admixture showed a broader cross section profiles at 1 mm above the agar plates. The cross section profiles and local absolute densities were increased in the bacterial killing zones but not exactly correlated. Thus, the ozone might be one of the reactive species in bacterial inactivation and could well synergize with other reactive species. There is still a need for additional investigation of the potential nitrogen reactive species which contribute to the effluent mechanisms.

The 2D ozone density in the effluent region was also examined in order to gauge its physical and chemical contributions due to the setup configuration and ambient air flows. The ozone production kept rising along the propagation axis up to the surface 30 mm away. The main reason behind this increase is thought to be the recombination of the atomic and molecular oxygen which is rapidly converted and has relatively short life-time compared with ozone. Following this, in the area off the propagation axis, the role of short-lived species decreases, while the contributions from the long-lived species and the physical air flow play an important role.

In addition to the possibility of reactive nitrogen species in the effluent region, the hydrogen-oxygen based reactive species are also involved as a key reactive species, with a small fraction of them present in the form of humidity. An analysis of OH density through the use of UV-LED absorption spectroscopy was performed. The OH absorption spectrum was separated to produce each narrow line profile that was required for the density calculation using the in-house program developed by K. Niemi. The temporally resolved OH density was achieved with the modulation of controlling signal of the setup. It was found that just over 3 seconds was needed for the OH density to reach equilibrium after plasma ignition. The increase of OH density with higher $He+H_2O$ admixture based on this setup agrees well with the results yielded when the broadband UV absorption technique (developed by LPP group) was used. This confirms the potential of the developed UV-LED absorption setup in measuring different species.

Ozone density can also be an important species in other chemical reaction environments. For CO_2 conversion, RF-driven atmospheric pressure plasma is found to be an efficient source of CO production. The ozone densities were observed in He with fraction of CO_2 admixture of 40.68 MHz RF-driven APP. The energy efficiency, which is an important factor for this conversion, was directly related to the energy coupled into the plasma. The results showed that the ozone density increased as a function of plasma power in the range of 15-55 W at voltage amplitudes of 150-200 V. It is approximately ten times higher than the plasma power of the COST reference microplasma jet which has the plasma volume about ten times smaller.

In summary, this research has

- provided the two-beam UV-LED absorption diagnostic technique with the potential in spatial measurement of O_3 and OH densities in the small volume plasma with the reduction of the uncertainty by factor of 2-3 compared to the common one beam measurement.

- clarified strong dependence and anti-correlation of O_3 density with gas temperature as function of plasma power and $\%O_2$ admixture in He/O_2 RF plasma.

- provided plasma chemistry description and main production and destruction mechanisms of the experimental conditions based on full plasma chemistry model.

- identified the dependence of O_3 density on kHz-frequency and duty cycle modulation factor of He/O_2 and He/0.5% air RF plasmas.

- verified that O_3 is not the only effective species in bacterial inactivation based on the study of correlation between O_3 density profile and biological results.

- observed 2D O_3 density in the effluent region applied over the surface sample.

- showed the potential of the developed setup in alternatively investigation of the OH density in He/H_2O vapour RF plasma.

- investigated O_3 density with plasma power in CO_2 conversion plasma at 40.68 MHz which is one of the interest application related to technology solving the global warming issue.

9.2 Outlook

The understanding of low-temperature atmospheric pressure plasmas for future technological application requires a wide range of knowledge and cooperation from numerous scientists. While theoretical simulation models are being developed to overcome such unknown factors, the diagnostic techniques are also being improved in order to accurately analyze experimental information generated from complex chemical reactions and a huge number of particle species. The developed two-beam UV-LED absorption setup showed a significant improvement in terms of the absorption spectroscopy for measuring ozone density. The complexity of the production and destruction channels of ozone is still an open question in terms of the most important reactions.

The key role of reactive species in biomedical applications is also an active topic. The study of ozone density using the developed UV-LED setup to gauge the correlation with the bacterial inactivation area can indicate the importance of ozone in this process. However, a number of investigations must be conducted in order to detect any possible reactive species, such as nitrogen and hydrogen-oxygen species, before conclusions can be drawn for the importance of the various species. For such conditions, the density is beyond the detection limit, thus presenting a further experimental challenge which requires more advanced diagnostic techniques. For example, measurement of OH in the effluent is found to be not possible through use of the two-beam UV-LED absorption technique due to the low density and short lifetime. Instead spatially resolved OH density in the effluent region of a He/H_2O co-axial kHz dielectric barrier APPJ applied to a biological sample can be measured by using the LIF technique. With this said however, such an experiment is beyond the scope of this work.

The ozone density measured by the two-beam UV-LED setup provides direct information with regard to tailoring the delivered key reactive species by changing the the plasma parameters, such as plasma power and modulation driving frequency. This is more than can be provided by the numerical simulation perspective since the principle question still relates to the most important reactions. Moreover, values for reaction rate coefficients are sometimes based on theoretical predictions and non-publishing sources. Therefore, the development of a diagnostic technique with which to understand fundamental and application perspectives represents essential work. Indeed, with this purpose in mind, there is a definite need for solid information from theoretical simulation, as this would make a significant contribution to research on low-temperature atmospheric pressure plasma with broad technological applications.

Appendix A

O_3 absorptions in the effluent region with vertical treatment samples

A.1 O_3 absorption profile with vertical treatment sample

The absorption profiles were influenced under the conditions where the sample plates were treated in vertical direction as shown in figure A.1 and A.2. The vertical plates introduced more complicate air flows that change the absorption in all directions. Obviously, the measured absorption profiles are not possible to determined the absolute O_3 density as they are not symmetry based on Abel's inversion assumption.

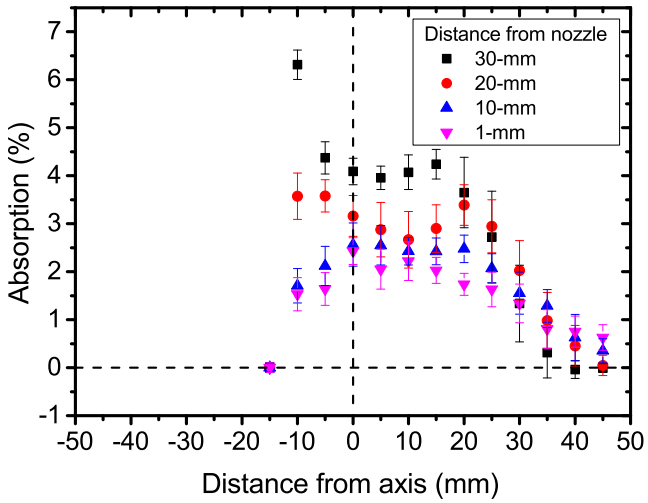

Fig. A.1 The vertical O_3 absorption profiles in the effluent region with different distance from the nozzle. The sample plate is at 10-mm from the propagation axis.

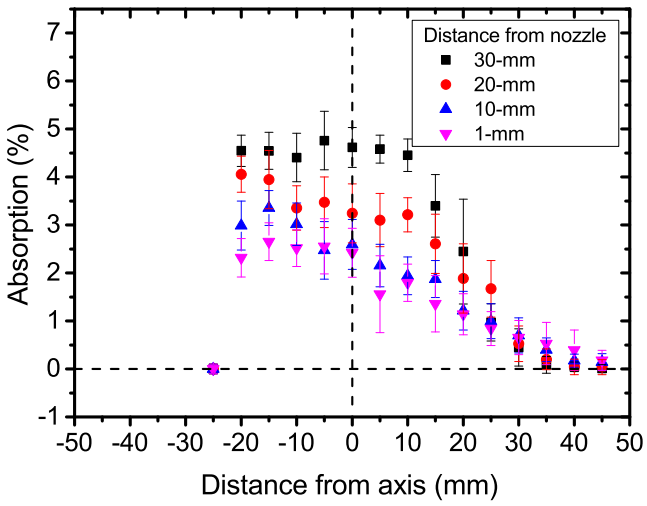

Fig. A.2 The vertical O_3 absorption profiles in the effluent region with different distance from the nozzle. The sample plate is at 20-mm from the propagation axis.

To investigate the influence of distance-from-axis effect, three absorption profiles at 20-mm from the nozzle were measured with the sample plates placed at 10, 20 and 30 mm from the axis as shown in figure A.3. The absorption near the sample surface show unpredictable variation. Therefore it is not possible to access and also having a clue of the absolute O_3 density under this measurement configuration.

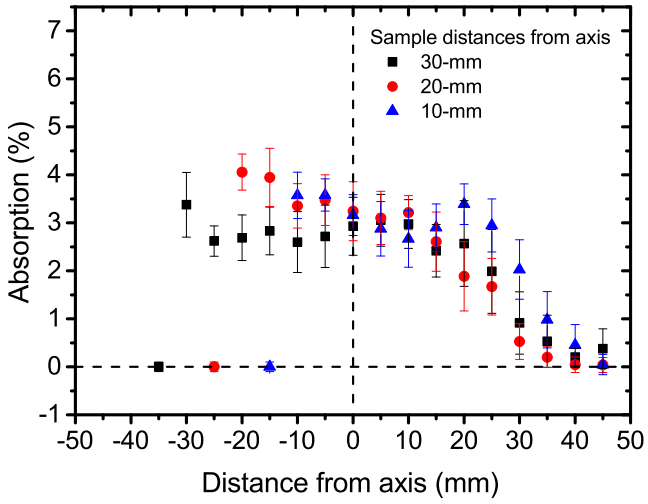

Fig. A.3 The vertical O_3 absorption profiles in the effluent region with at 20-mm from the nozzle with different distance from the propagation axis.

Appendix B

OH density in the effluent of the kHz APPJ

B.1 OH spectrum in the effluent of the kHz DBD APPJ

The setup used in chapter 6 for O_3 density measurement in the effluent of the kHz DBD APPJ with 2 slm He and less than 1% O_2 were adjusted to measure OH density. The conditions of the spectrometer and the CCD camera were the same as in chapter 7 for OH density measurement. The total 2 slm He were separated into one pure He channel and another He through water bubbler channel.

In the preliminary measurement, the background spectrum at the propagation axis with different distances from the nozzle is shown in figure B.1. At 1-mm from the nozzle, the spectrum intensity is about 700 counts and drops to around 670 counts at 10-mm from the nozzle. However, the spectrum at 10-mm shows the strong peak at 316.3 nm and is indicated as the nitrogen species spectrum. This obviously implies the contribution of N_2 from the ambient air. The further analysis on the absorption spectrum was found that under the maximum He+H_2O condition the absorption spectrum was in the noise level and cannot be used to calculate the OH density in the effluent of the kHz DBD atmospheric pressure plasma jet. Additionally, the OH density in the effluent region can be determined in the high H_2O concentration for example in [42].

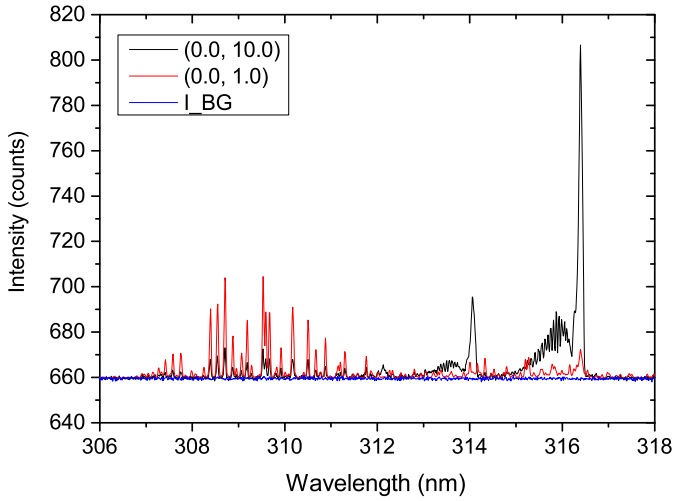

Fig. B.1 Plasma background spectrum with different distances from the nozzle on the propagation axis of the kHz DBD atmospheric pressure plasma jet, 1.9 slm He with 0.1 slm He + H_2O.

References

[1] R. J. Goldston and P. H. Rutherford. *Introduction to plasma physics*. Taylor & Francis, 1995.

[2] J. P. Freidberg. *Plasma Physics and Fusion Energy*. Cambridge University Press, 2007.

[3] J. Wesson. *Tokamaks*. Oxford Science Publications, 2011.

[4] S. Atzeni and J. Meyer-Ter-Vehn. *The Physics of Inertial Fusion*. Oxford University Press, 2009.

[5] M. A. Lieberman and A. J. Lichtenberg. *Principles of Plasma Discharges and Materials Processing*. John Wiley & Sons, Ltd., 2005.

[6] T. Makabe and Z. Lj. Petrovic. *Plasma electronics applications in microelectronic device fabrication*. CRC Press Taylor & Francis Group, 2 edition, 2015.

[7] R. M. Sankaran. *Plasma Processing of Nanomaterials*. CRC Press, 2011.

[8] F. R. Chang-Diaz. Plasma propulsion for interplanetary flight. *Thin Solid Films*, 506-507, 2006.

[9] M. Martinez-Sanchez and J. E. Pollard. Spacecraft electric propulsion-an overview. *Propulsion and Power*, 14(5):688–699, 1998.

[10] R. Hippler, H. Kersten, M. Schmidt, and K.H. Schoenbach. *Low temperature plasmas: fundamentals, technologies and techniques*, volume 1. Wiley-VCH, 2 edition, 2008.

[11] D. M. Manos and D. L. Flamm. *Plasma etching: an introduction*. Academic Press, 1989.

[12] C. Cardinaud, M. C. Peignon, and P. Y. Tessier. Plasma etching: principles, mechanisms, application to micro- and nano-technologies. *Applied Surface Science*, 164:72–83, 2000.

[13] D. B. Graves and D. Humbird. Surface chemistry associated with plasma etching processes. *Applied Surface Science*, 192:72–87, 2002.

[14] D. J. Economou. Modeling and simulation of plasma etching reactors for microelectronics. *Thin Solid Films*, 365:348–367, 2000.

[15] M. Konuma. *Film Deposition by Plasma Techniques*. Springer Berlin Heidelberg, reprint edition, 2011.

[16] A. Anders. *Handbook of Plasma Immersion Ion Implantation and Deposition*. Wiley, 2000.

[17] S. M. George. Atomic layer deposition: An overview. *Chem. Rev.*, 110(1):111–131, 2010.

[18] A. Schütze, J. Y. Jeong, S. E. Babayan, J. Park, G. S. Selwyn, and R. F. Hicks. The atmospheric-pressure plasma jet: A review and comparison to other plasma sources. *IEEE Transactions on Plasma Science*, 26(6), 1998.

[19] M. Laroussi, M.G. Kong, G. Morfill, and W. Stolz. *Plasma Medicine: Applications of Low-Temperature Gas Plasma in Medicine and Biology*. University Press, Cambrige, 2012.

[20] A. Fridman and G. Friedman. *Plasma Medicine*. John Wiley & Sons, Ltd., 2013.

[21] U. Kogelschatz. Atmospheric-pressure plasma technology. *Plasma Phys. Control. Fusion*, 46, 2004.

[22] D. P. Dowling. *Surface Processing Using Cold Atmospheric Pressure Plasmas*. Elsevier Ltd., 2014.

[23] A. Fridman. *Plasma Chemistry*. Cambridge University Press, 2008.

[24] K. Ostrikov, U. Cvelbar, and A. B. Murphy. Plasma nanoscience: setting directions, tackling grand challenges. *J. Phys. D: Appl. Phys.*, 44(174001), 2011.

[25] R. M. Sankaran. *Plasma Processing of nanomaterials*. CRC Press, 2011.

[26] D. Dobrynin, G. Fridman, G. Friedman, and A. Fridman. Physical and biological mechanisms of direct plasma interaction with living tissue. *New Journal of Physics*, 11(115020), 2009.

[27] B. Halliwell and J. M. C. Gutteridge. *Free radicals in biology and madicine*. Oxford University Press, 4 edition, 2007.

[28] C. O. Laux, T. G. Spence, C. H. Kruger, and R. N. Zare. Optical diagnostics of atmospheric pressure air plasmas. *Plasma Sources Sci. Technol.*, 12:125–138, 2003.

[29] R. H. Huddlestone and S. L. Leonard. *Plasma diagnostic techniques*. Academic Press, 1965.

[30] I. H. Hutchinson. *Principles of Plasma Diagnostics*. Cambridge University Press, 2002.

[31] H. R. Griem. *Principles of Plasma Spectroscopy*. Cambridge University Press, 2005.

[32] K. Niemi, V. Schulz-von der Gathen, and H. F. Döbele. Absolute atomic oxygen density measurements by two-photon absorption laser-induced fluorescence spectroscopy in an rf-excited atmospheric pressure plasma jet. *Plasma Sources Sci. Technol.*, 14:375–386, 2005.

[33] S. Reuter, J. Winter, A. Schmidt-Bleker, D. Schroeder, H. Lange, N. Knake, V. Schulz-von der Gathen, and K-D. Weltmann. Atomic oxygen in a cold argon plasma jet: TALIF spectroscopy in ambient air with modelling and measurements of ambient species diffusion. *Plasma Sources Sci. Technol.*, 21(024005), 21.

[34] K. Niemi, D. O'Connell, N. de Oliveira, D. Joyeux, L. Nahon, J. P. Booth, and T. Gans. Absolute atomic oxygen and nitrogen densities in radio-frequency driven atmospheric pressure cold plasmas: Synchrotron vacuum ultra-violet high-resolution fouriertransform absorption measurements. *Applied Physics Letters*, 103(034102), 2013.

[35] A. Greb, K. Niemi, D. O'Connell, and T. Gans. Energy resolved actinometry for simultaneous measurement of atomic oxygen densities and local mean electron energies in radio-frequency driven plasmas. *Applied Physics Letters*, 105(234105), 2014.

[36] J. S. Sousa, K. Niemi, L. J. Cox, Q. Th. Algwari, T. Gans, and D. O'Connell. Cold atmospheric pressure plasma jets as sources of singlet delta oxygen for biomedical applications. *J. Appl. Phys.*, 109(123302), 2011.

[37] J. Y. Jeong, J. Park, I. Henins, S. E. Babayan, V. J. Tu, G. S. Selwyn, G. Ding, and R. F. Hicks. Reaction chemistry in the afterglow of an oxygen-helium, atmospheric-pressure plasma. *J. Phys. Chem. A*, 104:8027–8032, 2000.

[38] R. Ono and T. Oda. Measurement of OH density and gas temperature in incipient spark ignited hydrogen air flame. *Combustion and Flame*, 152, 2008.

[39] Y. Nakagawa, R. Ono, and T. Oda. Density and temperature measurement of OH radicals in atmospheric-pressure pulsed corona discharge in humid air. *Journal of Applied Physics*, 110(073304), 2011.

[40] T. Verreycken, R. Mensink, R. van der Horst, N. Sadeghi, and P. J. Bruggeman. Absolute OH density measurements in the effluent of a cold atmospheric-pressure Ar-H_2O RF plasma jet in air. *Plasma Sources Sci. Technol.*, 22(055014), 2013.

[41] P. Bruggeman, G. Cunge, and N. Sadeghi. Absolute OH density measurements by broadband UV absorption in diffuse atmospheric pressure He-H_2O RF glow discharges. *Plasma Sources Sci. Technol.*, 21(035019), 2012.

[42] Q. Xiong, Z. Yang, and P. J. Bruggeman. Absolute OH density measurements in an atmospheric pressure dc glow discharge in air with water electrode by broadband UV absorption spectroscopy. *J. Phys. D: Appl. Phys.*, 48(424008), 2015.

[43] E. Wagenaars, T. Gans, D. O'Connell, and K. Niemi. Two-photon absorption laser-induced fluorescence measurements of atomic nitrogen in a radio-frequency atmospheric-pressure plasma jet. *Plasma Sources Sci. Technol.*, 21(042002), 2012.

[44] G. Dilecce, P. F. Ambrico, and S. De Benedictis. N_2 ($A\ ^3\Sigma_u^+$) density measurement in a dielectric barrier discharge in N_2 and N_2 with small O_2 admixtures. *Plasma Sources Sci. Technol.*, 16:511–522, 2007.

[45] A. F. H. van Gessel, K. M. J. Alards, and P. J. Bruggeman. NO production in an RF plasma jet at atmospheric pressure. *J. Phys. D: Appl. Phys.*, 46(265202), 2013.

[46] A. F. H. van Gessel, B. Hrycak, M. Jasiński, J. Mizeraczyk, J. J. A. M. van der Mullen, and P. J. Bruggeman. Temperature and NO density measurements by LIF and OES on an atmospheric pressure plasma jet. *J. Phys. D: Appl. Phys.*, 46(095201), 2013.

[47] H. C. Kim, F. Iza, S. S. Yang, M. Radmilović-Radjenović, and J. K. Lee. Particle and fluid simulations of low-temperature plasma discharges: benchmarks and kinetic effects. *J. Phys. D: Appl. Phys.*, 38:R283–R301, 2005.

[48] K. Niemi, S. Reuter, L. M. Graham, J. Waskoenig, N. Knake, V. Schulz von der Gathen, and T. Gans. Diagnostic based modelling of radio-frequency driven atmospheric pressure plasmas. *J. Phys. D: Appl. Phys.*, 43(124006), 2010.

[49] K. Niemi, T. Gans, and D. O'Connell. Comparison of a global model to semi-kinetic fluid simulations for atmospheric pressure radio-frequency plasmas. *Plasma Sources Sci. Technol.*, 22(032001), 2013.

[50] D. X. Liu, P. Bruggeman, F. Iza, M. Z. Rong, and M. G. Kong. Global model of low-temperature atmospheric-pressure He + H_2O plasmas. *Plasma Sources Sci. Technol.*, 19(025018), 2010.

[51] M. M. Turner. Uncertainty and error in complex plasma chemistry models. *Plasma Sources Sci. Technol.*, 24(035027), 2015.

[52] J. Orphal. A critical review of the absorption cross-sections of O_3 and NO_2 in the ultraviolet and visible. *Journal of Photochemistry and Photobiology A: Chemistry*, 157:185–209, 2003.

[53] R. Foest, M. Schmidt, and K. Becker. Microplasmas, an emerging field of low-temperature plasma science and technology. *International Journal of Mass Spectrometry*, 248:87–102, 2006.

[54] V. Schulz-von der Gathen, V. Buck, T. Gans, N. Knake, K. Niemi, St. Reuter, L. Schaper, and J. Winter. Optical diagnostics of micro discharge jets. *Contrib. Plasma Phys.*, 47:510–519, 2007.

[55] S. Zhang, W. van Gaens, B. van Gessel, S. Hofmann, E. van Veldhuizen, A. Bogaerts, and P. Bruggeman. Spatially resolved ozone densities and gas temperatures in a time modulate rf driven atmospheric pressure plasma jet: an analysis of the production and destruction mechanisms. *J. Phys. D: Appl. Phys.*, 46(205202), 2013.

[56] C. O'Neill, J. Waskoenig, and Gans. Tailoring electron energy distribution functions through energy confinement in dual radio-frequency driven atmospheric pressure plasmas. *Applied Physics Letters*, 101(154107), 2012.

[57] J. Waskoenig, K. Niemi, N. Knake, L. M. Graham, S. Reuter, V. Schulz-von der Gathen, and Gans T. Atomic oxygen formation in a radio-frequency driven micro-atmospheric pressure plasma jet. *Plasma Sources Sci. Technol.*, 19(045018), 2010.

[58] K. Niemi, J. Waskoenig, N. Sadeghi, T. Gans, and D. O'Connell. The role of helium metastable states in radio frequency driven helium oxygen atmospheric pressure plasma jets: measurement and numerical simulation. *Plasma Sources Sci. Technol.*, 20(055005), 2011.

[59] T. Murakami, K. Niemi, T. Gans, D. O'Connell, and W. G. Graham. Chemical kinetics and reactive species in atmospheric pressure helium oxygen plasmas with humid-air impurities. *Plasma Sources Sci. Technol.*, 22(015003), 2012.

[60] D. B. Graves. The emerging role of reactive oxygen and nitrogen species in redox biology and some implications for plasma applications to medicine and biology. *J. Phys. D: Appl. Phys.*, 45(263001), 2012.

[61] S. Paulussen, B. Verheyde, X. Tu, C. De Bie, T. Martens, D. Petrovic, A. Bogaerts, and B. Sels. Conversion of carbon dioxide to value-added chemicals in atmospheric pressure dielectric barrier discharges. *Plasma Sources Sci. Technol.*, 19(034015), 2010.

[62] Y. Bai, J. Chen, X. Li, and C. Zhang. Non-thermal plasmas chemistry as a tool for environmental pollutants abatement. *Rev. Environ. Contam. Toxicol.*, 201:117–136, 2009.

[63] L. F. Spencer and A. D. Gallimore. Efficiency of CO_2 dissociation in a radio-frequency discharge. *Plasma Chem. Plasma Process.*, 31:79–89, 2011.

[64] B. Ashford and X. Tu. Non-thermal plasma technology for the conversion of CO_2. *Current Opinion in Green and Sustainable Chemistry*, 3:45–49, 2017.

[65] C. Tendero, C. Tixier, P.Tristant, J. Desmaison, and P. Leprince. Atmospheric pressure plasmas: A review. *Spectrochimica Acta Part B*, 61:2–30, 2006.

[66] P. Chabert and N. Braithwaite. *Physics of Radio-Frequency Plasmas*. Cambridge University Press, 2011.

[67] G. J. M. Hagelaar and L. C. Pitchford. Solving the Boltzmann equation to obtain electron transport coefficients and rate coefficients for fluid models. *Plasma Sources Sci. Technol.*, 14:722–733, 2005.

[68] M. Capitelli, R. Celiberto, G. Colonna, F. Esposito, C. Gorse, K. Hassouni, A. Laricchiuta, and S. Longo. *Fundamental Aspects of Plasma Chemical Physics: Kinetics*. Springer, 2016.

[69] D. X. Liu, M. Z. Rong, X. H. Wang, F. Iza, M. G. Kong, and P. Bruggeman. Main species and physiochemical processes in cold atmospheric-pressure He + O_2 plasmas. *Plasma Process. Polym.*, 7:846–865, 2010.

[70] P. J. Bruggeman, N. Sadeghi, D. C. Schram, and V. Linss. Gas temperature determination from rotational lines in non-equilibrium plasmas: a review. *Plasma Sources Sci. Technol.*, 23(023001), 2014.

[71] A. J. Wagner, D. Mariotti, K. J. Yurchenko, and T. K. Das. Experimental study of a planar atmospheric-pressure plasma operating in the microplasma regime. *Physical Review E*, 80(065401), 2009.

[72] T. Murakami, K.Niemi, T. Gans, D. O'Connell, and W. G. Graham. Afterglow chemistry of atmospheric pressure helium oxygen plasmas with humid air impurity. *Plasma Sources Sci. Technol.*, 23(025005), 2014.

[73] J. J. Shi and M. G. Kong. Mechanisms of the alpha and gamma modes in radio-frequency atmospheric glow discharges. *Journal of Applied Physics*, 97(023306), 2005.

[74] Y. B. Golubovskii, V. A. Maiorov, J. Behnke, and J. F. Behnke. Modelling of the homogeneous barrier discharge in helium at atmospheric pressure. *Journal of Applied Physics*, 36, 2003.

[75] F. Iza, G. J. Kim, S. M. Lee, J. K. Lee, J. L. Walsh, Y. T. Zhang, and M. G. Kong. Microplasmas: Sources, particle kinetics, and biomedical applications. *Plasma Process. Polym.*, 5:322–344, 2008.

[76] J. Park, I. Henins, H. W. Herrmann, and G. S. Selwyn. Gas breakdown in an atmospheric pressure radio-frequency capacitive plasma source. *J. Appl. Phys.*, 89(15), 2001.

[77] J. L. Walsh and M. G. Kong. Contrasting characteristics of linear-field and cross-field atmospheric plasma jets. *Appl. Phys. Lett.*, 93(111501), 2008.

[78] P. S. Le, G. Li, S. Wang, H. P. Li, and C. Y. Bao. Characteristics of kilohertz-ignited, radio-frequency atmospheric-pressure dielectric barrier discharges in argon. *Appl. Phys. Lett.*, 95(201501), 2009.

[79] J. L. Walsh, F. Iza, N. B. Janson, V. J. Law, and M. G. Kong. Three distinct modes in a cold atmospheric pressure plasma jet. *J. Phys. D: Appl. Phys.*, 43(075201), 2010.

[80] J. Golda, J. Held, B. Redeker, M. Konkowski, P. Beijer, A. Sobota, G. Kroesen, N. St. J. Braithwaite, S. Reuter, M. M. Turner, T. Gans, D. O'Connell, and V. Schulz-von der Gathen. Concepts and characteristics of the 'COST Reference Microplasma Jet'. *J. Phys. D: Appl. Phys.*, 49(084003), 2016.

[81] S. Förster, C. Mohr, and W. Viöl. Investigations of an atmospheric pressure plasma jet by optical emission spectroscopy. *Surface & Coatings Technology*, 200, 2005.

[82] M. Laroussi and X. Lu. Room-temperature atmospheric pressure plasma plume for biomedical applications. *Appl. Phys. Lett.*, 87(113902), 2005.

[83] A. D. Morris, G. B. McCombs, T. Akan, W. Hynes, M. Laroussi, and S. L. Tolle. Cold plasma technology: Bactericidal effects on geobacillus stearothermophilus and bacillus cereus microorganisms. *J Dental Hygiene*, 83(55), 2009.

[84] G. Chen, S. Chen, M. Zhou, W. Feng, W. Gu, and S. Yang. The preliminary discharging characterization of a novel APGD plume and its application in organic contaminant degradation. *Plasma Sources Sci. Technol.*, 15, 2006.

[85] D. B. Kim, J. K. Rhee, S. Y. Moon, and W. Choe. Study of geometrical and operational parameters controlling the low frequency microjet atmospheric pressure plasma characteristics. *Appl. Phys. Lett.*, 89(061502), 2006.

[86] N. Knake, K. Niemi, S. Reuter, V. Schulz-von der Gathen, and J. Winter. Absolute atomic oxygen density profiles in the discharge core of a microscale atmospheric pressure plasma jet. *Applied Physics Letters*, 93(131503), 2008.

[87] E. Stoffels, A. J. Flikweert, W. W. Stoffels, and G. M. W. Kroesen. Plasma needle: a non-destructive atmospheric plasma source for fine surface treatment of (bio)materials. *Plasma Sources Sci. Technol.*, 11, 2002.

[88] E. Stoffels, Y. A. Gonzalvo, T. D. Whitmore, D. L. Seymour, and J. A. Rees. A plasma needle generates nitric oxide. *Plasma Sources Sci. Technol.*, 15, 2006.

[89] V. Léveillé and S. Coulombe. Design and preliminary characterization of a miniature pulsed RF APGD torch with downstream injection of the source of reactive species. *Plasma Sources Sci. Technol.*, 14:467–476, 2005.

[90] U. Kogelschatz. Dielectric-barrier discharges: Their history, discharge physics, and industrial applications. *Plasma Chemistry and Plasma Processing*, 23(1), 2003.

[91] B. Eliasson and U. Kogelschatz. Modeling and applications of silent discharge plasmas. *IEEE TRANSACTIONS ON PLASMA SCIENCE*, 19(2), 1991.

[92] T. Yokoyama, M. Kogoma, T. Moriwaki, and S. Okazak. The mechanism of the stabilisation of glow plasma at atmospheric pressure. *J. Phys. D: Appl. Phys.*, 23:1125–1128, 1990.

[93] J. Winter, M. Dünnbier, A. Schmidt-Bleker, A. Meshchanov, S. Reuter, and K-D. Weltmann. Aspects of uv-absorption spectroscopy on ozone in effluents of plasma jets operated in air. *J. Phys. D: Appl. Phys.*, 45(385201), 2012.

[94] S. Reuter, J. Winter, S. Iseni, S. Peters, A. Schmidt-Bleker, M. Dunnbier, J. Schafer, R. Foest, and K-D Weltmann. Detection of ozone in a mhz argon plasma bullet jet. *Plasma Sources Sci. Technol.*, 21(034015), 2012.

[95] B. Haertel, T. von Woedtke, K-D. Weltmann, and U. Lindequist. Non-thermal atmospheric-pressure plasma possible application in wound healing. *Biomol Ther (Seoul)*, 22(6):477–490, 2014.

[96] K. P. Arjunan and A. M. Clyne. Hydroxyl radical and hydrogen peroxide are primarily responsible for dielectric barrier discharge plasma-induced angiogenesis. *Plasma Process. Polym.*, 8:1154–1164, 2011.

[97] H. J. Kunze. *Introduction to Plasma Spectroscopy*. Springer, 2009.

[98] Daily. Laser induced fluorescence spectroscopy in flames. *Prog. Energy Combust. Sci*, 1997.

[99] T. Lang, M. Motzkus, H. M. Frey, and P. Beaud. High resolution femtosecond coherent anti-stokes raman scattering: Determination of rotational constants, molecular anharmonicity, collisional line shifts, and temperature. *The Journal of Chemical Physics*, 115(5418), 2001.

[100] C. Yubero, M. S. Dimitrijevi, M. C. Garcia, and M. D. Calzada. Using the van der Waals broadening of the spectral atomic lines to measure the gas temperature of an argon microwave plasma at atmospheric pressure. *Spectrochimica Acta Part B*, 62:169–176, 2007.

[101] Crystal IS. UVC LEDs provide more benefits than tranditional UV lamps in instrumentation. Technical report, Crystal IS, Inc., 2014.

[102] T. Gans, D. O'Connell, V. Schulz-von der Gathen, and J. Waskoenig. The challenge of revealing and tailoring the dynamics of radio-frequency plasmas. *Plasma Sources Sci. Technol.*, 19(034010), 2010.

[103] D. Maletić, N. Puač, S. Lazović, G. Malović, T. Gans, V. Schulz-von der Gathen, and Z. Lj. Petrović. Detection of atomic oxygen and nitrogen created in a radio-frequency-driven micro-scale atmospheric pressure plasma jet using mass spectrometry. *Plasma Phys. Control. Fusion*, 54(124046), 2012.

[104] G. Dilecce. Optical spectroscopy diagnostics of discharges at atmospheric pressure. *Plasma Sources Sci. Technol.*, 23(015011), 2014.

[105] D. Ellerweg, A. von Keudell, and J. Benedikt. Unexpected O and O_3 production in the effluent of He/O_2 microplasma jets emanating into ambient air. *Plasma Sources Sci. Technol.*, 21(034019), 2012.

[106] D. Ellerweg, J. Benedikt, A. von Keudell, N. Knake, and V. Schulz-von der Gathen. Characterization of the effluent of a He/O_2 microscale atmospheric pressure plasma jet by quantitative molecular beam mass spectrometry. *New Journal of Physics*, 12, 2010.

[107] L. T. Molina and M. J. Molina. Absolute absorption cross sections of ozone in the 185 to 350 nm wavelength range. *Journal of Geophysical Research*, 91:14501–14508, 1986.

[108] J. Malicet, J. Brion, and D. Daumont. Temperature dependence of the absorption cross-section of ozone at 254 nm. *Chemical Physics Letters*, 158:293–296, 1989.

[109] M. G. Kong, G. Kroesen, G. Morfill, T. Nosenko, T. Shimizu, J. van Dijk, and J. L. Zimmermann. Plasma medicine: an introductory review. *New Journal of Physics*, 11(115012), 2009.

[110] G. Y. Park, S. J. Park, M. Y. Choi, I. G. Koo, J. H. Byun, J. W. Hong, G. J. Sim, J. Y. amd Collins, and J. K. Lee. Atmospheric-pressure plasma sources for biomedical applications. *Plasma Sources Sci. Technol.*, 21(043001), 2012.

[111] S. U. Kalghatgi, G. Fridman, M. Cooper, M. Nagaraj, M. Peddinghaus, M. Balasubramanian, V. N. Vasilets, A. F. Gutsol, A. Fridman, and G. Friedman. Mechanism of blood coagulation by nonthermal atmospheric pressure dielectric barrier discharge plasma. *IEEE TRANSACTIONS ON PLASMA SCIENCE*, 35(5), 2007.

[112] G. Isbary, G. Morfill, H. U. Schmidt, M. Georgi, K. Ramrath, J. Heinlin, S. Karrer, M. Landthaler, T. Shimizu, B. Steffes, W. Bunk, R. Monetti, J. L. Zimmermann, R. Pompl, and W. Stolz. A first prospective randomized controlled trial to decrease bacterial load using cold atmospheric argon plasma on chronic wounds in patients. *British Journal of Dermatology*, 2010.

[113] M. Laroussi and F. Leipold. Evaluation of the roles of reactive species, heat, and uv radiation in the inactivation of bacterial cells by air plasmas at atmospheric pressure. *International Journal of Mass Spectrometry*, 233, 2004.

[114] M. Laroussi. Low temperature plasma-based sterilization: Overview and state-of-the-art. *Plasma Processes and Polymers*, 2:391–400, 2005.

[115] D. O'Connell, L. J. Cox, W. B. Hyland, S. J. McMahon, S. Reuter, W. G. Graham, T. Gans, and F. J. Currell. Cold atmospheric pressure plasma jet interactions with plasmid DNA. *Applied Physics Letters*, 98(043701), 2011.

[116] G. Fridman, A. Shereshevsky, M. M. Jost, A. D. Brooks, A. Fridman, A. Gutsol, V. Vasilets, and G. Friedman. Floating electrode dielectric barrier discharge plasma in air promoting apoptotic behavior in melanoma skin cancer cell lines. *Plasma Chem Plasma Process*, 23, 2007.

[117] S. Iseki, K. Nakamura, M. Hayashi, H. Tanaka, H. Kondo, H. Kajiyama, H. Kano, F. Kikkawa, and M. Hori. Selective killing of ovarian cancer cells through induction of apoptosis by nonequilibrium atmospheric pressure plasma. *Applied Physics Letters*, 100(113702), 2012.

[118] H. Wiseman and B. Halliwell. Damage to DNA by reactive oxygen and nitrogen species: role in inflammatory disease and progression to cancer. *Biochem. J.*, 313:17–29, 1996.

[119] A. M. Hirst, M. S. Simms, V. M. Mann, N. J. Maitland, D. O'Connell, and F. M. Frame. Low-temperature plasma treatment induces DNA damage leading to necrotic cell death in primary prostate epithelial cells. *British Journal of Cancer*, 112:1536–1545, 2015.

[120] A. R. Gibson, H. O. McCarthy, A. A. Ali, D. O'Connell, and W. G. Graham. Interactions of a non-thermal atmospheric pressure plasma effluent with PC-3 prostate cancer cells. *Plasma Process. Polym.*, 11:1142–1149, 2014.

[121] P. Bruggeman and R. Brandenburg. Atmospheric pressure discharge filaments and microplasmas: physics, chemistry and diagnostics. *J. Phys. D: Appl. Phys.*, 46(464001), 2013.

[122] G. Fridman, G. Friedman, A. Gutsol, A. B. Shekhter, V. N. Vasilets, and A. Fridman. Applied plasma medicine. *Plasma Process. Polym.*, 5:503–533, 2008.

[123] A. M. Hirst, F. M. Frame, M. Arya, N. J. Maitland, and D. O'Connell. Low temperature plasmas as emerging cancer therapeutics: the state of play and thoughts for the future. *Tumour biology : the journal of the International Society for Oncodevelopmental Biology and Medicine*, 2016.

[124] D. S. Stafford and M. J. Kushner. Singlet delta oxygen production in He/O_2 mixtures in flowing low pressure plasmas. *J. Appl. Phys.*, 96(5), 2004.

[125] U. Fantz. Basics of plasma spectroscopy. *Plasma Sources Sci. Technol.*, 15, 2006.

[126] M. M. Turner. Uncertainty and sensitivity analysis in complex plasma chemistry. *Plasma Sources Sci. Technol.*, 25(015003), 2016.

[127] V. Schulz-von der Gathen, L. Schaper, N. Knake, S. Reuter, K. Niemi, T. Gans, and J. Winter. Spatially resolved diagnostics on a microscale atmospheric pressure plasma jet. *J. Phys. D: Appl. Phys.*, 41(194004), 2008.

[128] Andy West. *Optical and electrical diagnosis of atmospheric pressure plasma jets*. PhD thesis, Department of Physics, University of York, April 2016.

[129] B. Twomey, A. Nindrayog, K. Niemi, W. G. Graham, and D. P. Dowling. Correlation between the electrical and optical properties of an atmospheric pressure plasma during siloxane coating deposition. *Plasma Chem Plasma Process*, 31:139–156, 2011.

[130] M. Ingram and Haines R. B. Inhibition of bacterial growth by pure ozone in the presence of nutrients. *Journal of Hygiene*, 47:146–158, 1949.

[131] S. Kelly, J. Golda, M. M. Turner, and V. Schulz-von der Gathen. Gas and heat dynamics of a micro-scaled atmospheric pressure plasma reference jet. *J. Phys. D: Appl. Phys.*, 48(444002), 2015.

[132] N. Balcon, A. Aanesland, and R. Boswell. Pulsed RF discharges, glow and filamentary mode at atmospheric pressure in argon. *Plasma Sources Sci. Technol.*, 16, 2007.

[133] R. Ye, T. Ishigaki, and T. Sakuta. Controlled generation of pulse-modulated rf plasmas for materials processing. *Plasma Sources Sci. Technol.*, 14, 2005.

[134] J. J. Shi, J. Zhang, G. Qiu, J. L. Walsh, and M. G. Kong. Modes in a pulse-modulated radio-frequency dielectric-barrier glow discharge. *Applied Physics Letters*, 93(041502), 2008.

[135] H. Ohkawa, T. Akitsu, M. Tsuji, H. Kimura, M. Kogoma, and K. Fukushima. Pulse-modulated, high-frequency plasma sterilization at atmospheric-pressure. *Surface & Coatings Technology*, 200:5829–5835, 2006.

[136] Andor Technology Ltd. Andor solis, 2012.

[137] 2B Technologies. Model 205 ozone monitor.

[138] R. Dorai and M. J. Kushner. A model for plasma modification of polypropylene using atmospheric pressure discharges. *J. Phys. D: Appl. Phys.*, 36:666–685, 2003.

[139] K. R. Stalder, R. J. Vidmar, G. Nersisyan, and W. G. Graham. Modeling the chemical kinetics of high-pressure glow discharges in mixtures of helium with real air. *Journal of Applied Physics*, 99(093301), 2006.

[140] Y. S. Seo, A-A. H. Mohamed, H. C. Woo, H. W. Lee, J. K. Lee, and K. T. Kim. Comparative studies of atmospheric pressure plasma characteristics between He and Ar working gases for sterilization. *IEEE Transactions on Plasma Science*, 38.10:2954–2962, 2010.

[141] X. P. Lu, T. Ye, Y. G. Cao, Z. Y. Sun, Q. Xiong, Z. Y. Tang, Z. L. Xiong, J. Hu, Z. H. Jiang, and Y. Pan. The roles of the various plasma agents in the inactivation of bacteria. *J. Appl. Phys.*, 104, 2008.

[142] S. Schneider, J.-W. Lackmann, D. Ellerweg, D. Benjamin, F. Narberhaus, J. E. Bandow, and J. Benedikt. The role of VUV radiation in the inactivation of bacteria with an atmospheric pressure plasma jet. *Plasma Process. Polym.*, 9:561–568, 2012.

[143] M. A. Khadre, A. E. Yousef, and J.-G. Kim. Microbiological aspects of ozone applications in food: A review. *Concise Reviews in Food Science*, 66, 2006.

[144] L. F. Gaunt, C. B. Beggs, and G. E. Georghiou. Bactericidal action of the reactive species produced by gas-discharge nonthermal plasma at atmospheric pressure: A review. *IEEE TRANSACTIONS ON PLASMA SCIENCE*, 34(4), 2006.

[145] R. Alvarez, A. Rodero, and M. C. Quintero. An Abel inversion method for radially resolved measurements in the axial injection torch. *Spectrochimica Acta Part B*, 57:1665–1680, 2002.

[146] G. Pretzier. A new method for numerical Abel-inversion. *Z. Naturforsch*, 46a:639–641, 1991.

[147] C. Killer. Abel inversion algorithm. Online, September 2013.

[148] Mathematica. Version 10.4, Wolfram Research, Inc. 2016.

[149] MATLAB. version 8.3.0 (r2014a), 2014.

[150] M. J. Buie, J. T. P. Pender, J. P. Holloway, T. Vincent, P. L. G. Ventzek, and M. L. Brake. Abel's inversion applied to experimental spectroscopic data with off axis peaks. *J. Quant. Spectrosc. Radiat. Transfer*, 55(2):231–243, 1996.

[151] J. S. Sousa, Q. Algwari, K. Niemi, T. Gans, and D. O'Connell, editors. *Reactive oxygen species in kHz-driven atmospheric pressure plasma jets*. ICPIG, August 2011.

[152] P. Bruggeman and C. Leys. Non-thermal plasmas in and in contact with liquids. *J. Phys. D: Appl. Phys.*, 42(053001), 2009.

[153] B. R. Locke and Shih K. Y. Review of the methods to form hydrogen peroxide in electrical discharge plasma with liquid water. *Plasma Sources Sci. Technol.*, 20(034006), 2011.

[154] K. R. Stalder, D. F. McMillen, and J. Woloszko. Electrosurgical plasmas. *J. Phys. D: Appl. Phys.*, 38, 2005.

[155] X. T. Deng, J. J. Shi, G. Shama, and M. G. Kong. Effects of microbial loading and sporulation temperature on atmospheric plasma inactivation of bacillus subtilis spores. *Applied Physics Letters*, 87(153901), 2005.

[156] H. W. Herrmann, I. Henins, J. Park, and G. S. Selwyn. Decontamination of chemical and biological warfare (CBW) agents using an atmospheric pressure plasma jet (APPJ). *Physics of Plasmas*, 6(2284), 1999.

[157] P. Muranyi, J. Wunderlich, and M. Heise. Influence of relative gas humidity on the inactivation efficiency of a low temperature gas plasma. *Journal of Applied Microbiology*, 104, 2008.

[158] A. N. Bhoj and M. J. Kushner. Repetitively pulsed atmospheric pressure discharge treatment of rough polymer surfaces: Ii. treatment of micro-beads in He/NH_3/H_2O and He/O_2/H_2O mixtures. *Plasma Sources Sci. Technol.*, 17(035025), 2008.

[159] G. Dilecce, P. F. Ambrico, M. Simek, and S. De Benedictis. LIF diagnostics of hydroxyl radical in atmospheric pressure He-H_2O dielectric barrier discharges. *Chemical Physics*, 398:142–147, 2012.

[160] C. Wang and N. Srivastava. OH number densities and plasma jet behavior in atmospheric microwave plasma jets operating with different plasma gases (Ar, Ar/N_2, and Ar/O_2). *Eur. Phys. J. D*, 60:465–477, 2010.

[161] C. Wang, N. Srivastava, S. Scherrer, P. R. Jang, T. S. Dibble, and Y. Duan. Optical diagnostics of a low power-low gas flow rates atmospheric-pressure argon plasma created by a microwave plasma torch. *Plasma Sources Sci. Technol.*, 18(025030), 2009.

[162] H.-P. Dorn, R. Neuroth, and A. Hofzumahaus. Investigation of OH absorption cross sections of rotational transitions in the $A^2\Sigma^+$, $v' = 0 \leftarrow X^2\Pi$, $v'' = 0$ band under atmospheric conditions: Implications for tropospheric long-path absorption measurement. *Journal of Geophysical Research*, 100(D4):7397–7409, 1995.

[163] G. Dilecce, P. F. Ambrico, M. Simek, and S. De Benedictis. OH density measurement by time-resolved broad band absorption spectroscopy in an Ar-H_2O dielectric barrier discharge. *J. Phys. D: Appl. Phys.*, 45(125203), 2012.

[164] K. Niemi. OH(A-X) fitting spectra program (private communication). 2015.

[165] G. H. Dieke and H. M. Crosswhite. The ultraviolet bands of OH fundamental data. *J. Quant. Spectrosc. Radiat. Transfer.*, 2:97–199, 1962.

[166] L. T. Earls. Intensities in $^2\Pi$ - $^2\Sigma$ transition in diatomic molecules. *Physical Review*, 48, 1935.

[167] K. R. German. Direct measurement of the radiative lifetimes of the a $^2\Sigma^+$+ ($v' = 0$) states of OH and OD. *The Journal of Chemical Physics*, 62(2584), 1975.

[168] A. Goldman and J. R. Gillis. Spectral line parameters for the $A^2\Sigma$- $X^2\Pi(0,0)$ band of OH for atmospheric and high temperatures. *J. Quant. Spectrosc. Radiat. Transfer.*, 25:111–135, 1981.

[169] O. A. Alduchov and R. E. Eskridge. Improved mafnus form approximation of saturation vapor pressure. *Journal of Applied Meteorology*, 35:601–609, 1996.

[170] A. Y. Nikiforov, A. Sarani, and C. Leys. The influence of water vapor content on electrical and spectral properties of an atmospheric pressure plasma jet. *Plasma Sources Sci. Technol.*, 20(015014), 2011.

[171] O. A. Alduchov and R. E. Eskridge. Improved Magnus form approximation of saturation vopor. *Journal of applied meteorology*, 35:601–609, 1996.

[172] Q. Wang, D. J. Economou, and V. M. Donnelly. Simulation of a direct current microplasma discharge in helium at atmospheric pressure. *J. Appl. Phys.*, 100(023301), 2006.

[173] P. Bruggeman and D. C. Schram. On OH production in water containing atmospheric pressure plasmas. *Plasma Sources Sci. Technol.*, 19(045025), 2010.

[174] M. McKay, D. X. Liu, M. Z. Rong, F. Iza, and M. G. Kong. Generation and loss of reactive oxygen species in low-temperature atmospheric-pressure RF He + O_2 + H_2O plasmas. *J. Phys. D: Appl. Phys.*, 45(172001), 2012.

[175] A. Foote, M. North, and T. Gans. Conversion of CO_2 using radio-frequency atmosphere pressure plasma: determining the best carrier gas and the dominant pathways. Department of Physics, University of York, June 2016.

[176] C. De Bie, T. Martens, J. van Dijk, S. Paulussen, B. Verheyde, S. Corthals, and A. Bogaerts. Dielectric barrier discharges used for the conversion of greenhouse gases: modeling the plasma chemistry by fluid simulations. *Plasma Sources Sci. Technol.*, 20(024008), 2011.

[177] T. Silva, N. Britun, T. Godfroid, and R. Snyders. Optical characterization of a microwave pulsed discharge used for dissociation of CO_2. *Plasma Sources Sci. Technol.*, 23(025009), 2014.

[178] L. F. Spencer and A. D. Gallimore. CO_2 dissociation in an atmospheric pressure plasma/catalyst system: a study of efficiency. *Plasma Sources Sci. Technol.*, 22(015019), 2013.

[179] T. Nunnally, K. Gutsol, A. Rabinovich, A. Fridman, A. Gutsol, and A. Kemoun. Dissociation of CO_2 in a low current gliding arc plasmatron. *J. Phys. D: Appl. Phys.*, 44(274009), 2011.

[180] A. Bogaerts, T. Kozák, K. van Laer, and R. Snoeckx. Plasma-based conversion of CO_2: current status and future challenges. *The Royal Society of Chemistry*, 183, 2015.

[181] M. Ramakers, I. Michielsen, R. Aerts, V. Meynen, and A. Bogaerts. Effect of argon or helium on the CO_2 conversion in a dielectric barrier discharge. *Plasma Process. Polym.*, 12, 2015.

[182] M. Tsuji, T. Tanoue, K. Nakano, and Y. Nishimura. Decomposition of CO_2 into CO and O in a microwave-excited discharge flow of CO_2/He or CO_2/Ar mixtures. *Chem. Lett.*, 1:22–23, 2001.

[183] H. S. Johansen. Determination of oxygen-18 abundances by analysis of the first negative emission spectrum of CO^+. *Int. J. Radiat. Appl. Instrum.*, 39(10):1059–1063, 1988.

[184] T. S. Wauchop and H. P. Broida. Absolute measuremnts of light emission from $CO_2{}^+$ and CO in the interaction of He(2^3S) with $CO_2{}^*$. *J. Quant. Spectrosc. Radiat. Transfer.*, 12:371–378, 1972.